DISSERTATION

THE RESPONSE OF A SPHERICAL TISSUE-EQUIVALENT PROPORTIONAL COUNTER TO DIFFERENT HEAVY IONS WITH SIMILAR VELOCITIES

Submitted by

Phillip James Taddei

Department of Environmental and Radiological Health Sciences

In partial fulfillment of the requirements for the Degree of Doctor of Philosophy
Colorado State University
Fort Collins, Colorado
Spring 2005

ProQuest Information and Learning Company
300 North Zeeb Road
P.O. Box 1346
Ann Arbor, MI 48106-1346

Colorado State University

August 27, 2004

WE HEREBY RECOMMEND THAT THE DISSERTATION PREPARED UNDER OUR SUPERVISION BY PHILLIP JAMES TADDEI ENTITLED *THE RESPONSE OF A SPHERICAL TISSUE-EQUIVALENT PROPORTIONAL COUNTER TO DIFFERENT HEAVY IONS WITH SIMILAR VELOCITIES* BE ACCEPTED AS FULFILLING IN PART REQUIREMENTS FOR THE DEGREE OF DOCTOR OF PHILOSOPHY.

Committee on Graduate Work

(Please print name under signature)

James Durham
James Durham
Lawrence Heilbronn
Lawrence Heilbronn

Thomas Lee

Thomas B Borak
Adviser THOMAS B BORAK
John D. Zimbrick
Department Head/Director JOHN D. ZIMBRICK

ABSTRACT OF DISSERTATION

THE RESPONSE OF A SPHERICAL TISSUE-EQUIVALENT PROPORTIONAL COUNTER TO DIFFERENT HEAVY IONS WITH SIMILAR VELOCITIES

A tissue-equivalent proportional counter (TEPC) has been used as an area monitor to measure absorbed dose and estimate equivalent dose during Space Transport Shuttle and International Space Station missions. This detector measures energy deposition events in simulated small volumes of tissue on the order of the size of a mammalian cell nucleus. A TEPC measures energy deposited in tissue of simulated microscopic volumes on an event-by-event basis and has a large dynamic domain of sensitivity to energy deposition events, ranging from hundreds of eV to thousands of keV. An enhanced understanding of the response of the TEPC is necessary to correctly evaluate these microdosimetric quantities. The particles of particular interest to which astronauts are exposed in space are high atomic number (atomic number, $Z \geq 2$) and high energy (HZE) ions originating from galactic cosmic radiation and solar radiation.

The response of a spherical tissue-equivalent proportional counter to different HZE ions having similar energy per nucleon (i.e., similar velocity) was studied using the Heavy Ion Medical Accelerator operated by the National Institute of Radiological Sciences in Chiba, Japan. Detector response was measured for ^{12}C, ^{16}O, ^{28}Si and ^{56}Fe at 376 MeV nucleon^{-1} (velocity relative to the speed of light, $\beta = 0.70$) and ^{4}He and ^{12}C at 220 MeV nucleon^{-1} ($\beta = 0.59$). A particle spectrometer was used to record the charge and position of each incident beam particle. This enabled reconstruction of the location of the

track as it passed though the TEPC and ensured that the incident particle survived without undergoing fragmentation.

Events with small energy deposition were observed for particles that passed through the wall of the TEPC but not through the sensitive volume. Events with large energy deposition were observed for particles that interacted with the anode or helical wire or grazed the inside wall of the gas cavity. Data indicated that the frequency averaged lineal energy, $\bar{y}_f$, was always less than the linear energy transfer (*LET*) of the incident particles. The dose averaged lineal energy, $\bar{y}_D$, was approximately equal to *LET* for particles with *Z* greater than 6 and *LET* greater than 10 keV μm^{-1}, whereas $\bar{y}_D$ was larger than *LET* for the lighter particles with lower *LET*. Part of this effect is due to the low energy deposition events that are often indistinguishable from noise. The small energy deposition portion of the lineal energy distribution had a similar shape for ions of similar velocity, indicating that ions of the same velocity have identical delta-ray wall effects.

When using a TEPC, a lower threshold for energy deposition must be selected below which events are considered indistinguishable from noise and are eliminated from the data. Careful consideration must be made when selecting a lower threshold in the spectrum of energy deposition response of the TEPC. The choice of the lower threshold has a measurable effect on $\bar{y}_f$ and $\bar{y}_D$.

Although the TEPC is not an *LET* spectrometer, it can provide real time measurement of dose and estimation of quality for HZE particles. The energy deposition response of the TEPC can be used along with the mass of the active volume of the TEPC

to measure absorbed dose. The distribution of lineal energy events may be used to estimate the average quality of the radiation and, hence, equivalent dose.

Phillip James Taddei
Environmental and Radiological
Health Sciences Department
Colorado State University
Fort Collins, CO 80523
Spring 2005

ACKNOWLEDGMENTS

It is accepted, and perhaps preferred, for scientists in this generation to by and large disregard the Author of nature. There is a temptation as a scientist to say, "Look what I have done." This was the disposition of King Herod of Judah shortly before he was struck down and eaten by worms. King Nebuchadnezzar of ancient Babylon displayed the same arrogant manner, and he spent the next seven years away from people, eating grass and living like an animal. I must clearly acknowledge my God the Creator ("For I desire...acknowledgment of God," Hosea 6:6, NIV) in His marvelous work—visible and invisible.

The heavens declare the glory of God,
    and the sky above proclaims His handiwork (Psalm 19:1, ESV).

Let the heavens be glad, and let the earth rejoice;
    let the sea roar, and all that fills it;
    let the field exult, and everything in it!
Then shall all the trees of the forest sing for joy
    before the LORD (Psalm 96:11, ESV).

Let the sea roar, and all that fills it;
    the world and those who dwell in it!
Let the rivers clap their hands;
    let the hills sing for joy together
before the LORD (Psalm 98:7,8, ESV).

Praise the LORD, all his works
    everywhere in his dominion (Psalm 103:22, NIV).

O LORD my God, you are very great!
You are clothed with splendor and majesty,
    covering yourself with light as with a garment,
    stretching out the heavens like a tent.
. . .
O LORD how manifold are your works!
    In wisdom have you made them all;
    the earth is full of your creatures.
. . .
May the glory of the LORD endure forever;
    may the LORD rejoice in His works (Psalm 104:1,2,24,31, ESV).

Praise [the LORD], sun and moon,
    praise Him, all you shining stars!
Praise Him, you highest heavens
    and you waters above the heavens!
Let them praise the Name of the LORD!
    For He commanded and they were created (Psalm 148:3-5, ESV).

Lift up your eyes on high and see: Who created these?
    He who brings out their host by number, calling them by name,
by the greatness of His might,
    and because He is strong in power
    not one is missing (Isaiah 40:26).

The purpose of the creation, including the heavens and solar, trapped, and galactic cosmic radiation, is to display God's majesty and put mankind in awe of Him, "For since the creation of the world God's invisible qualities—his eternal power and divine nature—have been clearly seen, being understood from what has been made" (Romans 1:20, NIV). We cannot see these tiny particles, but we can see the effects of them—from the Aurora Borealis to the response of a tissue-equivalent proportional counter. What is their source? Their source is the ordination of Almighty God, "In the beginning God created the heavens and the earth" (Genesis 1:1, NIV). "For by Him all things were created, in heaven and on earth, visible and invisible...all things were created through Him and for Him. And He is before all things, and in Him all things hold together" (Colossians

1:16,17, ESV). He "upholds the universe by the word of His power" (Hebrews 1:3, ESV).

How can we disregard the One who designed and sustains the laws of physics discovered by Sir Isaac Newton, who said

> This most beautiful system of the sun, planets, and comets, could only proceed from the counsel and dominion of an intelligent Being. ...This Being governs all things, not as the soul of the world, but as Lord over all....He is eternal and infinite, omnipotent and omniscient; that is, His duration reaches from eternity to eternity; His presence from infinity to infinity; He governs all things, and knows all things that are or can be done (Newton, 1687)

and James Clerk Maxwell, who said

> Through the creatures Thou hast made
> Show the brightness of Thy glory,
> Be eternal Truth displayed
> In their substance transitory,
> Till green Earth and Ocean hoary,
> Massy rock and tender blade
> Tell the same unending story—
> "We are Truth in Form arrayed" (Maxwell, 1853)

and Albert Einstein, who said

> I want to know how God created this world (Clarck, 1971).

John Piper exhibited his exultation in God for His creation, "What is this universe but the lavish demonstration of the incredible, incomparable, unimaginable exuberance and wisdom and power and greatness of God! What a God He must be!" (Piper, 2000) When meditating on the nature of the universe, I gladly and joyfully bow in submission to and in awe of my God.

> When I consider Your heavens, the work of Your fingers,
> the moon and the stars, which You have set in place,
> what is man that You are mindful of him,
> the son of man that You care for him? (Psalm 8:3,4, NIV)

I am thankful to God, and I acknowledge Him as my sovereign master. He has provided for me and my family everything that we need. He has restored my health. He has loved me with a forgiving, everlasting, and steadfast love. He has granted me four years of investigating his natural world. He has established His gospel in my heart. Everything that I am that is good comes from God. He works in me "both to will and to work for His good pleasure" (Philippians 2:13, ESV).

Thomas Borak has been my advisor and scientific mentor, and he has become my friend. His scientific wisdom demands my attention and observance. His knowledge in the radiological health sciences is beyond comparison. For good reason he is well respected by his peers and collaborators. He is a great teacher and experimentalist. I thank God for Dr. Borak's place in my life, and it has been my honor to follow in his footsteps for the past four years.

Thanks to Brad Gersey and Stephen Guetersloh for training and advising me while they were at CSU. They have also been quick and eager in helping me with this research.

Cary Zeitlin, Lawrence Heilbronn, and Jack Miller of the Lawrence Berkeley National Laboratory were essential collaborators on all of the HZE ion experiments. They provided equipment and expertise. They took turns running the data acquisition system orchestrated by Dr. Zeitlin. They worked tirelessly to ensure that we always collected high-quality data. Without the cooperation of the LBL group, this research would have been virtually impossible.

Yoshiyuki Iwata and Takeshi Murakami of the National Institute of Radiological Sciences also collaborated on these experiments and communicated with the staff of the HIMAC facilities.

Erin Kasdin must be acknowledged for her generous help in the calibration of the TEPC.

Thank you to my graduate committee, Thomas Borak, James Durham, Lawrence Heilbronn, and Thomas Lee, for being willing and available to help in any way to make sure I completed my research.

E. Dan Dahlberg of the University of Minnesota was the first to introduce me to the physics laboratory. The hours we spent in his office discussing physics and metaphysics were priceless and, I hope, mutually enjoyable. He accepted me and respected my ideas and input even when I was a meager undergraduate student.

I am grateful for the support given by the other faculty and staff of the Department of Radiological Health Sciences at Colorado State University, especially Julie Asmus, Chuck Sampier, Norma Bulera, Sandra Wiggen, Shawki Ibrahim, and F. Ward Whicker.

This research was financed by the NASA Specialized Centers for Outreach, Research, and Training, the United States Department of Energy, and the National Institute of Radiological Sciences in Japan.

It was four years ago when I was sitting beside Rick and Marlene Vanasek's pool, not having decided yet whether I was going to pursue graduate research at Colorado State University. They were pleasant yet imposing in convincing me that there was no other reasonable option.

I am in gratitude towards God for my parents, James and Deborah Taddei, and Lyla's parents, David and Susan Thimsen. God has used them to shape our characters and mold our personalities. My mom taught me to think for myself, in essence to think outside of the box, a trait that is a necessity in experimental science. My dad has demonstrated a work ethic and a kindness to which I cannot possibly attain. Over the past four years they have demonstrated love toward us through phone calls, gifts, advice, and visits. And they are truly fantastic grandparents. They have supported us in every fashion that I can imagine.

Last winter I experienced a terrible illness that I feared would take my life. During my illness, I spent several weeks at the home of my sister, Kristen Taddei. While there, aside from necessary time away with her occupation, she never left my side, and she never complained. Her "I'll get it" and "I'll do it" attitude was extraordinary. She really came through for her little brother in a time of desperate need.

My wife, Lyla, is everything I had hoped as a helper and partner. The Lord granted Lyla energy, wisdom, and resolve beyond measure in enduring my illness without ceasing and without exception. Those who watched her care for me experienced a miracle.

Over the past four years while in Fort Collins, Del Hafer has been my spiritual mentor, and Robert Dunn, Ron Goerzen, Terry Gray, Nicholas Kemp, Jonathan Miller, Ronald Spaulding, Martin Thomaz, and Chung-te Tzou have been faithful spiritual brothers. I am thankful to our Lord for how they have kept me "on the sidewalk" with God during our season in Fort Collins.

A graduate research assistantship stipend and benefits are not sufficient to support a family of four, especially through a serious illness. But God was faithful to supply the remainder of our needs as well ("And my God will meet all your needs," Philippians 4:19, NIV) through generous friends and family, who I think would rather be anonymous, and through working with Apartment Life at Colorado State University.

The skills and intuition of my physicians have been literally amazing. I am grateful to God for His healing work through Russell Risma, Michael Thakor, Mehrdad Mazlumzadeh, Roger Shepherd, David Cobb, William O'Halloran, Diane Mahurin, Rod Holland, and the research fellow at the Mayo Clinic who stunned everyone by determining the cause of my illness.

Thanks to my supervisor with Apartment Life, Hosam-Aldeen Ahmad, who, *al-humdu lillah*, was willing to give us time away from Apartment Life duties during my preliminary exam and my illness and health recovery.

DEDICATION

To…

…Lyla—my friend, my helper, my bride

…Amma—my firstborn, who calls me Daddy and watches cartoons with me

…Halima—my secondborn, who calls me Baba and brings my shoes to me in the morning

TABLE OF CONTENTS

LIST OF TABLES

LIST OF FIGURES

CHAPTER I: INTRODUCTION

Human exposure to radiation fields consisting of high atomic number (atomic number, $Z \geq 2$) and high energy (HZE) ions is of concern during manned space missions, near particle accelerators used for research and radiation therapy, and on high-altitude aircraft flights. The radiation environment in space has three primary components: 1) trapped particles in the geomagnetic field of the earth, consisting of protons in altitudes corresponding to low earth orbit and electrons in altitudes corresponding to geosynchronous earth orbit, 2) solar particles, 98% of which are protons, 1% are helium, and 1% are other HZE ions, and 3) galactic cosmic radiation (GCR) having a composition of cations consisting of 87% protons, 12% helium ions, and 1% HZE ions. Fig. 1.1 shows the relative abundance of elemental ions in the GCR spectrum from protons ($Z = 1$) to nickel ($Z = 28$) (Wefel, 1978). Also displayed in the plot is the relative abundance weighted by Z^2. The weighted relative abundance is a measure of the comparative contribution to absorbed dose for each ion. Although the contribution of HZE particles heavier than helium is only about one percent of GCR, their impact on dose is significant. Human exposure to HZE particles from GCR is of concern because the frequency and duration of manned space activities is increasing (National Research Council and Space Studies Board, 1996) and human exploration of Mars is considered to be inevitable (Simonsen, *et al.*, 2000; Cucinotta *et al.*, 2001). A major area of concern

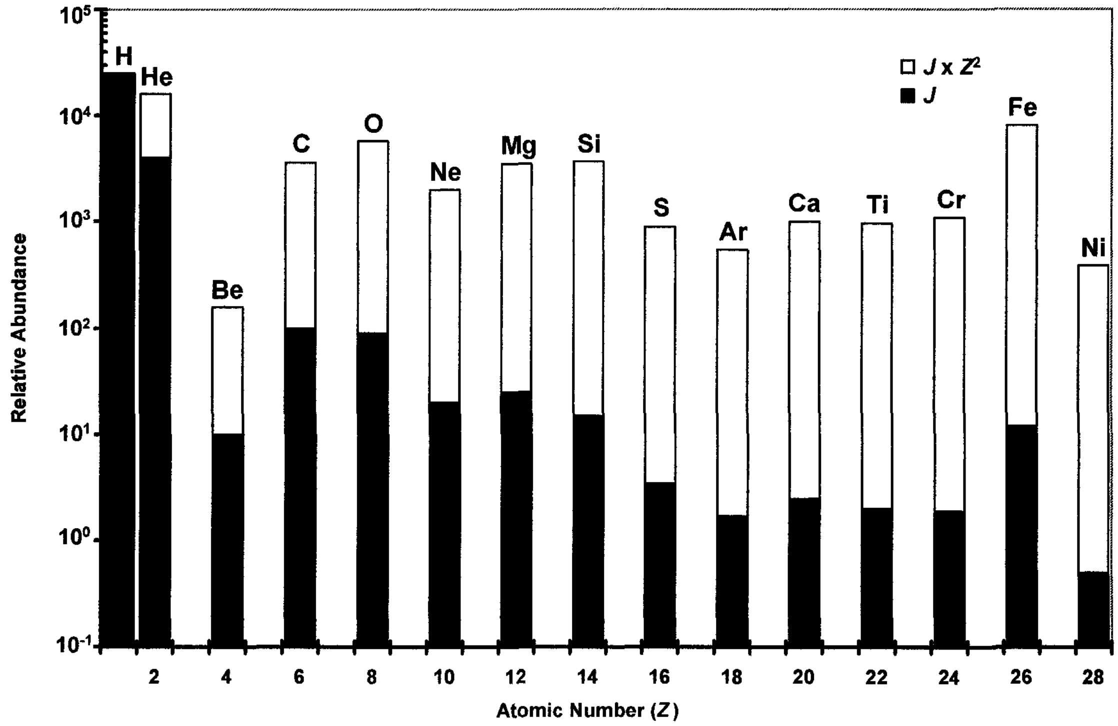

Fig. 1.1. Histogram showing the relative abundances, J, normalized to $J_C = 100$, of the even numbered galactic cosmic ray nuclei (solid bars) compared to these abundances weighted by the square of the charge of the ion to give a measure of the contribution to dose of each element (open bars) (Wefel, 1978).

for the radiation safety of astronauts is the possible detrimental effects, including cancer and other late effects such as hereditary effects, cataracts, and neurological disorders caused by exposure to GCR, trapped particles, and solar particle events (SPE). SPEs are produced by coronal mass ejections from the sun. They can cause an acute exposure to ionizing radiation, and currently their occurrences are unpredictable.

Medical facilities have particle accelerators that generate clinical beams of electrons, photons, and neutrons as well as protons and carbon ions for tumor therapy (GSI, 2004; LLUMC, 2004; NIRS, 2004). In addition to dosimetry for these situations, it is necessary to determine the quality of the incident radiations in order to characterize their relative biological effectiveness (RBE). RBE has been investigated as a function of linear energy transfer.

The unrestricted linear energy transfer, or *LET*, of a particle incident upon a target medium is a scalar quantity defined as

$$LET \equiv \frac{dE}{dx}, \tag{1.1}$$

where *dE* is the mean energy lost by the particle through collisions within the medium and *dx* is the distance traversed by the particle through the medium (Zirkle *et al.*, 1952). *LET* assumes that energy loss occurs only along the trajectory of the primary charged particle. In this sense, energy deposition can only be described when the particle intercepts a point or volume of interest. It neglects the radial dimensions of a track caused by secondary electrons (delta-rays) that can have considerable range when the velocity of the particle is large. Also, it does not consider the random nature of the fluctuations in energy transfer and is an average over large numbers of primary particle interactions (ICRU, 1983). There have been attempts to address this problem by introducing the concept of restricted linear energy transfer, LET_{Δ}, in which dE only includes energy transfers less than some specified value (ICRU, 1968), but this has never been applied to recommendations that formally assess radiation quality. Further, it is very difficult to directly measure LET in tissue.

For radiation protection, a radiation weighting factor, w_r, has been defined to compensate for differences in RBE between different types of radiation. The value of w_r is selected for the type and energy of the radiation incident on the body or emitted by a source within the body. Table 1.1 contains the values of w_r for the types and energy of the radiation selected by the ICRP (ICRP, 1991) and the NCRP (NCRP, 2002). Note that

TABLE 1.1

Selected values of w_r for representative particles from the radiation environment in space (ICRP, 1991; NCRP, 1993).

	w_r	
Particle Type	**ICRP, 1991**	**NCRP, 1993**
x- and γ-rays, electrons, positrons, muons	1	1
< 10 keV neutrons	5	5
10 keV to 100 keV neutrons	10	10
100 keV to 2 MeV neutrons	20	20
2 MeV to 20 MeV neutrons	10	10
> 20 MeV neutrons	5	5
> 2 MeV protons	5	2
alpha particles, fission fragments, nonrelativistic heavy nuclei	20	20

there is no consideration for relativistic heavy nuclei, or HZE ions. Multiplying the absorbed dose averaged over a tissue of organ by the proper w_r yields an equivalent dose that relates the radiation risk of stochastic effects to the specific exposure.

For mixed fields and radiations without a defined w_r, the ICRP has provided a formula for estimating w_r using an average radiation quality factor, $\overline{Q}$, such that

$$\overline{Q} = \frac{1}{D}\int_0^\infty Q(LET)d(LET)dLET\,, \tag{1.2}$$

where D is the total absorbed dose and $d(LET)$ is the measured dose distribution as a function of LET. The accepted value of Q has been defined as a function of LET of the incident particle in water (ICRP, 1991; NCRP, 1993). Table 1.2 shows the ICRP formula for determining $Q(LET)$.

TABLE 1.2

Formula for calculating Q as a function of LET in water (ICRP, 1991).

***LET* in water (keV μm^{-1})**	***Q(LET)***
< 10	1
$10 - 100$	$0.32\,LET - 2.2$
> 100	$300\,LET^{-1/2}$

It has been suggested that radiation quality be estimated based on the lineal energy of the particle. The lineal energy, y, of a single charged particle is a microdosimetric quantity defined as

$$y \equiv \frac{\varepsilon}{\bar{l}}, \qquad (1.3)$$

where ε is the energy deposited by an event in a specified volume, and $\bar{l}$ is the mean chord length of the volume that results if the region of interest is randomly intersected by straight lines (Kellerer and Rossi, 1968), i.e. in the condition of mean free path randomness, or μ-randomness. μ-randomness was defined by Kellerer as the kind of randomness such that a chord is defined by a line extending through a convex body, where the line is prescribed by a point in Euclidian space and a direction, where the point and the direction are from independent uniform distributions (Kellerer, 1971a). For a convex object, traversed by isotropic chords, the mean chord length of the object is given by the Cauchy relation (Turner, 1995),

$$\bar{l} = \frac{4V}{S}, \qquad (1.4)$$

where V is the volume of the object and S is the surface area of the object. Hence, for a spherical volume,

$$\bar{l} = \frac{2}{3}d, \qquad (1.5)$$

where d is the diameter of the volume. y is a stochastic quantity with the same dimensions as *LET* and has been used as a surrogate for *LET* when *LET* cannot be easily measured.

The ideal approach to radiation protection in mixed fields is to use a detector that can measure patterns of energy deposition within volumes of material that are important for biological considerations. It should respond to particles that pass through the volume of interest as well as to delta-rays from particles that pass near but not through this volume. One solution is a tissue-equivalent proportional counter (TEPC). Rossi and Rosenzweig developed the first TEPC to simulate the measurement of energy deposition in volumes of tissue with dimensions similar to the size of the nucleus of a mammalian cell (Rossi and Rosenzweig, 1955). The conventional TEPC used today has a rigid wall made of tissue-equivalent (TE) plastic surrounding a gas-filled cavity. An anode wire extends through the center of this gas cavity. Spherical detectors often have a helical grid wire surrounding the anode in order to form a uniform electric field for ion-pair multiplication. Simulation of energy deposition in volumes with dimensions of a few micrometers is accomplished by operating the TEPC at a low pressure. However, the density difference between the solid wall and the gas cavity can alter the pattern of energy deposition from that in a homogenous medium since the spatial distribution of delta-rays produced in a volume of material is directly related to density of the material. Nevertheless, this type of detector has found wide applications in applied dosimetry.

Careful examination of the response of a TEPC is necessary for a proper interpretation of its response. In recent recommendations for radiation protection for astronauts in space, the NCRP suggested that a TEPC be used as an active area monitor on manned space missions. The NCRP correspondingly issued a call for further study of the response of a TEPC, "Response data for the active and passive devices used should be determined for...high-*Z*, high-energy ions (e.g., helium, carbon, silicon, iron) from 50 MeV n^{-1} to 1 GeV n^{-1}...in fields that are monoenergetic or quasi-monoenergetic" (NCRP, 2002). Nikjoo *et al.* recently made the statement, "Of prime importance are the measurements of absorbed dose and radiation quality (in terms of lineal energy), especially in a mixed field in the environment of the spacecraft" (Nikjoo *et al.*, 2002).

The response of a spherical TEPC with a 2.54-mm-thick wall to HZE ions has been reported previously (Rademacher, 1997; Rademacher *et al.*, 1998; Gersey *et al.*, 2002; Guetersloh, 2003; Guetersloh *et al.*, 2004). These experiments were unique because the TEPC was part of a charged-particle spectrometer which recorded the identity and the trajectory of each incident ion. This made it possible to identify and reconstruct the trajectory of each ion as it passed near or through the TEPC.

Rademacher *et al.* presented results for ^{56}Fe ions at 1050 MeV nucleon^{-1} (velocity relative to the speed of light, $\beta = 0.88$) (Rademacher, 1997; Rademacher *et al.*, 1998). It was observed that only about 80% of *LET* was recorded for ions passing through the center of the detector. The impact parameter, b, is defined as the radial distance from the center of the TEPC. For example, for ions passing through the center of the detector, $b = 0$. The reason that events where $b = 0$ recorded a smaller response than what would be expected based on the product of *LET* and the simulated diameter was attributed to the combined effects of energy escaping the sensitive volume through high energy delta-rays and the enhancement of delta-rays as the ion passed through the forward wall of the detector. In other words, electrons produced in the wall did not fully compensate for delta-rays that escaped the gas cavity. However, as *b* increased, energy deposition became larger than what would be expected from *LET* alone. There was a pronounced enhancement in energy deposition when the impact parameter was very near the radius of the gas cavity. This was attributed to the large number of soft (i.e., low energy) delta-rays produced within the wall but close enough to emerge and deposit energy in the cavity. This effect was later observed in the results of Monte Carlo computations (Nikjoo *et al.*, 2002). Additionally, energy deposition events were recorded from ions that passed through the wall but not through the cavity ($b >$ radius). For a summary of these so-called "wall effects" related to a walled TEPC, see Chapter III: Materials and Methods. The TEPC nevertheless did measure absorbed dose as predicted for a uniform beam of ^{56}Fe at 1050 MeV nucleon^{-1} when all of the events for ions passing both inside and outside of the cavity were included in the energy deposition response, or the "response function," of the TEPC.

Gersey *et al.* extended the above experiment by measuring the response of the TEPC to ^{56}Fe as a function of energy from 200 to 1000 MeV nucleon^{-1} (Gersey *et al.*, 2002). The velocity ranged from $\beta = 0.57$ to $\beta = 0.87$. Patterns of energy escape and wall effects for ions that passed through the wall but not through the gas cavity were observed for all energies. A class of large energy deposition events was also reported, which occurred when the incident ions intercepted the anode wire or helical grid surrounding the anode. Charged-particle equilibrium was satisfied when all events were included in the measurement of absorbed dose.

Expected values, or means, of the y probability density functions, $f(y)$, were computed. The frequency averaged lineal energy, $\bar{y}_f$, is the first moment of y and is determined by (ICRU, 1983)

$$\bar{y}_f = \int y f(y) dy . \tag{1.6}$$

The dose averaged lineal energy, $\bar{y}_D$, is the second moment of y divided by the first moment and is determined by (ICRU, 1983)

$$\bar{y}_D = \frac{\overline{y^2}}{\bar{y}} = \frac{\int y^2 f(y) dy}{\int y f(y) dy} . \tag{1.7}$$

$\bar{y}_f$ was consistently less than *LET*, whereas $\bar{y}_D$ was always within 8% of *LET* for this study. It was suggested that the mean quality factor for ^{56}Fe could be obtained by using $\bar{y}_D$ as a substitute for *LET*.

Guetersloh *et al.* compared the response of a spherical TEPC to ^{14}N, ^{16}O, ^{20}Ne and ^{28}Si particles with different energies but having similar *LET* at 44 ± 2 keV μm^{-1} (Guetersloh, 2003; Guetersloh *et al.*, 2004). Ions that passed through the center of the detector (i.e., $b < 0.8$ mm) deposited only about 80% of the energy that would be expected from the product of *LET* and the diameter. A computational model for a homogeneous geometry indicated that the energy loss due to escaping delta-rays would result in only about 60% of *LET* being deposited by ions passing through the center of the sphere. The difference between the measurements and the calculation was attributed to forward-moving electrons produced in the front wall of the detector. Thus for an impact parameter of zero, the forward contribution of electrons was not sufficient to compensate for the electrons escaping the sensitive volume. However, energy compensation from interactions with the wall exceeded energy loss from outside of the gas when the impact parameter was greater than about 85% of the radius.

The response functions of the TEPC in terms of the distributions of energy deposition events were found to be similar for all four ions with the same *LET*, but there were differences in the response functions for events with very small and large energy deposition. These were shown to be primarily from ions that did not pass through the sensitive volume of the detector. The number of events with very small energy depositions increased as the velocity of the ion increased. This was due to an increase in the energy and corresponding range of the delta-rays produced in the side wall of the detector. Although the incident *LET* remained fairly constant, the ratio of both $\bar{y}_f$ and $\bar{y}_D$ to *LET* decreased as the velocity of the incident ion increased. $\bar{y}_f$ was particularly sensitive to the number of small energy deposition events. This becomes problematic because the signals corresponding to these events can be indistinguishable from electronic noise. They are often eliminated from the spectrum with electronic discriminators even though they reflect actual small energy deposition events.

The similar-*LET* data were used to estimate mean quality factors for applications in radiation protection. Mean quality factors that were estimated using $\bar{y}_D$ as a substitute for *LET* in the formula given by the ICRP (Table 1.2) seemed to be the most stable and accurate since $\bar{y}_D$ was not strongly influenced by changes in the number of very small energy deposition events recorded by the TEPC.

Borak *et al.* measured the response of the TEPC to protons from 50 to 200 MeV ($\beta = 0.33$-0.55) (Borak *et al.*, 2004). For these data, $\bar{y}_f$ was similar to *LET*, whereas $\bar{y}_D$ was approximately 3 times greater than *LET*. This was in contrast to the results for heavy ions reported above. Again, $\bar{y}_f$ was sensitive to the frequency of small energy deposition events that were indistinguishable from noise. If these are not selectively discriminated from background, the detector underestimates $\bar{y}_f$.

The work presented here is an extension of the experiments described above. The objective was to examine the responses of the same spherical TEPC to HZE ions with different atomic number but with similar velocities. The experiments were originally designed to study the response of the TEPC to ion beams consisting of monoenergetic ions with charge from $Z = 2$ to $Z = 26$ and at an energy of 400 MeV nucleon^{-1}. Because of insufficient shielding for radiation safety, however, it was not possible to generate the lighter ions at this energy. Thus the experiment was divided into two groups. One group consisted of data from ^{56}Fe, ^{28}Si, ^{16}O and ^{12}C ions at 376 ± 15 MeV nucleon^{-1} ($\beta = 0.70$), and the other group consisted of data from ^{12}C and ^{4}He ions at 220 ± 7 MeV nucleon^{-1} ($\beta = 0.59$). The reasoning was that the two carbon beams would serve as a link between the two energies. The gas pressure in the TEPC was adjusted to simulate volumes of tissue having diameters of 1 μm for ions with $\beta = 0.70$ and 3 μm for ions with $\beta = 0.59$. The TEPC provided a spectrum of measured energy deposition events, from which were calculated the absorbed dose and radiation quality factor for these heavy ions representative of the GCR spectrum. The data were measured at the Heavy Ion Medical Accelerator in Chiba (HIMAC) facility operated by the National Institute of Radiological Sciences in Chiba, Japan (NIRS, 2004). More than 5×10^5 energy deposition events were recorded for each ion. A summary of the beam characteristics is included in Table 1.3. Position-sensitive detectors (PSDs) were placed both upstream and downstream of the TEPC so that the trajectory could be reconstructed and the identity of each incident ion could be determined. All data were recorded on an event-by-event basis.

TABLE 1.3

Properties of the particle beams from previous HZE studies (Rademacher, 1997; Rademacher *et. al*, 1998; Gersey *et. al*, 2002; Guetersloh, 2003; Guetersloh *et. al*, 2004) and the current HZE study using an identical spherical TEPC.

Ion	*Energy*[a] (MeV n^{-1})	β	d[b] (μm)	*LET* (keV μm^{-1})	*Q(LET)*[c]
		Previous Studies			
^{14}N	79	0.39	1	43.1	11.6
^{16}O	119	0.46	1	40.9	10.9
^{20}Ne	211	0.58	1	43.8	11.8
^{28}Si	781	0.84	1	46.4	12.6
^{56}Fe	200	0.57	1	302	17.3
^{56}Fe	360	0.69	1	214	20.5
^{56}Fe	540	0.77	1	179	22.4
^{56}Fe	700	0.82	1	163	23.5
^{56}Fe	790	0.84	1	157	23.9
^{56}Fe	1000	0.87	1	149	24.6
^{56}Fe	1050	0.88	1	149	24.6
		Current Study			
^{4}He	225	0.59	3	1.68	1.00
^{12}C	215	0.58	3	15.6	2.79
^{12}C	389	0.71	1	11.2	1.38
^{16}O	385	0.71	1	19.9	4.17
^{28}Si	375	0.70	1	61.9	17.6
^{56}Fe	355	0.69	1	219	20.3

[a] Energy at the active volume of the TEPC.

[b] *d* is the simulated tissue diameter of the TEPC.

[c] *Q(LET)* was calculated using the definition from the ICRP (ICRP, 1991).

CHAPTER II: REVIEW OF LITERATURE

RADIATION SAFETY IN SPACE

Radiation Environment in Space

Space is the region beyond the atmosphere of the earth. Ionizing radiations in the space environment are classified into three primary categories: trapped particles, solar particles, and GCR.

Particles contained by the magnetosphere of the earth are called trapped particles. They are composed of mostly protons in low earth orbit and electrons in geosynchronous earth orbit. A special region, called the South Atlantic Anomaly, exists over the South Atlantic Ocean off the coast of Brazil, where the magnetosphere dips into lower altitudes. As a result, the fluence of trapped particles for spacecraft that pass through this region is high. Spacecraft with orbits having inclination between 35 and 60 degrees travel through this region. For example, the International Space Station passes through the South Atlantic Anomaly.

The particle spectrum originating from the sun, or solar particle spectrum, consists mostly of protons but also has a small HZE component. The paucity of HZE data for solar particles makes quantifying their contribution to absorbed dose difficult. As a result, the contribution to dose of HZE ions originating from the sun is considered negligible (NCRP, 2000). Of primary concern for radiation protection for astronauts are solar particle events (SPEs). SPEs are caused by coronal mass ejections of the sun and are periods of immense flux of solar particles. The occurrence of SPEs is not predictable, and they can cause extremely dangerous and even potentially-lethal radiation exposures for astronauts. Solar particles are of concern especially for space travel outside the magnetosphere of the earth.

GCR is isotropic, meaning that it travels in all directions with the same probability, and does not have a known source. It is hypothesized that GCR has existed in space since the creation of the universe. Ninety-eight percent of GCR is made up of protons and HZE ions while the remaining two percent is composed of electrons and positrons. Electrons and positrons are not a concern for radiation safety for astronauts inside spacecraft because they are adequately shielded. The composition of the elemental portion of GCR is 87 percent protons, 12 percent helium, and one percent larger HZE particles (Simpson, 1983). Fig. 1.1 shows the relative abundances of each element of the GCR spectrum. Energies of these particles are on the order of hundreds of MeV nucleon^{-1}. GCR are of concern mainly for space travel outside of the magnetosphere of the earth, for example Lunar or Martian missions.

Shielding and other material in the spacecraft are secondary sources of ionizing radiation in the astronaut habitat (Miller *et al.*, 1998; Cucinotta *et al.*, 2003; Miller *et al.*, 2003). Fragments are created by HZE ions and protons having nuclear interactions with target material. There is no practicable means of shielding the astronauts from radiation in space while avoiding the production of these secondary particles. During an extra-vehicular activity, on the other hand, astronauts are not exposed to secondary ions from the shielding of the spacecraft but are exposed additionally to electrons in space. It is the aim of the National Aeronautics and Space Administration (NASA) in shielding design to maximize the protection from primary particles incident upon the spacecraft and minimize the production of secondary particles (Wilson *et al.*, 1997).

Dose Assessment and Limits for Astronauts

The objective of NASA in dose assessment for astronauts is to "determine the necessary radiation protection quantities for the limitation of stochastic and deterministic effects" (NCRP, 2002). NASA's overall objective in the assessment and control of the radiation exposure to astronauts is to

1) keep individual doses below the established dose limits to avoid deterministic effects;
2) keep accumulated doses over an astronaut's career below the established dose limits for stochastic effects; and
3) keep all astronaut doses as low as reasonably achievable, economic and social factors being taken into account (NCRP, 2002).

Stochastic effects are effects of radiation such that the *probability* of the incidence of a biological effect is a function of absorbed dose. For example, cancer and genetic effects are stochastic effects. Deterministic effects are effects of radiation such that the *severity* of the effect is a function of absorbed dose, which includes a threshold below which the biological effect will not occur. For example, cataracts and sterility are deterministic effects.

The current recommended model of the NCRP for estimating risk of stochastic effects involves the concepts of effective dose and equivalent dose. Effective dose is defined as the following:

$$E \equiv \sum_{T} w_T H_T \,, \tag{2.1}$$

where w_T is the tissue weighting factor (Table 2.1) and H_T is the equivalent dose in an organ or tissue,

$$H_T \equiv \sum_{r} w_r D_{T,r} \,, \tag{2.2}$$

where $D_{T,r}$ is the absorbed dose in an organ or tissue for a radiation type, r. The career

TABLE 2.1

Tissue weighting factor, w_T, values (ICRP, 1991; NCRP, 1993).

Organ or Tissue	w_T
Gonads	0.20
Red bone marrow	0.12
Colon	0.12
Lung	0.12
Stomach	0.12
Bladder	0.05
Breast	0.05
Liver	0.05
Esophagus	0.05
Thyroid	0.05
Skin	0.01
Bone surface	0.01
Remainder	0.05

limits for stochastic effects based on effective dose, which correspond to a lifetime excess risk of cancer mortality of three percent and are specified by sex and age, are given in Table 2.2.

TABLE 2.2

Ten-year career effective dose limits corresponding to a lifetime excess risk of cancer mortality of three percent (NCRP, 2000).

Age at First Exposure (years)	**Female *E* limit (Sv)**	**Male *E* limit (Sv)**
25	0.4	0.7
35	0.6	1.0
45	0.9	1.5
55	1.7	3.0

Dose limits for deterministic effects for astronauts are based on the quantity gray equivalent, which is “the mean absorbed dose in an organ or tissue modified by a recommended value, for radiation protection purposes, of the relative biological effectiveness of a given particle type as given in NCRP” (NCRP, 2002). The conventional notation used for gray equivalent is

$$G_T = R_i D_T, \tag{2.3}$$

where G_T is gray equivalent and R_i is the recommended value of the RBE for particle type i. The unit of D_T is the gray (Gy), and the unit of G_T is the gray equivalent (Gy-Eq). The values of R_i are given in Table 2.3, and the dose limits for deterministic effects are given in Table 2.4.

TABLE 2.3

Recommended RBE, R_i, values for various particle types i (NCRP, 2002).

Particle Type	***R_i (range for the value)***
1 to 5 MeV neutrons	6.0 (4-8)
5 to 50 MeV neutrons	3.5 (2-5)
HZE ions	2.5 (1-4)
Protons > 2 MeV	1.5 (—)

TABLE 2.4

Recommended G_T limits for three deterministic effects (all ages) (NCRP, 2000).

	G_T Limit (Gy-Eq)		
	Bone Marrow	**Lens of the Eye**	**Skin**
Career	—[a]	4.0	6.0
1 year	0.50	2.0	3.0
30 days	0.25	1.0	1.5

[a] The career limits for stochastic effects are sufficient for protection of the bone marrow against deterministic effects for a career.

Quality Factor

Quality factor, Q, is a multiplicative factor that is interrelated with RBE in that it is used to relate a stochastic biological effect of a radiation to a physical absorbed dose. Q was originally useful in estimating a dose equivalent applied to an absorbed dose at a point rather than averaged over a tissue or organ from the radiation at that point. It is a dimensionless quantity, but units of sieverts per gray (Sv Gy^{-1}) may be assigned. For radiation types where w_r is not defined or in mixed or unknown fields of radiation such as in space, an approximation of w_r may be obtained by calculating an average Q as in Equation 1.2,

$$w_r \approx \overline{Q} = \frac{1}{D}\int_0^\infty Q(LET)d(LET)dLET\,.$$

In 1977, the ICRP defined *Q* as a function of *LET* of the radiation in water at the point of interest (ICRP, 1977). This definition is in Table 2.5. Interpolated values of *Q* may be obtained by plotting *Q* versus *LET*.

TABLE 2.5

Previous definition of *Q* as a function of *LET* in water from the ICRP (ICRP, 1977). Interpolated values of *Q* may be obtained by plotting *Q* versus *LET* on a linear-logarithmic plot.

***LET* in water (keV μm^{-1})**	***Q(LET)***
≤ 3.5	1
7	2
23	5
53	10
≥ 175	20

It is difficult to directly measure *LET* in tissue in a mixed radiation field. The ICRU has made a suggestion for estimating quality, *q*, as a function of lineal energy, *y*. Lineal energy was defined (Chapter 1: Introduction) as the energy deposited in a volume of interest divided by the mean chord length of that volume. Lineal energy has the same units as *LET* and has been used as a surrogate for *LET* for estimating radiation quality. The suggestion of the ICRU for a quality function for a spherical volume of tissue with a diameter of 1 μm is

$$q(y) = \frac{a_1}{y}\left(1 - e^{-a_2 y^2 - a_3 y^3}\right), \tag{2.4}$$

where y is in keV μm^{-1}, with the coefficients:

$a_1 = 5510$ keV μm^{-1}
$a_2 = 5 \times 10^{-5}$ μm^2 keV^{-2}
$a_3 = 2 \times 10^{-7}$ μm^3 keV^{-3}

(ICRU, 1986). This relation was based on general observations and theoretical considerations in radiobiology. In particular, special consideration was given to observations on chromosomal aberrations in human lymphocytes.

In response to the urgency of the search for a more consistent convention for estimating radiation quality, Keller and Hahn (1988) made a slight adjustment for small values of y to the ICRU suggestion above. The quality function was estimated as

$$q(y) = 0.3y\left[1 + \left(\frac{y}{137}\right)^5\right]^{-0.4}, \tag{2.5}$$

where y is in keV μm^{-1}.

Quality as a function of *y* may be used to estimate w_r in the microdosimetric event-based approach to estimating equivalent dose described by the NCRP (NCRP, 2001). The concept of having radiation quality decrease below 1 for small and large *y* has been controversial.

The ICRP has defined *Q* as a function of *LET* as shown in Table 1.2 (ICRP, 1991). This definition is currently used as the standard approach for estimating w_r and the accepted value of *Q* for radiation protection in mixed or unknown fields of radiation. To estimate Q in the situation where *y* is measured rather than *LET*, an approximation is made that the dose distribution of *y*, *d(y)*, is identical to the dose distribution of *LET*. This approximation is tested in this study.

A summary of these radiation quality functions is given in Fig. 2.1.

Applications of a Tissue-Equivalent Proportional Counter

A TEPC is a useful device for simulating the measurement of *y* in small volumes of tissue. The NCRP continues to recommend a TEPC for use as an active area monitor in the measurement package of radiation safety management for astronauts (NCRP, 2002):

> *Recommendation 8*: Tissue equivalent proportional counters (TEPC) should be utilized during manned space flight for real-time measurements of absorbed dose and absorbed dose rate, and estimates of quality factor and dose equivalent to a small mass of tissue [*sic*].

Later in the same report, the NCRP suggested, "A TEPC can be placed at fixed locations within the spacecraft or can be operated as a survey meter if necessary."

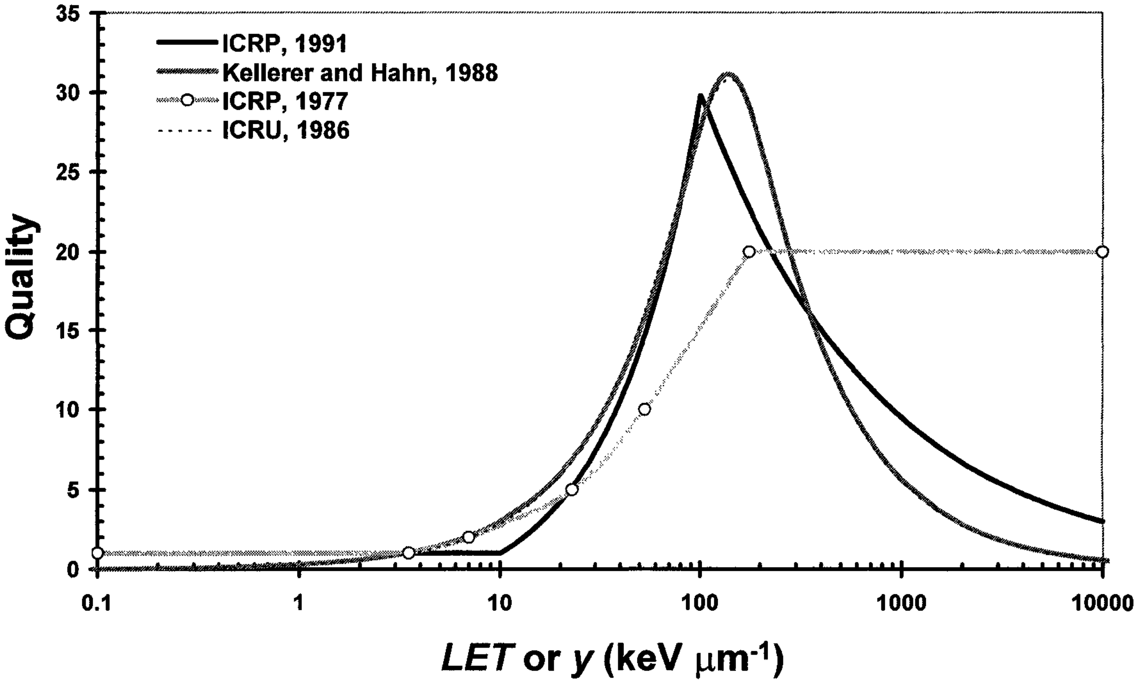

Fig. 2.1. Summary of four methods of estimating radiation quality. The definition of *Q(LET)* from the ICRP (ICRP, 1977) is shown in the lightest shaded line and open circles. The suggestion from the ICRU (ICRU, 1986) for *q(y)* is shown with a dashed line and is nearly identical to the recommendation of Kellerer and Hahn (Kellerer and Hahn, 1988) shown in the moderate shade of gray. The current standard definition of *Q(LET)* from the ICRP (ICRP, 1991) is shown with a solid black line.

A TEPC has been flown in recent years on NASA manned space flights, including Space Transport Shuttle and International Space Station missions (Badhwar, 2000; Doke *et al.*, 2001; Badhwar, 2002). Other applications of the TEPC have included microdosimetry on MIR (Bottollier-Depois *et al.*, 1996; Badhwar *et al.*, 1997; Cucinotta *et al.*, 2000), on aircraft flights (Chee *et al.*, 2000; Lindborg *et al.*, 1999; Tume *et al.*, 2000; Walters *et al.*, 2000), and near therapy beams (Burmeister *et al.*, 2002).

Contributions from this Work

This dissertation is a report of the characterization of the response of a spherical TEPC to different HZE ions having similar velocities. It is a contribution to a broader collection of studies of the response of an identical TEPC to HZE ions of various energies and atomic numbers from ^{4}He to ^{56}Fe. Incident ions used in this particular study were ^{56}Fe, ^{28}Si, ^{16}O and ^{12}C at 376 MeV nucleon^{-1} ($\beta = 0.70$) and ^{12}C and ^{4}He at 220 MeV nucleon^{-1} ($\beta = 0.59$). Previous experiments focused on the response of a TEPC to a 1.05-GeV nucleon^{-1} ^{56}Fe beam (Rademacher, 1997; Rademacher *et al.*, 1998), the response of a TEPC to HZE ions having the same atomic number but with different energies using ^{56}Fe beams of between 200 and 1000 MeV nucleon^{-1} (Gersey *et al.*, 2002), and the response of a TEPC to HZE ions of the same *LET* of 44 keV μm^{-1} (Guetersloh, 2003; Guetersloh *et al.,* 2004). The ions used in this collection of studies are summarized in Table 1.3.

Also related to this study is an investigation involving the response of the same TEPC to protons of energies characteristic of protons in the South Atlantic Anomaly (Borak *et al.*, 2004).

CHAPTER III: MATERIALS AND METHODS

Facility and Ion Beam Properties

Experiments were performed at the HIMAC facility operated by the National Institute of Radiological Sciences in Chiba, Japan (NIRS, 2004). HIMAC employs two synchrotrons along with an Alvarez-type, standing wave drift tube linear accelerator. The facility is capable of accelerating a large selection of ions from protons to xenon with energies ranging from 100 to 800 MeV nucleon^{-1}. The entire accelerating system has a cycle of 3.3 seconds. Beams of protons and heavy ions can be focused to create small, uniform beams. The ion beams serve two purposes—they are used for charged-particle therapy during the day and for scientific research at night and on weekends, including physics, chemistry, biology, and engineering experiments. It is therefore possible to design research experiments for radiation physics and biology using heavy ions that are similar to ions characteristic of the radiation environment in space. For these experiments, HZE beams were defocused to uniform distributions approximately 20 mm in diameter, and the beam intensity was adjusted to approximately 1000 particles per spill (i.e., beam extraction). Each spill lasted approximately one second.

A TEPC was exposed to accelerated beams of ^{12}C, ^{16}O, ^{28}Si, and ^{56}Fe ions at $\beta =$ 0.70 (376 ± 15 MeV nucleon^{-1}) and ^{4}He and ^{12}C ions at $\beta = 0.59$ (220 ± 7 MeV nucleon^{-1}), where β is the velocity of a ion relative to the speed of light

$$\beta = \sqrt{\frac{E^2 - M_0^2 c^4}{E^2}}, \tag{3.1}$$

E is the total energy of the ion, M_0 is the rest mass of the ion (for specific beam characteristics, see Table 1.3), and c is the speed of light. The maximum energy of the delta-rays from an incident ion may be determined using the following equation (Attix, 1986):

$$E_{\delta,max} = \frac{2mc^2\beta^2}{1-\beta^2}\left[1 + \frac{2m}{M}\cdot\frac{1}{\sqrt{1-\beta^2}} + \left(\frac{m}{M}\right)^2\right] \tag{3.2}$$

where m is the mass of an electron and M is the mass of the incident ion. For HZE ions ($M >> m$) where the velocity of the ion is not approximately equal to the speed of light (β not ≈ 1), this equation may be simplified to

$$E_{\delta,max}(\mathrm{HZE}) = \frac{2mc^2\beta^2}{1-\beta^2}. \tag{3.3}$$

This is the case for the HZE ions characteristic of the GCR, which have energies on the order of hundreds of MeV nucleon^{-1} or a few GeV nucleon^{-1}. The maximum energies of delta-rays from ions with velocities, $\beta = 0.70$ and $\beta = 0.59$, are 0.979 MeV and 0.546 MeV, respectively. The ranges based on the continuous slowing down approximation for the maximum energy delta-rays in low-*Z* materials, e.g., A-150®[1] TE plastic, are (Turner, 1995)

$$R_{\delta,max}\left(\text{g cm}^{-2}\right)=\begin{cases}0.412\,E_{\delta,max}^{1.27-0.0954\ln\left(E_{\delta,max}\right)}, & 0<E_{\delta,max}\le 2.5\\ 0.53\,E_{\delta,max}-0.106, & E_{\delta,max}>2.5\end{cases}\tag{3.4}$$

and are equal to 3.76 mm and 1.78 mm in A-150 TE plastic for $\beta = 0.70$ and $\beta = 0.59$ ions, respectively.

Tissue-Equivalent Proportional Counter

A TEPC is a gas-filled detector operated in the proportional region. It is filled with TE gas, and it measures energy deposited in the gas. TEPCs are manufactured in various sizes and shapes, most commonly of cylindrical or spherical shape. The physical dimensions of a TEPC may vary from fractions of a centimeter to tens of centimeters. Because of its large dynamic range in energy deposition response, which extends from a few hundred eV to thousands of keV, a walled TEPC is sensitive to photons, neutrons, and charged particles from electrons to protons and heavy ions. For spherical TEPCs, often a helical grid wire is added around the anode wire in order to produce a uniform electric field near the anode. Data from a TEPC are recorded on an event-by-event basis so that a distribution of energy deposition events may be displayed, stored, and transmitted. The distribution of energy deposited may be integrated to generate absorbed dose and absorbed dose rate and may be used to estimate quality factor.

---

[1] Standard Imaging, Inc., 7601 Murphy Drive, Middleton, Wisconsin 53562-2532

Target media with similar compositions and density thicknesses (i.e., density of media × thickness of media) have similar cross sections for ionization at the atomic and molecular levels and similar energy transfer characteristics. Therefore, media composed of TE materials may be used to simulate tissue for the purposes of radiation protection. The gas pressure of a TEPC may be adjusted to simulate small volumes of tissue with dimensions on the order of the size of a mammalian cell nucleus. Modern detectors are now being designed to simulate small volumes of tissue with dimensions on the order of a nanometer, which is on the order of the diameter of a DNA molecule (Garty *et al.*, 2002). For a tissue sphere of diameter, d_T, and a gas sphere of diameter, d_G, the condition of simulation, where the energy loss of passing charged particles is identical in the tissue sphere and the gas sphere for equivalent trajectories is

$$\Delta E_T = \left(\frac{S}{\rho}\right)_T \rho_T d_T = \left(\frac{S}{\rho}\right)_G \rho_G d_G = \Delta E_G \tag{3.5}$$

where ΔE_T and ΔE_G are the mean energy losses of the charged particles in tissue and gas, $\left(\frac{S}{\rho}\right)_T$ and $\left(\frac{S}{\rho}\right)_G$ are the mass stopping powers of the tissue and gas, and ρ_T and ρ_G are the densities of the tissue and gas, respectively (ICRU, 1983). Therefore, when using a gas that has a mass stopping power equal to and an atomic composition similar to that of tissue (i.e., tissue-equivalent), to calculate the simulated tissue diameter for a TEPC the following relationship may be used:

$$\rho_T d_T = \rho_G d_G. \tag{3.6}$$

For example, for a spherical detector that is 12.7 mm (one-half inch) in diameter, a propane-based TE gas pressure of 33 Torr, or a gas density of 7.78×10^{-5} g cm^{-3}, may be used to simulate a tissue diameter of 1 μm (For a detailed calculation, see Appendix A: Simulated Diameter Calculation). Ideally, then, the response of a TEPC can characterize energy deposition patterns from incident radiation in a cell nucleus for the purpose of radiation protection.

For general use of a TEPC, it is important that the wall of a TEPC be manufactured with material that is electrically conductive, able to be easily constructed, and be reactive to incident uncharged particles such as photons and neutrons. In this study, since the response of tissue was being simulated, it was additionally imperative that the TEPC wall be composed of TE material.

The signal generated by a TEPC is proportional to the energy deposited in its gas cavity through ionization events. A first approximation of the energy deposition response of the TEPC is related to *LET* of the incident ion, such that

$$\varepsilon = LET \times x, \tag{3.7}$$

where ε is energy deposition and x is the path length through the volume.

Four types of wall effects can distort the response of gas cavities used to simulated small volumes, such as in the case of a TEPC (Rossi, 1967; Oldenburg and

Booz, 1970; Kellerer, 1971a; Kellerer, 1971b; Kellerer, 1971c; ICRU, 1983). First, the "delta-ray effect" occurs when one or more delta-rays produced in the wall enter the gas cavity with or without the incident charged particle. In an actual microscopic region, for example a cell nucleus, only one of the particles would enter the target of interest. Secondly, the "re-entry effect" occurs when an delta-ray exits the gas cavity and, because of the high relative density of the wall, has sufficient curvature in its track to re-enter the gas cavity. In a true microscopic region, the electron has a much lower probability of re-entering the gas cavity. The third type of wall effect, called the "V-effect," occurs when the incident charged particle interacts with at least one atomic nucleus such that two or more nuclear fragments enter the gas cavity. In reality, only one particle would likely enter the microscopic region of interest. Finally, the fourth effect, called the "scattering effect," occurs when two or more charged particles enter the gas cavity as a result of a primary uncharged particle, for example a photon or a neutron, interacting with the wall. A combination of effects could also occur in a single recorded event. In the case of the response of a walled TEPC to HZE ions, two of these wall effects, the delta-ray effect and the V-effect, are most common. The effects of these two on the response of the TEPC are detailed in Chapter IV: Results and Discussion.

In summary, a TEPC is advantageous for radiation protection purposes in that it can simulate the measurement of energy deposition in small volumes of tissue, its data are recorded on an event-by-event basis and can be displayed, stored, and transmitted, and it has a large dynamic range. The disadvantages of using a TEPC to simulate energy deposition patterns in a small volume of tissue are that the wall effects that would not occur in an actual microscopic target, its response in lineal energy depends on the geometry of the site, and it does not directly measure *LET*, making an estimation of quality factor difficult.

Detectors used in this study

Tissue-Equivalent Proportional Counter

The orientation of the detectors used in this investigation is shown in Fig. 3.1. The same spherical research TEPC[2] (Rossi type, serial number 1376) with a sensitive volume diameter of 12.7 mm (0.5 inch) and wall thickness of 2.54 mm (0.1 inch) was used in all experiments and was identical to the instrument used in previous studies (Rademacher, 1997; Rademacher *et al.*, 1998; Gersey *et al.*, 2002; Guetersloh, 2003; Guetersloh *et al.*, 2004; Borak *et al.*, 2004).

Fig. 3.2 is a diagram of the active components of the TEPC. The TEPC signal is collected to a single anode wire encircled by a helical grid wire. The diameter of the helix is 1.3 mm (0.05 inches) and the coil density of the helix is 0.7 mm coil^{-1} (0.03 inches coil^{-1}). The diameter of the wires is 0.046 mm (0.0018 inches). The wall of the TEPC used in this study is composed of A-150 TE plastic. For this particular TEPC, there is a small fill hole in the wall through which the gas within the wall can be in equilibrium with the gas outside of the wall. Additionally, there is a slit in the wall that acts as a collimator, allowing alpha particles emitted from a ^{244}Cm alpha source to enter the active volume and cross its diameter. The detector is housed in a vacuum-tight, 0.007-inch-thick aluminum shell. The aluminum shell and attached 10-inch-long stem are completely submersible and capable of operating in any common fluid.

---

[2] Far-West Technology, Inc., 330 South Kellogg Avenue, Suite D, Goleta, CA 93117

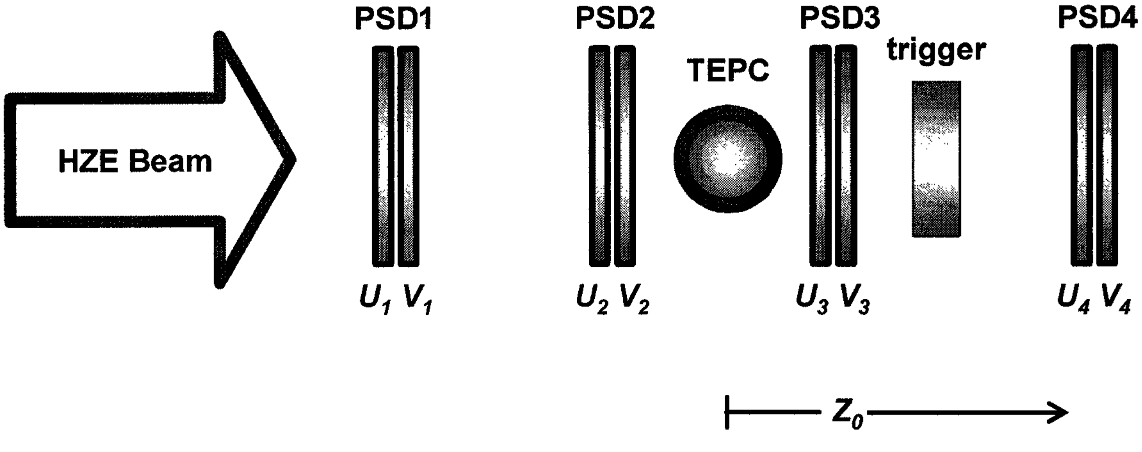

Fig. 3.1. The experimental arrangement of the detectors, showing the position (not to scale) of the TEPC relative to the position-sensitive silicon detectors, labeled PSDi. The detector labeled "trigger" was a 3-mm-thick lithium-drifted silicon detector whose signal allowed or denied the processing of an incident ion event.

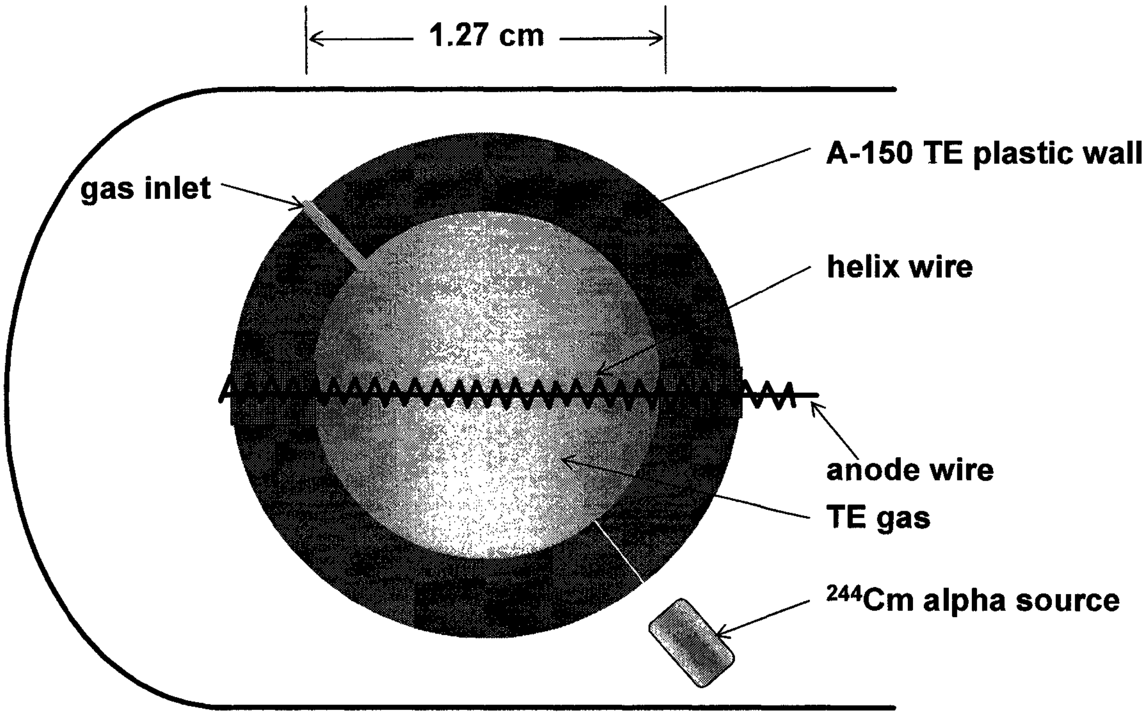

Fig. 3.2. Diagram of the spherical tissue-equivalent proportional counter used in this study. The detector is housed in a vacuum-tight aluminum shell. The gas cavity is surrounded by A-150 tissue-equivalent plastic wall and filled with propane-based tissue-equivalent gas. The pressure of the gas may be adjusted to simulate small volumes of tissue with dimensions on the order of the size of a mammalian cell nucleus. On the lower-right of the detector is a ^{244}Cm alpha source with a gravity-controlled shutter. Traversing the diameter of the gas cavity in the detector are the anode and helical wires held in place by insulating material. Two holes exist in the wall: 1) an opening to bring the gas inside the wall into equilibrium with the gas outside the wall (upper-left) and 2) a gap that acts as a collimator to allow alpha particles originating in the alpha source to cross directly through the gas with a pathlength through the active volume equal to the diameter of the cavity (lower-right).

A Tennelec TC 954A[3] high voltage power supply for the TEPC was set to 595 V for the $\beta = 0.70$ ions and 610 V for the $\beta = 0.59$ ions. These high voltage levels were chosen so that the TEPC would operate in true proportional mode, achieve a gas gain high enough to record small energy deposition events above the electronic noise, and yet remain slightly below the high voltage level that causes electrical breakdown of the gas, or “arching” (Gerdung *et al.*, 1995).

The composition of the propane-based TE gas used at HIMAC is essentially identical to the ICRU standard TE gas composition (Srdoc, 1970; ICRU, 1984; ICRU 1993) and is shown in Table 3.1. The density of the propane-based TE gas in the TEPC was adjusted to 33 Torr to simulate a tissue diameter of 1 μm for the higher-velocity ions and 99 Torr to simulate a tissue diameter of 3 μm for the lower-velocity ions (Waker, 1995). A larger simulated diameter was used for the lower-velocity ions in order to

TABLE 3.1

Composition of propane-based, tissue-equivalent gas.

Compound	**ICRU, 1984; ICRU, 1993**	**HIMAC gas**
	% by volume	
Propane, C_3H_8	55.0	54.9
Carbon dioxide, CO_2	39.6	39.8
Nitrogen, N_2	5.4	5.34

[a] The standard propane-based, tissue-equivalent gas mixture recommended by the ICRU was optimized by Srdoc (Srdoc, 1970).

---

[3] Oxford Instruments, Inc., Nuclear Measurements Group, 601 Oak Ridge Turnpike, P.O. Box 2560, Oak Ridge, Tennessee 37831-2560

increase the signal by about a factor of three. This is particularly important for low-*LET* ions because the response function of the TEPC for these ions extends into the noise distribution of the detector. Over 5×10^5 events were recorded for each ion.

The TEPC was calibrated using an internal ^{244}Cm alpha source as well as an external plutonium-beryllium neutron source, giving a total of four calibration points. Alpha particles from the internal ^{244}Cm alpha source passed through a very small hole in the TEPC wall that acted as a collimator. These alpha particles had trajectories through the diameter of the gas cavity and thus a simulated path of 1 μm or 3 μm for a density of 1 g cm^{-3}. These alpha particles are stopped by a gravity-controlled shutter when used in normal operation mode. A distribution of alpha particles interacting with the central anode of the TEPC provided a calibration point corresponding to a path of approximately one half of the diameter since these alpha particles stopped in the anode wire. An alpha edge was also observed for alpha particles nearing the end of their range. For the external neutron source, the point of maximum energy deposition by recoil protons, or the "proton edge," was the fourth calibration point (for a detailed description of the calibration technique, see Appendix B). An EG&G ORTEC[4] research pulser was also used to further establish the linearity of the data acquisition system, ensuring that the four calibration points found by the source method could be related to energy deposition events in all other channels.

---

[4] EG&G ORTEC, 801 South Illinois Avenue, Oak Ridge, TN 37830

Silicon Detectors

The TEPC was placed within four pairs of position-sensitive lithium-drifted silicon detectors (PSDs) that served as a charged-particle spectrometer (Wong *et al.*, 1990; Zeitlin *et al.*, 1994). Each pair is labeled "PSD1," "PSD2," "PSD3," and "PSD4" in Fig. 3.1. Two PSD pairs were mounted upstream of the TEPC, and two downstream. PSD2 and PSD3 were placed a few centimeters away from the TEPC while PSD1 and PSD4 were placed about 50 cm away from the TEPC.

The PSDs were fabricated in the shape of circular disks having active areas with a radius of 22 mm and thicknesses between 800 and 1050 μm. The total charge from interactions with the incident charged particle was collected on one side of the detector and was proportional to the total amount of energy deposited in the PSD. Since the amount of energy deposited is proportional to Z^2, this signal was used in off-line analysis to identify the ion. On the opposite side of the detector, charge was divided between the left (q_1) and right (q_2) of each horizontal PSD, or the top (q_1) and bottom (q_2) of each vertical PSD. The relative amounts of charge collected in q_1 and q_2 were used to determine the horizontal (U_i) or vertical (V_i) coordinates of the incident ion while passing between each PSD pair, *i*. The total energy deposited as well as the transverse locations within the detectors were recorded for each event. The third spatial dimension (Z_0) of the ion was provided by the physical location of the PSD along the beam axis.

An additional lithium-drifted silicon detector (Zeitlin *et al.*, 1994), labeled "trigger" in Fig. 3.1, was mounted downstream of the TEPC. This detector had a thickness of 3.0 mm and an active area radius of 12.7 mm. The silicon detector was used primarily to increase the efficiency of data acquisition system by allowing it to process only events that had energy deposition characteristic of the incident ion.

Data Acquisition System

Two trigger signals were used with the data acquisition system—one from the trigger silicon detector and one from the TEPC. Triggering was done both with and without the trigger silicon detector and the TEPC in coincidence for all ions with the exception of ^{16}O at 385 MeV nucleon^{-1} (an explanation for this exception is in Chapter IV: Results and Discussion). The fast-timing signal from the preamplifier of the TEPC was selected for use as the TEPC trigger signal. For each trigger, the energy signal from the TEPC was sent first to an external EG&G ORTEC 142AH charge-sensitive preamplifier and then split into two EG&G ORTEC 572 shaping amplifiers, one with a lower gain and one with a higher gain. The difference in amplification between the two shaping amplifiers was optimized to obtain detailed information on the full spectrum of energy deposition events. Each signal from the PSDs, the trigger detector, and the shaping amplifiers were sent to dedicated peak-measuring analog-to-digital converters. The data were saved to disk on an event-by-event basis. A schematic of the data acquisition system is shown in Fig. 3.3.

Off-line Analysis

Off-line data analysis began by selecting events where only the incident ion of interest interacted with the silicon detectors. Since energy deposition in each PSD was proportional to Z^2 of the ion, a prominent peak in the total energy deposited signal

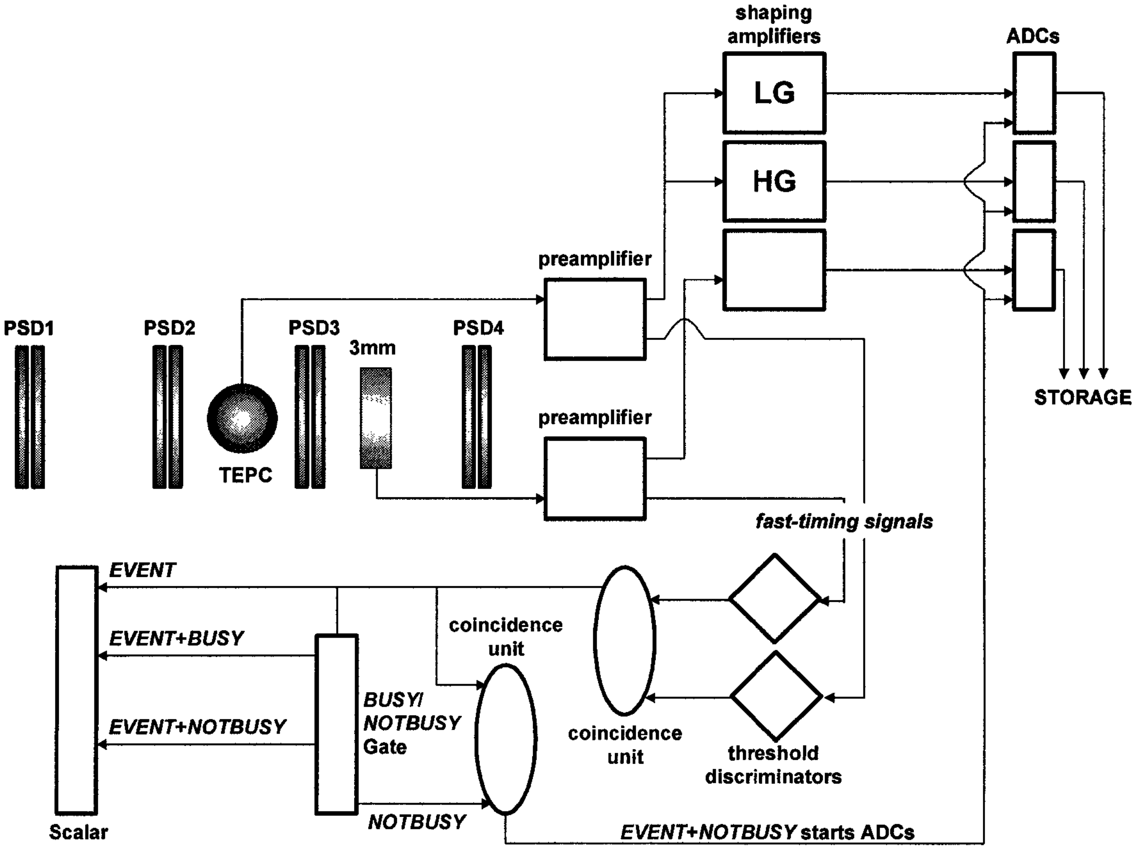

Fig. 3.3. Logic pathway for triggering data acquisition. Fast-timing outputs are used for the logic pathway eventually arriving at the ADCs. Shaped outputs are sent directly to their dedicated ADCs waiting for the state "*EVENT+NOTBUSY*" to trigger signal conversion to digital. If "*EVENT+BUSY*" is found, then only the scalars are incremented (Guetersloh, 2003).

corresponded to the primary incident ion (see Fig. 4.1). Spurious events from fragments and noise contributed to smaller, less developed peaks and wide tails in the energy deposited spectra of the PSDs. Only signals that were within the full width at five percent of the maximum of this peak were chosen as incident ion events. Elimination of all events that were not in the peak corresponding to the primary ion for each PSD ensured that the incident ion passed through the entire spectrometer. PSD4 was placed far downstream of PSD3. Because of the possibility of interactions downstream from the TEPC, its energy deposition signal was not used to eliminate spurious events.

The PSDs also measured each Cartesian coordinate of the incident ion as it traveled through each PSD pair. A procedure using a carefully machined 25.4-mm-thick, brass grid collimator (Fig. 3.4) was used to calibrate the coordinates recorded by each PSD (Wong *et al.*, 1990). Dedicated runs were taken for each ion beam and each PSD pair with the collimator placed immediately upstream of the PSD pair with the exception of ^{16}O at 385 MeV nucleon^{-1} (an explanation for this exception is in the next paragraph). During off-line analysis, events with a smaller total energy deposition in the PSDs indicated incident ions of higher energy. These ions did not slow down in the brass collimator because they traveled through the holes. They had a noticeable peak in the total energy deposition spectra of each PSD and were selected from the data. The mean coordinates, U_i-V_i, for each PSD pair, i, corresponding to each hole in the collimator was calculated. With these data from each collimator run, in order to calibrate the position signals from the PSDs a third-order multiple regression model for each PSD pair, i, of the form

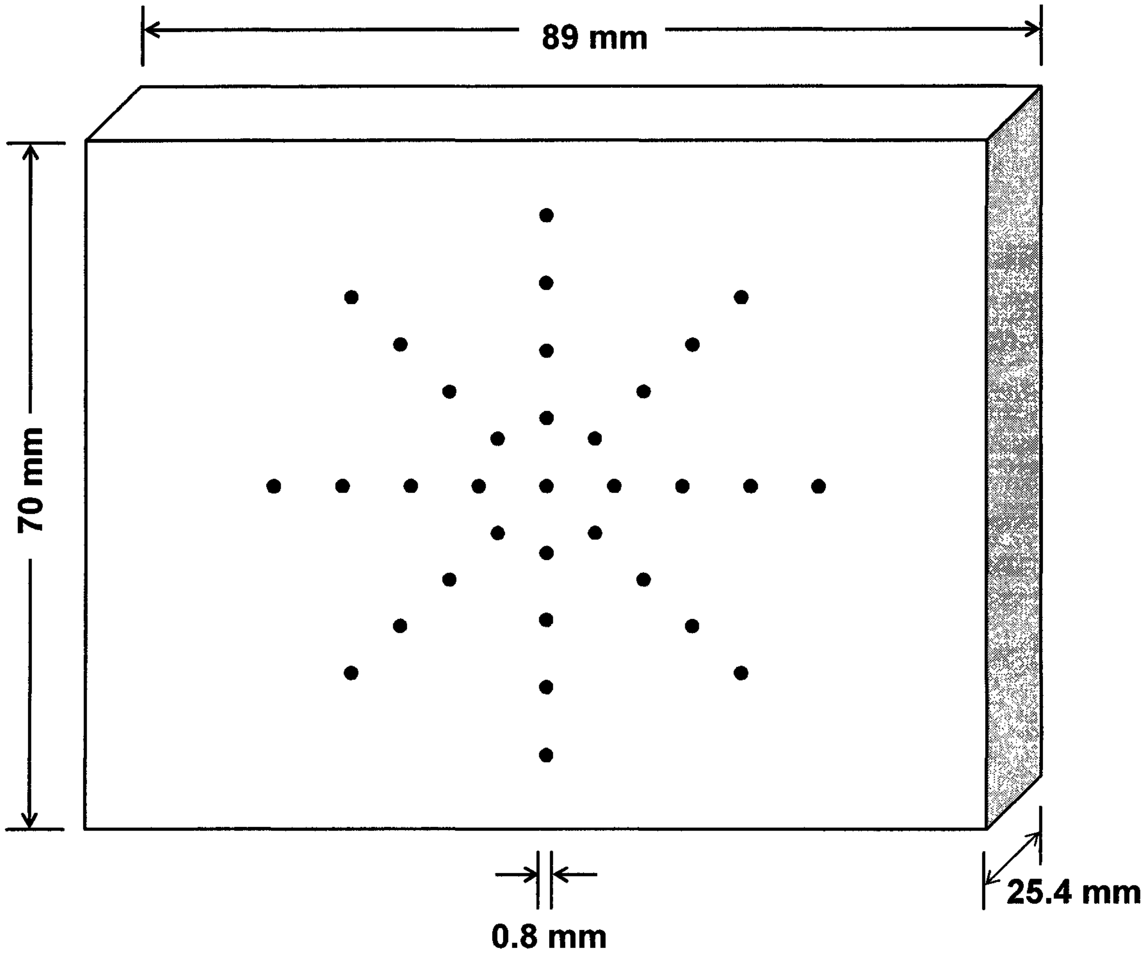

Fig. 3.4. A diagram of the brass grid collimator that was used in the position calibration runs for the PSDs. The radius of each concentric circle through the holes of the collimator increases radially stepwise by 6.35 mm.

$$X_i = \gamma_1 U_i + \gamma_2 V_i + \gamma_3 U_i V_i + \gamma_4 U_i^2 + \gamma_5 V_i^2 + \gamma_6 U_i^2 V_i + \gamma_7 U_i V_i^2 + \gamma_8 U_i^3 + \gamma_9 V_i^3 \qquad (3.8)$$

for the horizontal coordinate and

$$Y_i = \gamma_{10} U_i + \gamma_{11} V_i + \gamma_{12} U_i V_i + \gamma_{13} U_i^2 + \gamma_{14} V_i^2 + \gamma_{15} U_i^2 V_i + \gamma_{16} U_i V_i^2 + \gamma_{17} U_i^3 + \gamma_{18} V_i^3 \qquad (3.9)$$

for the vertical coordinate was selected and the coefficients, γ_1 through γ_{18}, were calculated by both taking into account the results of the backward elimination method with $\alpha = 0.5$ (Ott, 1993) and minimizing the C_p statistic (Mallows, 1973). All interaction terms were considered in the model selection, and lower-order hierarchical terms were included in the final models. The result was in effect a mapping of the measured coordinates, U_i and V_i, into the true coordinates, X_i and Y_i, within each PSD pair, i (e.g., Fig. 3.5).

This entire procedure was undertaken for all ion beams with the exception of ^{16}O at 385 MeV nucleon^{-1}. For the ^{16}O data, position mapping was performed using the regression from the ^{56}Fe at 355 MeV nucleon^{-1} data. The ^{56}Fe data was recorded with an identical experimental setup and gain settings on position signals of the PSDs.

Since it was not possible to mount the PSDs such that their centers were absolutely on the beam axis, each PSD pair had its own coordinate system. Therefore, it was necessary to align the PSD coordinate systems relative to each other. The coordinates of PSD2, PSD3, and PSD4 were aligned to the PSD1 coordinates by first

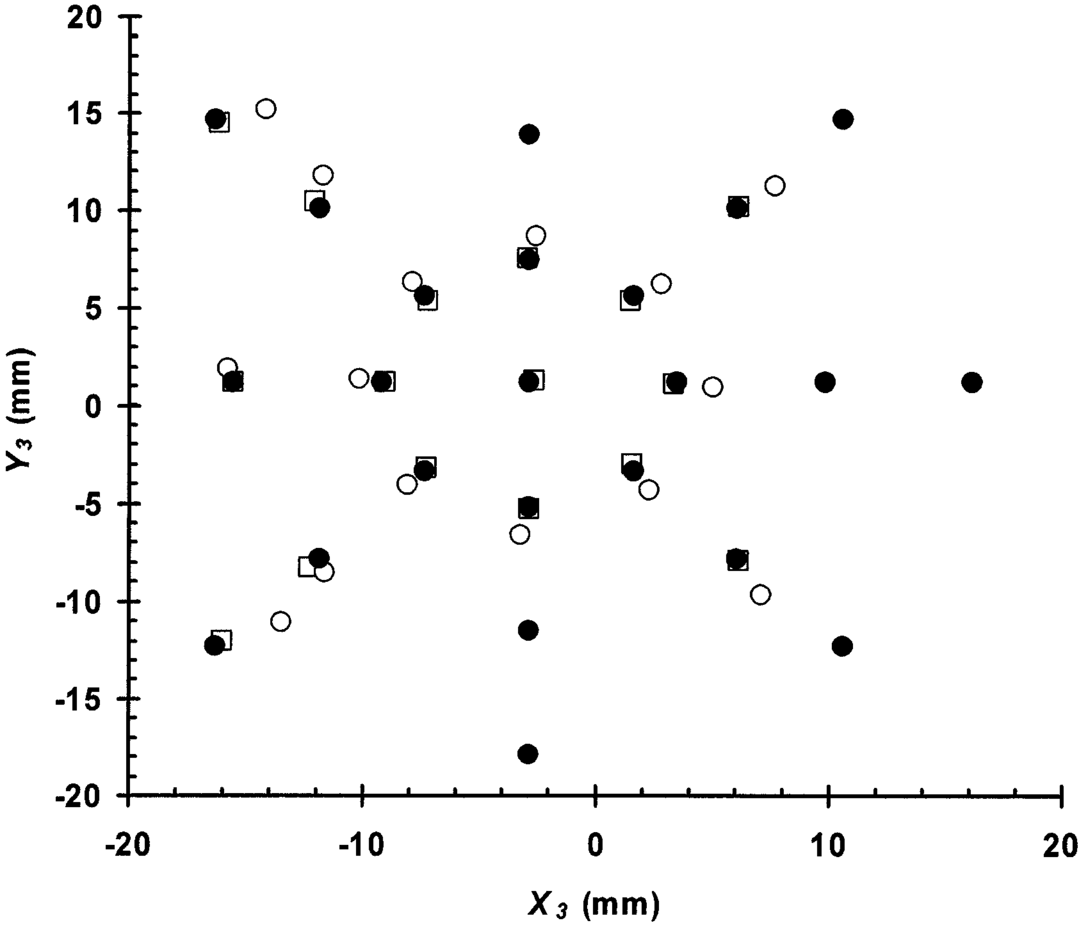

Fig. 3.5. A comparison of the Y_3 vs. X_3 coordinates of the holes in the brass mask (solid circles), the actual response of PSD3 (open circles), and the mapped coordinates by the selected model (open squares) for ^{28}Si at 375 MeV nucleon^{-1}.

projecting a 2-mm × 2-mm area about the origin ($-1 < X_1 < 1, -1 < Y_1 < 1$) of events in PSD1 onto the two-dimensional positional response of the other PSDs, then taking the means of the horizontal and vertical coordinates of each projection, and finally shifting the origin of the coordinates of each PSD pair vertically and horizontally as necessary. For example, Fig. 3.6 shows the projection of the selected region in PSD1 onto PSD2 for ^{12}C at 389 MeV nucleon^{-1}. In this case, X_2 was shifted by subtracting 0.89 mm, and Y_2 was shifted by subtracting 2.64 mm.

After aligning the PSD coordinate systems, transverse positions recorded in PSD2 and PSD3 were used to reconstruct the transverse coordinates, X_0 and Y_0, of the ion at the longitudinal position corresponding to the center of the TEPC ($Z_0 = 0$) using the equations,

$$X_0 = X_3 - Z_{3X} \cdot \frac{X_3 - X_2}{Z_{3X} - Z_{2X}} \tag{3.10}$$

for the horizontal transverse coordinate and

$$Y_0 = Y_3 - Z_{3Y} \cdot \frac{Y_3 - Y_2}{Z_{3Y} - Z_{2Y}} \tag{3.11}$$

for the vertical transverse coordinate, with Z_{ij} such that j denoted either the horizontal or vertical coordinate in the PSD pair, i.

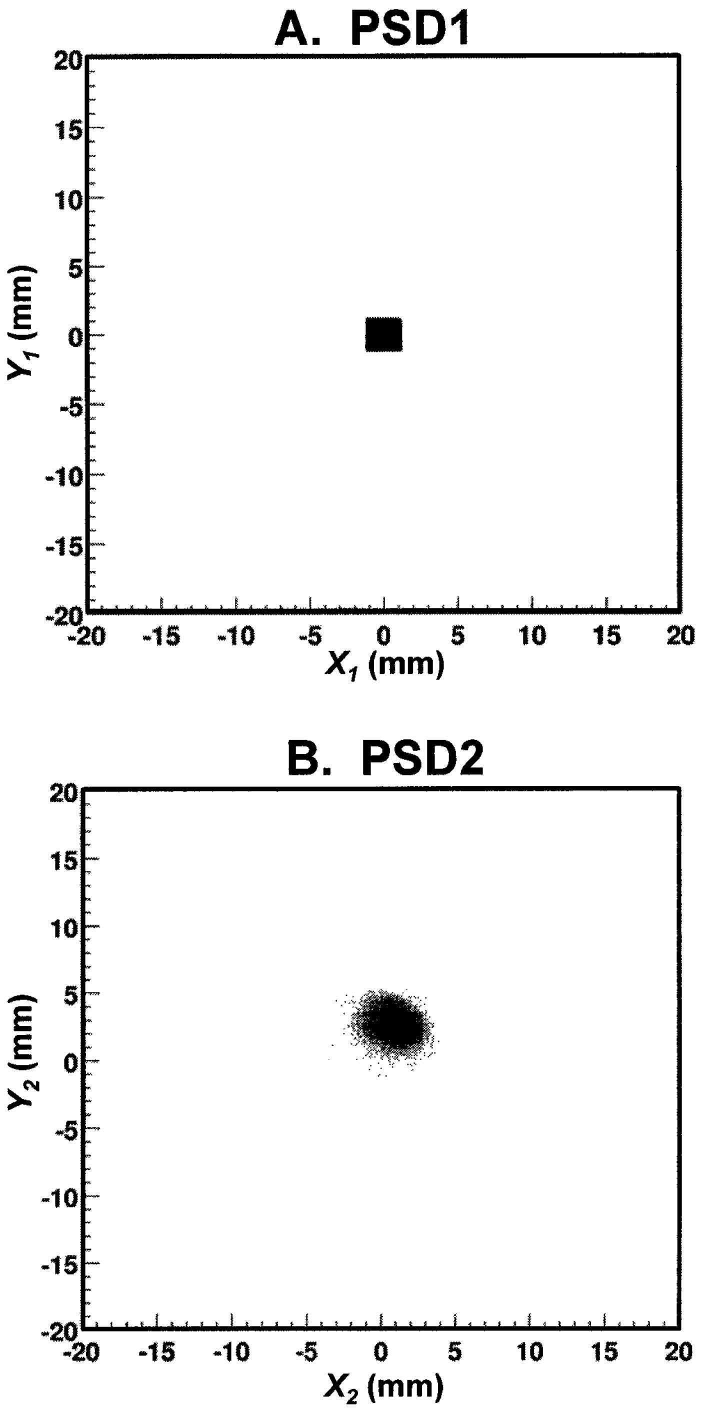

Fig. 3.6. Events selected from PSD1 before alignment, where $-1 < X_1 < 1$ and $-1 < Y_1 < 1$ shown in the PSD1 coordinate system (A) and projected onto the PSD2 coordinate system (B) for the ^{12}C at 389 MeV nucleon^{-1} data.

Finally, the center of the transverse coordinates, (X_0,Y_0), were transposed so that (0,0) corresponded to the center of the TEPC. The center of (X_0,Y_0) was determined by selecting small energy deposition events from the response function of the TEPC, where the incident ion traveled through the wall of the TEPC. A two-dimensional circular plot of Y_0 versus X_0 was created (Fig. 3.7). The center of these events was estimated, tested by other distributions that corresponded to the wall of the TEPC, and adjusted accordingly, and the X_0-Y_0 coordinate system was shifted from the center of these events to (0,0). In the case of ^{28}Si at 375 MeV nucleon^{-1}, X_0 was transposed by adding 4.1 mm, and Y_0 was transposed by adding 1.0 mm.

The impact parameter, b, was defined as the radial distance from the center of the TEPC to the location of the event at $Z_0 = 0$, so

$$b = \sqrt{X_0^2 + Y_0^2} \, . \tag{3.12}$$

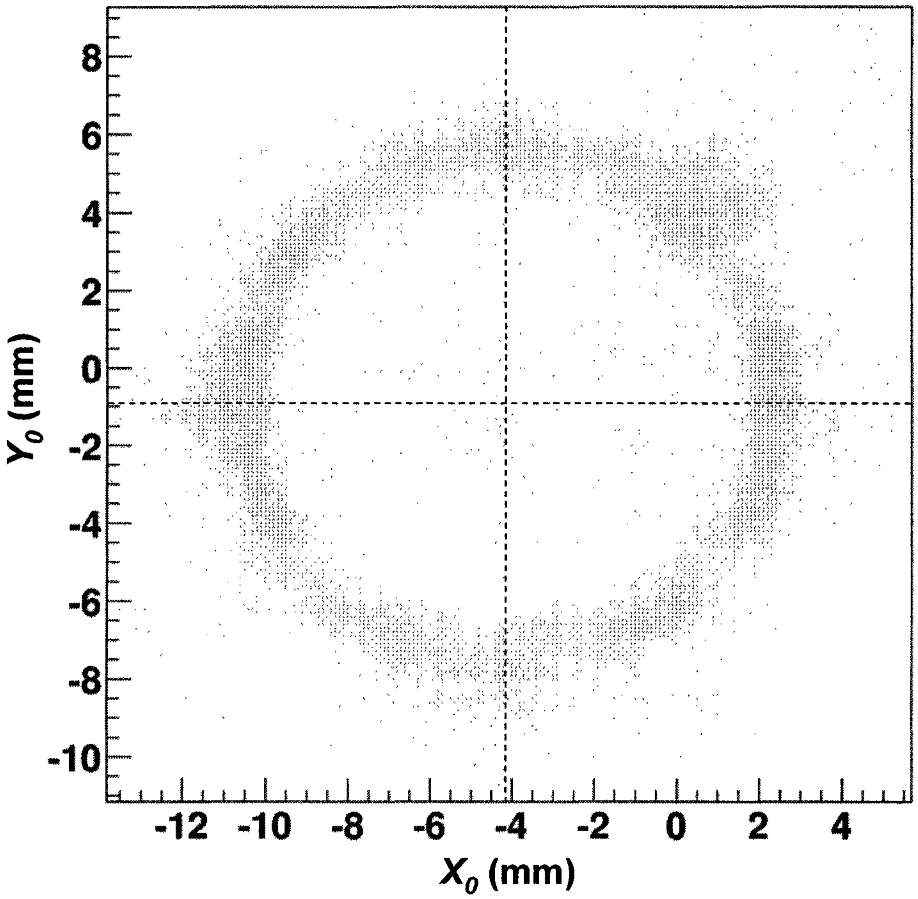

Fig. 3.7. This plot of Y_0 versus X_0 was used to transpose the center of the coordinate system for ^{28}Si at 375 MeV nucleon^{-1}.

CHAPTER IV: RESULTS AND DISCUSSION

Incident Ion Selection

An example of a distribution of total energy deposited in a PSD is found in Fig. 4.1. The height of the primary ion peak for the horizontal PSD of PSD pair 3 for ^{28}Si at 375 MeV nucleon^{-1} was 1.29×10^5 events. Five percent of maximum was 6450, so that the full width at five percent of maximum was between 105 MeV and 117 MeV. Incident ions of interest were identified in each horizontal and vertical PSD and the trigger silicon detector as events that populated the prevalent peak in the energy deposited distribution of each detector. Other events not in this primary ion peak were eliminated from the data.

Noise and Background

Because the stem of the TEPC used in this study is long (Fig. 4.2), a long anode wire extended from the TEPC active volume to its base. This long anode wire acted as an antenna for electronic noise. As a result, a moderate amount of noise distorted the TEPC signal. Other than using a very short BNC cable to connect the energy signal from the base of the TEPC to the preamplifier of the TEPC, no attempt was made to actively suppress electronic noise in the TEPC and its amplifiers.

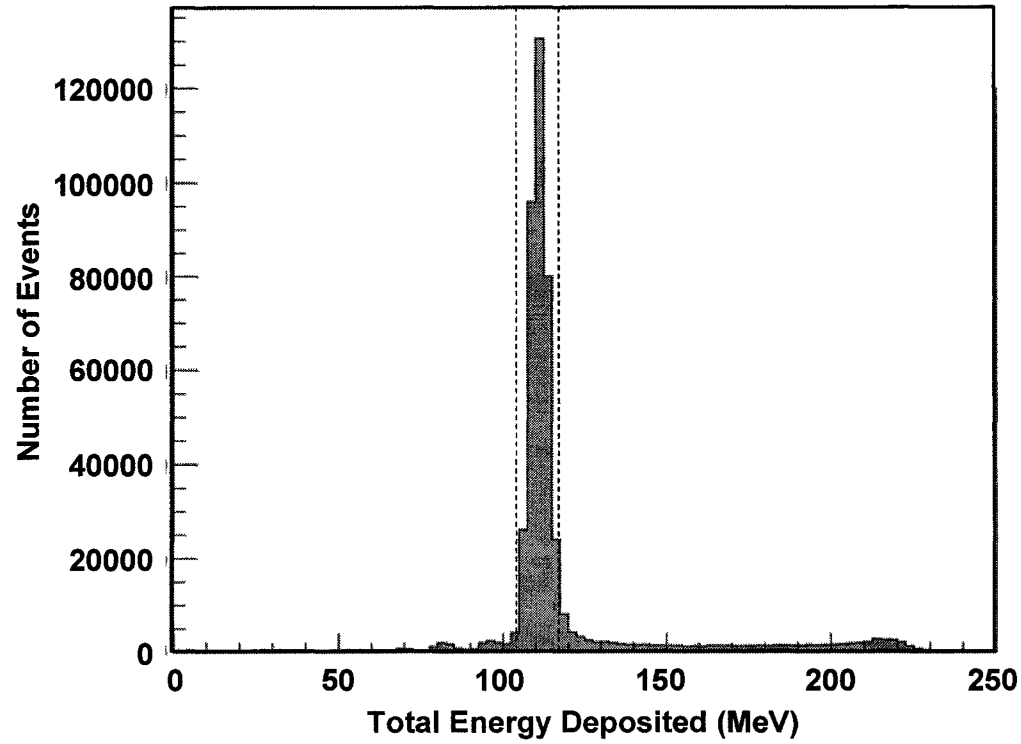

Fig. 4.1. Total energy deposited in the *X* detector of PSD pair 3 for the ^{28}Si at 375 MeV nucleon^{-1} experiment. The prominent peak is populated by events of incident ^{28}Si ions. Events with energy deposition between the two dashed lines (from 105 MeV to 117 MeV) were identified as incident ion events.

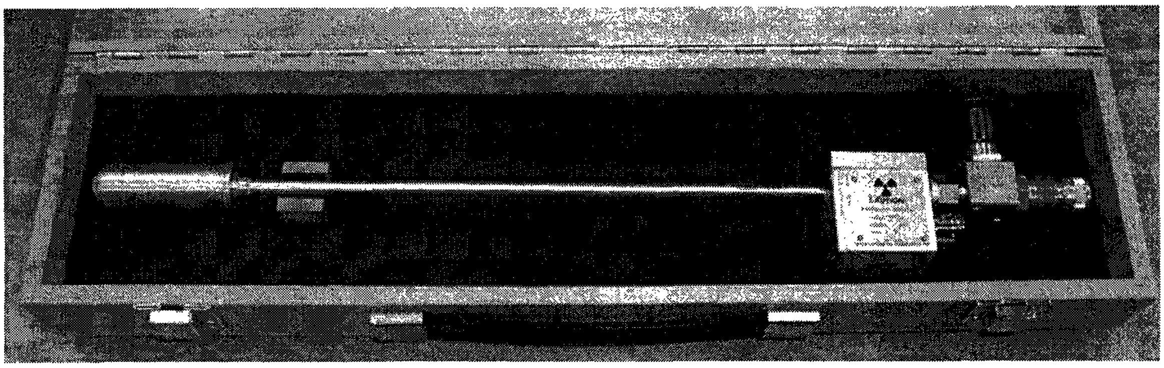

Fig. 4.2. Photograph of the Far-West Technology half-inch Rossi-type TEPC (serial number 1376) used in all of the experiments.

As stated in Chapter III: Materials and Methods, two trigger signals were used with the data acquisition system—one from the trigger silicon detector and one from the TEPC. Triggering was done both with and without the trigger silicon detector and the TEPC in coincidence for all ions with the exception of ^{16}O at 385 MeV nucleon^{-1}. To increase the efficiency of data acquisition for ^{16}O at 385 MeV nucleon^{-1} ($\beta = 0.71$, $LET =$ 19.9 keV μm^{-1}), because large-ε events in the TEPC were of greatest scientific concern when the data was recorded, no data was processed without the TEPC included in the triggering. As a result, the response function of the TEPC for ^{16}O was inadequately measured at small ε. To compensate for this the small-ε portion of the response function of the TEPC for ^{12}C at 389 MeV nucleon^{-1} ($\beta = 0.71$, $LET = 11.2$ keV μm^{-1}) was adjusted for the difference in *LET* and applied to the response function for ^{16}O.

During each experiment, the data acquisition system was also triggered by a pulse generator running at a fixed rate of either 1 or 10 Hz. These events were identified in off-line analysis as having a noise signal from the TEPC but with a signal from the trigger silicon detector that was below the lower threshold of its discriminator. For example, for ^{4}He at 225 MeV nucleon^{-1} (Fig. 4.3), the trigger was set to record only events where the pulse height signal from the trigger silicon detector was greater than approximately channel 700 (one-third of the channel number of the peak). Therefore, for ^{4}He at 225 MeV nucleon^{-1}, when the pulse height was less than channel 500 and the total energy deposited signals in PSD1-3 were near zero, the data acquisition system recorded events that were triggered by the pulse generator. The energy deposited distribution of the TEPC corresponding to these events constituted background and noise.

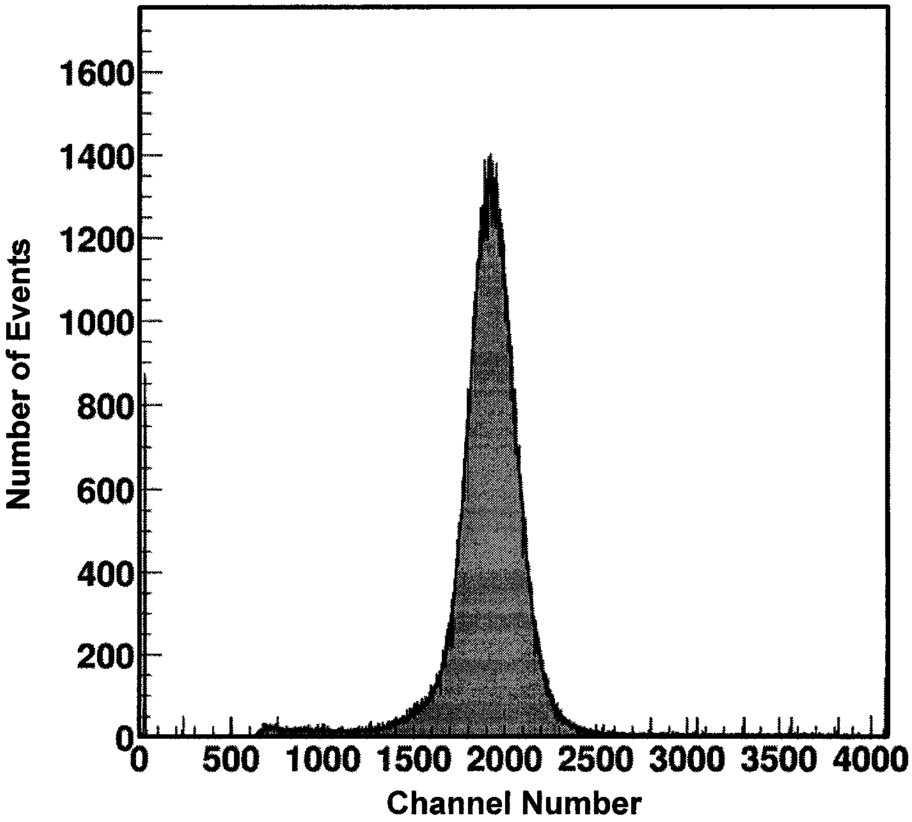

Fig. 4.3. Pulse height spectrum of the trigger silicon detector for all events for ^{4}He at 225 MeV nucleon^{-1}. The trigger was set to record events with pulse heights that were only greater than approximately channel 700.

Based on these background and noise signals, a lower threshold was determined for each experiment such that the signals corresponding to energy depositions below this value could not be distinguished from noise. The value of this lower threshold, ε_{min}, for each ion is listed in Table 4.1. An example of a plot that was used to determine ε_{min} is

TABLE 4.1

Results of experiments for each particle beam from previous HZE studies (Rademacher, 1997; Rademacher *et. al*, 1998; Gersey *et. al*, 2002; Guetersloh, 2003; Guetersloh *et. al*, 2004) and the current HZE study using an identical spherical TEPC. Also listed are the properties of the particle beams from all of the experiments from Table 1.3.

Ion	***Energy***[a]	β	***d***[b]	ε_{min}[c]	***LET***	$\bar{y}_f$	$\bar{y}_D$
	(MeV n^{-1})		**(μm)**	**(keV)**	**(keV μm^{-1})**		
			Previous Studies				
^{14}N	79	0.39	1	3	43.1	43.7	46.8
^{16}O	119	0.46	1	3	40.9	39.1	43.9
^{20}Ne	211	0.58	1	3	43.8	42.4	47.6
^{28}Si	781	0.84	1	3	46.4	39.4	46.7
^{56}Fe	200	0.57	1	0	302	199	328
^{56}Fe	360	0.69	1	0	214	146	216
^{56}Fe	540	0.77	1	0	179	134	173
^{56}Fe	700	0.82	1	0	163	125	159
^{56}Fe	790	0.84	1	0	157	118	153
^{56}Fe	1000	0.87	1	0	149	106	147
^{56}Fe	1050	0.88	1	0	149	79	143
			Current Study				
^{4}He	225	0.59	3	0.3	1.68	1.56	2.58
^{12}C	215	0.58	3	0.6	15.6	13.4	16.1
^{12}C	389	0.71	1	0.35	11.2	9.93	12.4
^{16}O	385	0.71	1	0.4	19.9	17.9	20.8
^{28}Si	375	0.70	1	0.02	61.9	50.4	59.8
^{56}Fe	355	0.69	1	3	219	184	224

[a] Energy at the active volume of the TEPC.

[b] *d* is the simulated tissue diameter of the TEPC.

[c] ε_{min} is the selected lower threshold for energy deposition below which events were considered indistinguishable from noise and were eliminated from the data.

found in Fig. 4.4. For ^{12}C at 389 MeV nucleon^{-1}, an ε_{min} of 0.35 keV was selected based on the location of the approximate maximum the noise and background signals. For each ion, particles that missed the detector entirely (i.e., $b > 8.9$ mm) provided signals in the TEPC that were essentially identical to noise and background signals (Fig. 4.5). Therefore, events that were below ε_{min} in the TEPC were eliminated from the data.

Energy Deposited Response Functions

The distribution of energy deposition events in the TEPC, or 'response function,' for a broad uniform beam of ^{12}C ions at 215 MeV nucleon^{-1} is shown in Fig. 4.6. The solid line in this plot shows the predicted distribution of energy depositions if $\varepsilon = LET \cdot x$, where x is the path length through the gas cavity. The shape of this response function is similar to those reported earlier (Rademacher, 1997; Rademacher *et al.*, 1998; Gersey *et al.*, 2002; Guetersloh, 2003; Guetersloh *et al.*, 2004; Borak *et al.*, 2004). Three significant differences were observed between the actual data and what would be the expected distribution based on *LET* and the path length distribution through the gas cavity. First, the broad peak, indicated as region A, was shifted to smaller energy deposition than what would be expected if $\varepsilon = LET \cdot x$. Also, there were a large number of small energy deposition events, or a 'leading edge,' in the spectrum (region B). Thirdly, a significant number of events were found that were much larger than the maximum energy deposition based on *LET* and maximum x of the incident ion (region C).

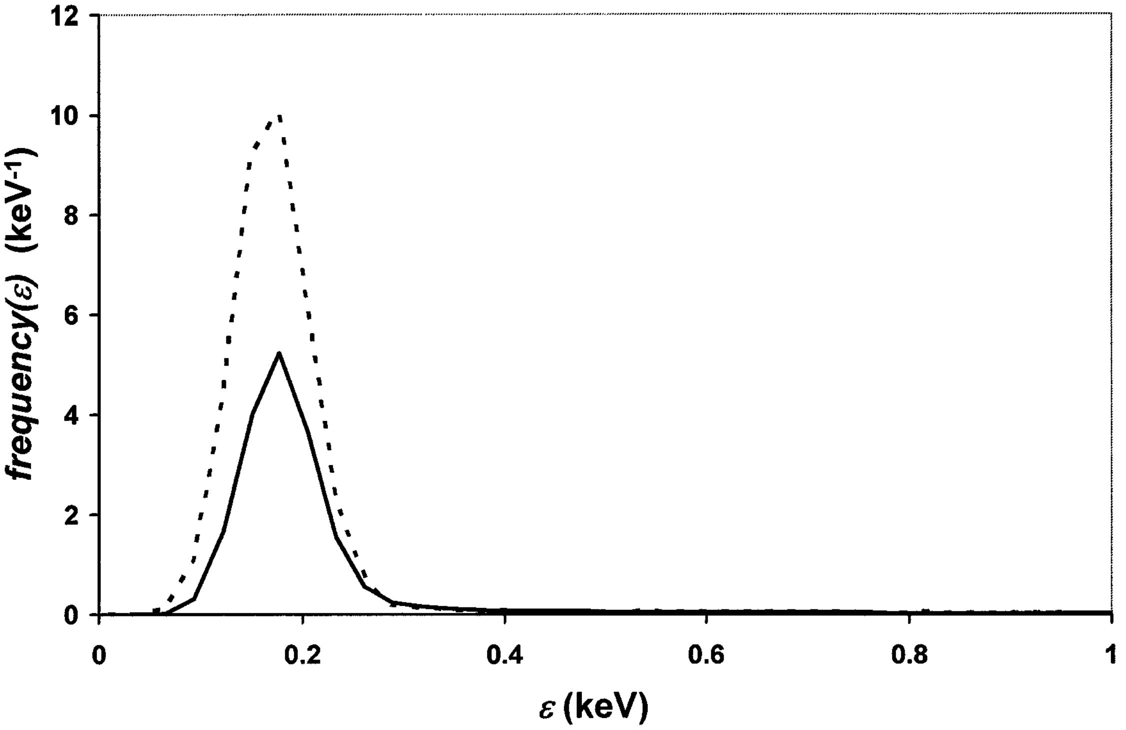

Fig. 4.4. Low energy deposition portion of the TEPC distributions of 389-MeV-nucleon^{-1} ^{12}C incident ion signals (solid line) and background and noise signals (dashed line). Only events where $\varepsilon < 1$ keV are shown. This plot was used to determine the noise and background lower threshold, ε_{min}, for the energy deposited distribution of the TEPC for ^{12}C at 389 MeV nucleon^{-1}.

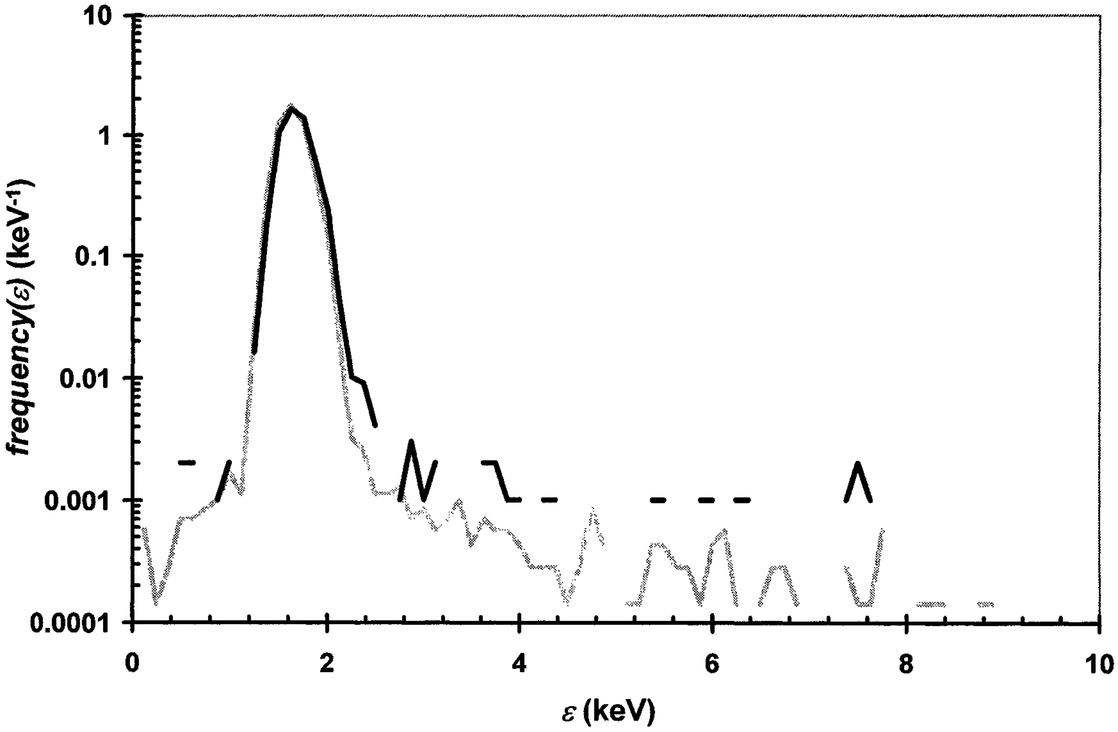

Fig. 4.5. Comparison between the ε-distributions for ^{28}Si at 375 MeV nucleon^{-1} data with b > 8.9 mm (black line) and the noise and background distribution (gray line) for the same experiment.

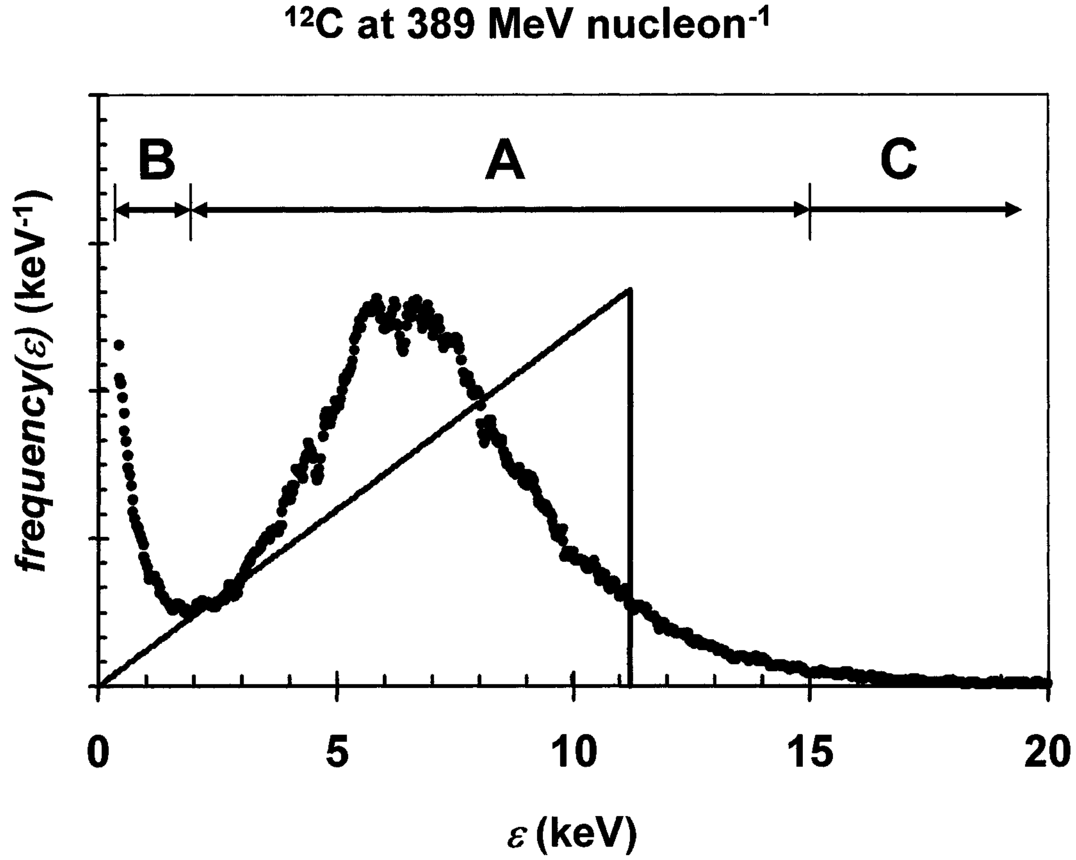

Fig. 4.6. The distribution of energy deposition for events measured in a spherical TEPC operating with a simulated diameter of 3 μm for ^{12}C ions at 389 MeV nucleon^{-1} (only $\varepsilon < 20$ keV is displayed). A solid black line represents the predicted distribution based on the first approximation for energy deposition, $\varepsilon = LET \cdot x$. Three regions, A, B, and C, represent events with different classes of trajectories through the detector.

The broad peak (region A) was populated by events in which the incident ion passed through the gas cavity of the TEPC. Fig. 4.7 shows the transverse position at the middle of the TEPC ($Z_0 = 0$) for events in this broad peak for ^{12}C at 389 MeV nucleon^{-1}. These events were within the inside wall of the active volume. A narrower selection of events that populated the highest portion (5.5 keV $< \varepsilon <$ 7.5 keV) of this broad peak (Fig. 4.8) shows that these events were passing through the center of the detector. Ions from region A lose some energy deposition when their delta-rays escape the active volume and deposit energy in the wall, and the ionization in the TEPC is reduced, causing a decrease in the energy deposited in the TEPC. For ions traveling through the gas cavity of the detector, some of this energy loss is compensated by the delta-ray influx from forward-moving delta-rays originating from interactions of the primary ion with the upstream half of the wall of the detector.

Region B, corresponding to small values of ε, was populated by events where the incident ions missed the gas cavity but passed through the side wall of the detector and produced delta-rays that entered the gas cavity. By selecting these small ε events their transverse position may be displayed at $Z_0 = 0$ (Fig. 4.9). The impact parameters of these events were between 6.35 mm and 8.9 mm, corresponding to the wall of the detector. Although the primary ion missed the active volume of the TEPC, delta-rays from interactions between the primary ion and the side wall of the detector traveled into and deposited energy in the gas.

Region C, corresponding to very large values of ε, was populated by events where the incident ions either grazed the inside wall of the gas cavity or happened to hit the

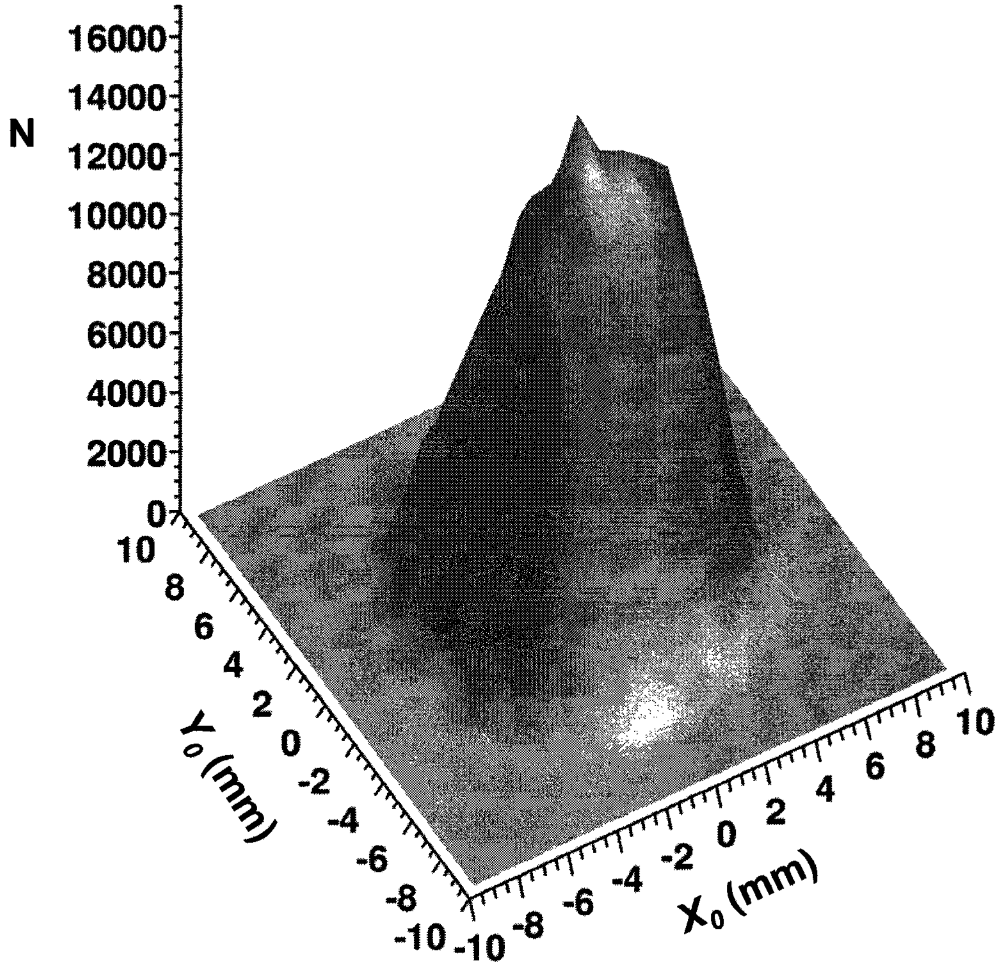

Fig. 4.7. Two-dimensional histogram of region A (see Fig. 4.6) events, 2 keV < ε < 15 keV, at $Z_0 = 0$ for ^{12}C at 389 MeV nucleon^{-1}. The vertical axis is the number of events per bin. It is clear from this plot that these were events in which the incident ion traveled through the gas cavity of the detector, i.e., b < 6.35 mm.

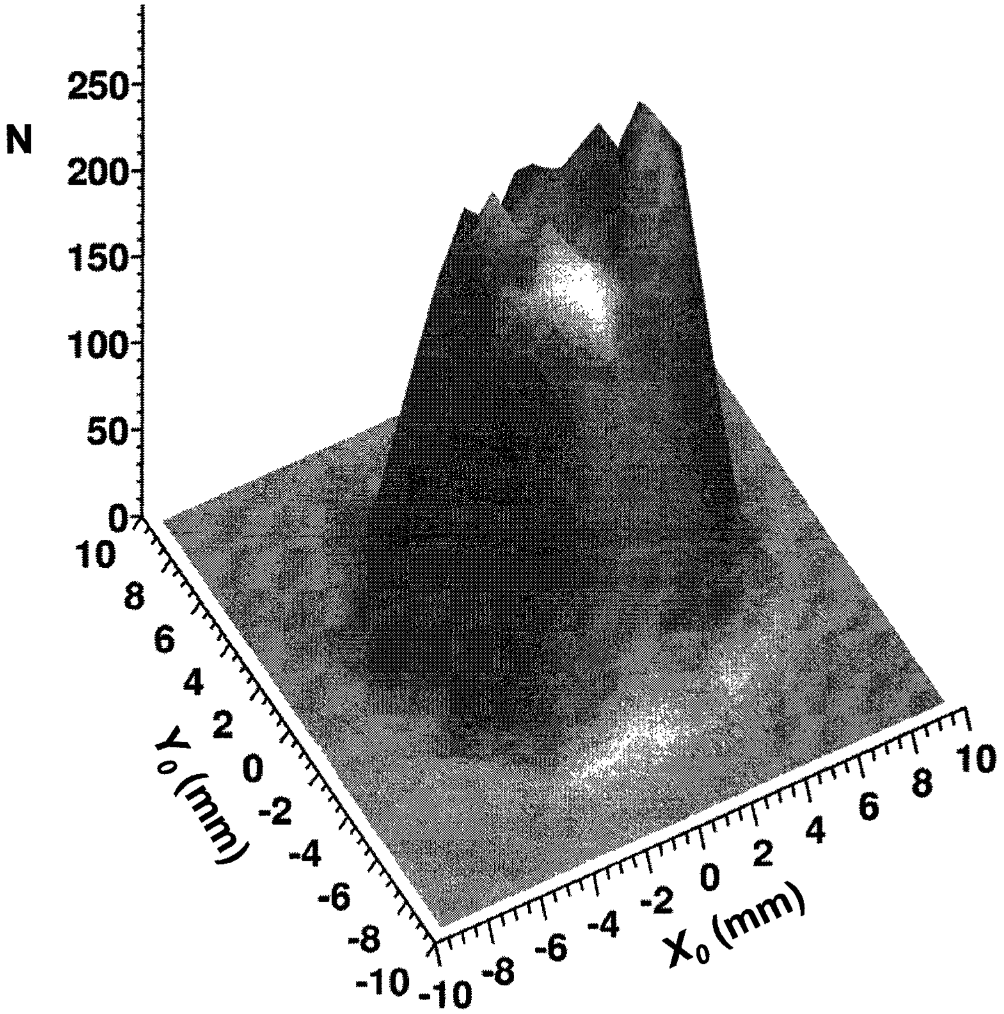

Fig. 4.8. Two-dimensional histogram of the highest portion of the peak of region A (see Fig. 4.6) events, 7.25 keV $< \varepsilon <$ 7.35 keV, at $Z_0 = 0$ for ^{12}C at 389 MeV nucleon^{-1}. The vertical axis is the number of events per bin. It is clear from this plot that these were events in which the incident ion traveled through the center of the gas cavity of the detector.

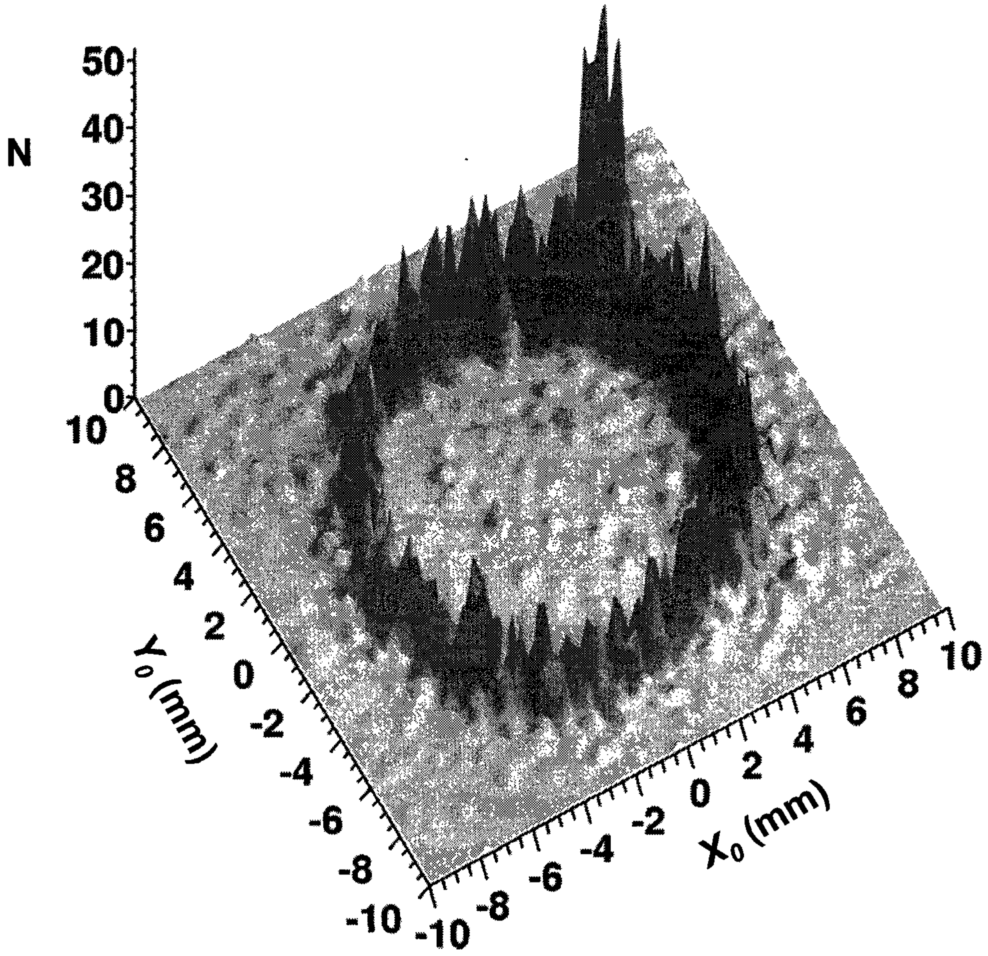

Fig. 4.9. Two-dimensional histogram of region B (see Fig. 4.6) events, 0.35 keV $< \varepsilon < 2$ keV, at $Z_0 = 0$ for ^{12}C at 389 MeV nucleon^{-1}. The vertical axis is the number of events per bin. It is clear from this plot that these were events in which the incident ion traveled outside of the gas but through the walls of the detector, i.e., 6.35 mm $< b < 8.90$ mm.

anode or helical grid wires within the cavity. Fig. 4.10 shows the transverse location of these ions as they passed through the middle of the TEPC. Because of the low number of events, it is difficult to see the wires in this plot. They extend along $Y_0 = 0$. Ions corresponding to these events, where the primary ion passed through the relatively high density wall or wires, produced a large number of delta-rays and deposited a large amount of energy in the gas.

The response functions of the TEPC, $f(\varepsilon)$, representing distributions of ε, are shown in Fig. 4.11 for all ions in this study. They have a similar shape. There is a leading edge of small energy deposition events corresponding to region B in Fig. 4.6. There is a broad peak corresponding to region A in Fig. 4.6 with events that had smaller energy deposition than expected based on *LET* and the path length distribution through the gas cavity. There is a significant number of events with energy depositions that were larger than the maximum based on the product of *LET* and the simulated diameter, *d*, as in region C of Fig. 4.6.

Relative Energy Deposition

Probability Density Functions

The coefficient of variation of the distribution of ε is defined as

$$CV_\varepsilon \equiv \frac{\sigma_\varepsilon}{\bar{\varepsilon}}, \tag{4.1}$$

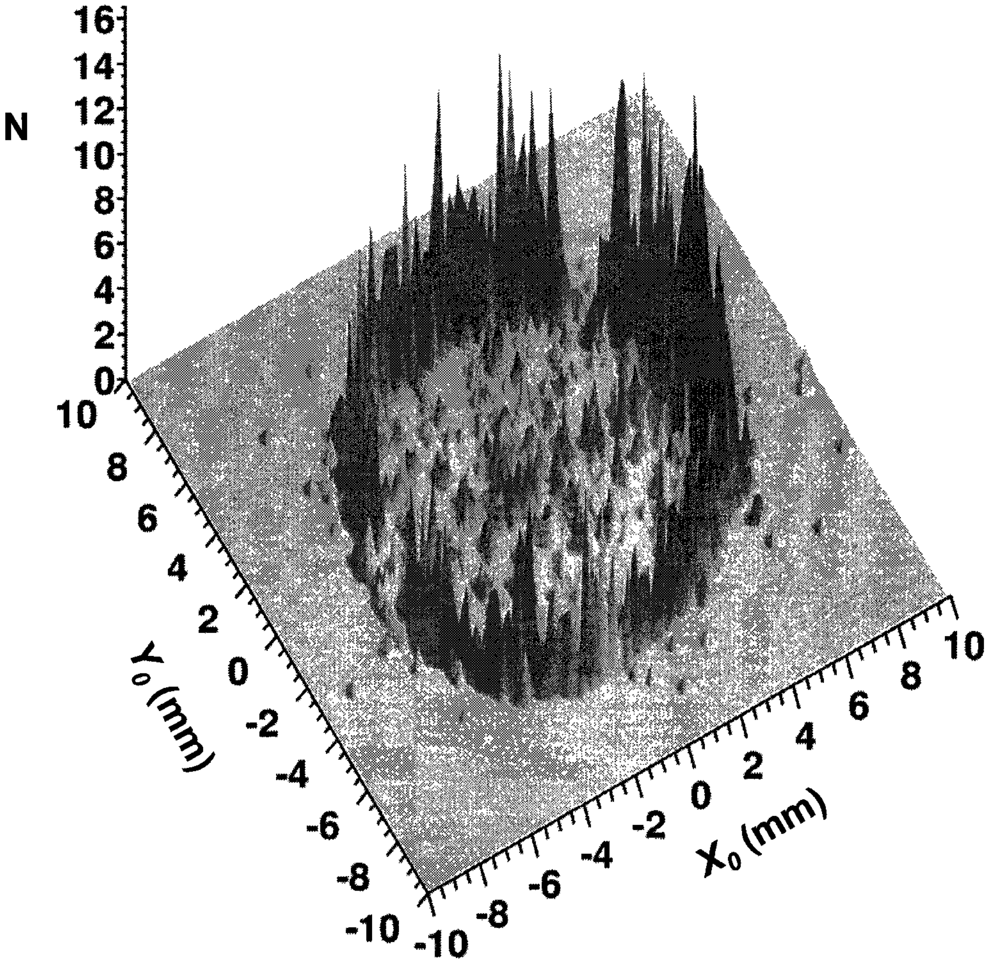

Fig. 4.10. Two-dimensional histogram of region C (see Fig. 4.6) events, 25 keV < ε, at $Z_0 = 0$ for ^{12}C at 389 MeV nucleon^{-1}. The vertical axis is the number of events per bin. These were events in which the incident ion either grazed the inside wall, i.e., $b = 6.35$ mm, or interacted with the anode or helical wire of the detector. The wires extended along $Y_0 = 0$.

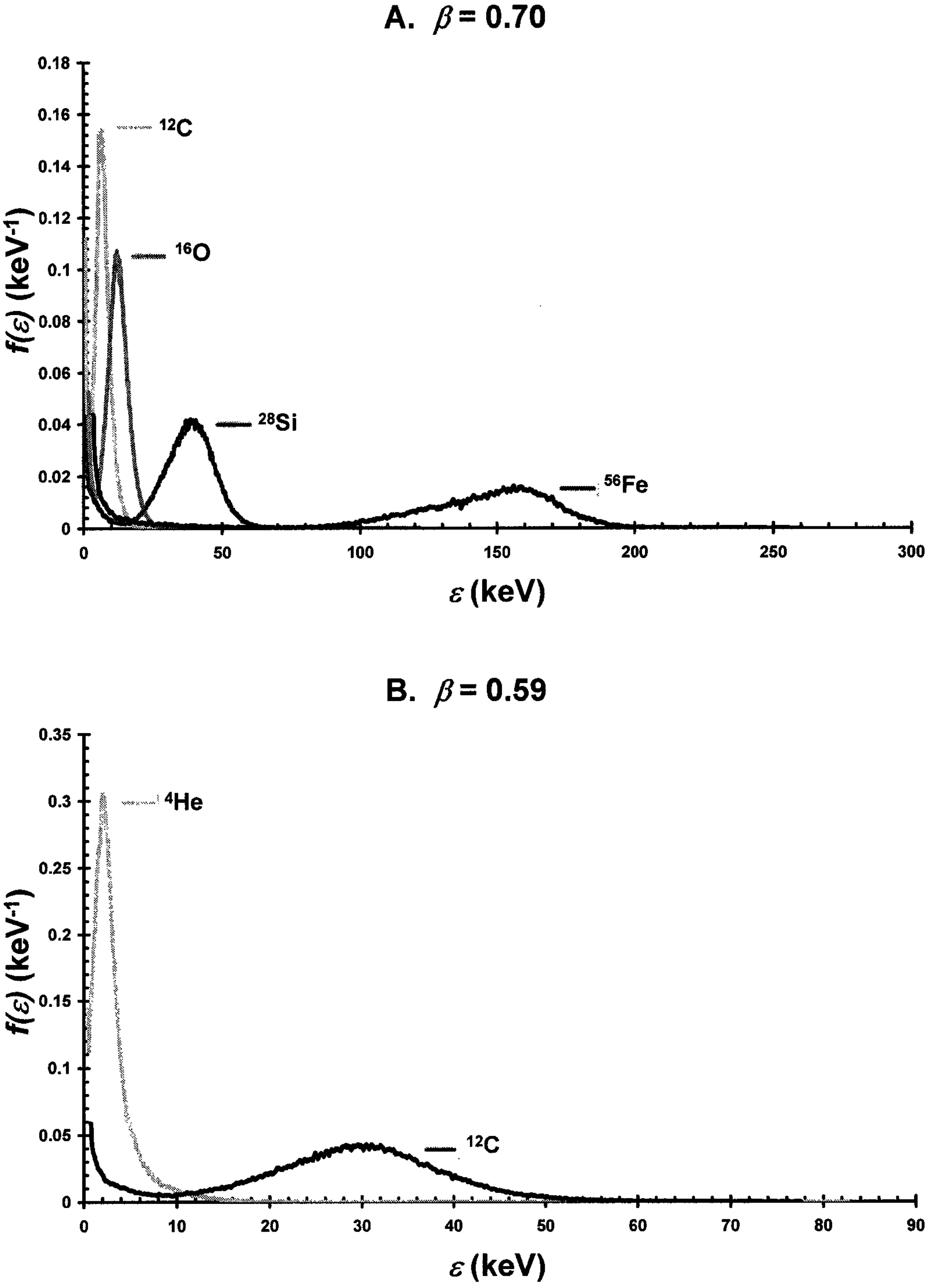

Fig. 4.11. Probability density functions, $f(\varepsilon)$, of energy deposition, or "response functions," of the TEPC, were smoothed (Savitzky and Golay, 1964). Response functions for ions of velocity $\beta = 0.70$ (A) and ions of velocity $\beta = 0.59$ (B).

where σ_ε is the standard deviation and $\bar{\varepsilon}$ is the mean of the distribution of ε. For comparison purposes, the distributions of ε can be adjusted by creating a new standardized random variable. In Fig. 4.12, the random variable, ε, has been adjusted by dividing by the maximum predicted energy deposition based on $LET \cdot d$ of each ion. Here, the relative energy deposition with respect to $LET \cdot d$ has been defined,

$$\eta \equiv \frac{\varepsilon}{LET \cdot d}, \tag{4.2}$$

along with its probability density function, $g(\eta)$. The coefficient of variation of η is numerically equivalent to the coefficient of variation of ε:

$$CV_\eta = \frac{\sigma_\eta}{\bar{\eta}} = \frac{\frac{1}{LET \cdot d}\sigma_\varepsilon}{\frac{1}{LET \cdot d}\bar{\varepsilon}} = \frac{\sigma_\varepsilon}{\bar{\varepsilon}} = CV_\varepsilon, \tag{4.3}$$

where σ_η is the standard deviation and $\bar{\eta}$ is the mean of the distribution of η. The coefficient of variation is a measure of the relative spread in the broad peaks of each distribution with respect to its mean. Therefore, the relative spreads in the broad peaks of the distributions of η may be used to qualitatively compare the spreads in the broad peaks of the distributions of ε for each ion.

For ions of the same velocity, as Z decreased, three effects were observed in the broad peaks of the distributions of η. First, the spread of the broad peaks of the

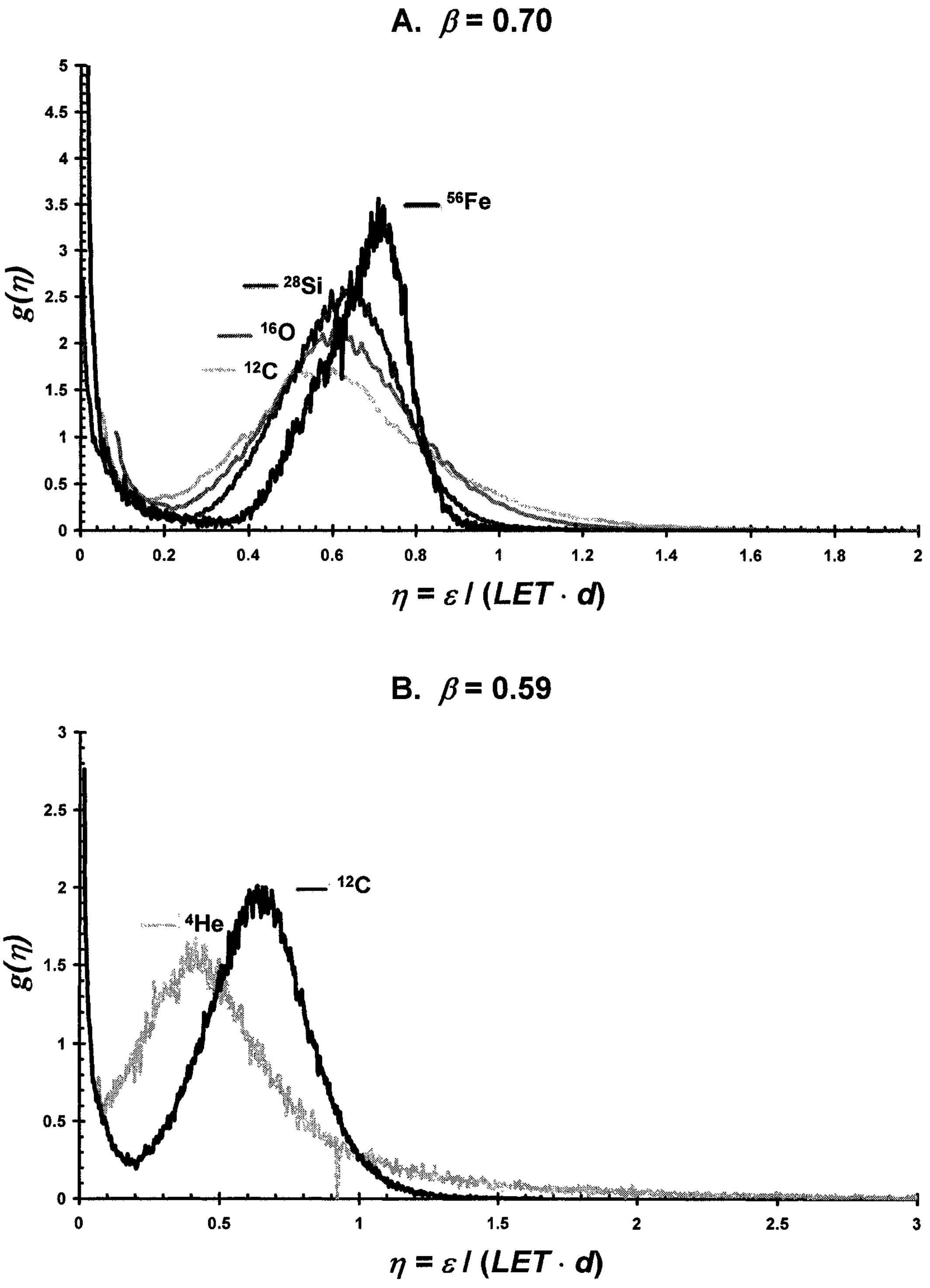

Fig. 4.12. Probability density functions, $g(\eta)$, of the relative energy deposition with respect to $LET \cdot d$ were smoothed (Savitzky and Golay, 1964). Distributions for ions of velocity $\beta = 0.70$ (A) and ions of velocity $\beta = 0.59$ (B).

distributions increased. This effect was due to the changing effects of energy straggling and ion-pair production with decreasing atomic number. Holding velocity constant, as atomic number decreases, *LET* decreases. As a result, ion-pair production in the gas cavity decreases, which causes the signal and, hence, the resolution of the signal sent by the TEPC to be reduced. Also, energy straggling increases, which has the effect of reducing the resolution of the energy signal from the TEPC (Knoll, 2000). Second, for events where $\eta > 0.2$, the means of the distributions, $\bar{\eta}_{0.2}$, remained constant (see Table 4.2). The averages of the values of $\bar{\eta}_{0.2}$ were 0.64 ± 0.02 for the $\beta = 0.70$ ions and 0.66 ± 0.03 for the $\beta = 0.59$ ions. The means of the broad peaks of the distributions were the same because ions of the same velocity eject atomic electrons in a particular target with the same distribution of energy (Kraft *et al.*, 1992; Craven and Rycroft, 1996). Therefore, tracks of the delta-rays emitted along the path of the incident ion through the detector had the same range and energy deposition patterns independent of the charge of the incident ion. Finally, a greater number of events were measured where ε was greater

TABLE 4.2

Properties of the distributions of η, where $\eta > 0.2$.

Ion	***Z***	β	***LET*** **(keV µm^{-1})**	$\bar{\eta}_{0.2}$	**median($\eta_{0.2}$)**	**mode($\eta_{0.2}$)**
^{4}He	2	0.59	1.68	0.68	0.53	0.41
^{12}C	6	0.58	15.6	0.64	0.64	0.63
^{12}C	6	0.71	11.2	0.65	0.61	0.60
^{16}O	8	0.71	19.9	0.64	0.62	0.60
^{28}Si	14	0.70	61.9	0.62	0.62	0.62
^{56}Fe	26	0.69	219	0.66	0.68	0.71

than the maximum based on $LET \cdot d$ (i.e., $\eta > 1$). This effect is also because of the spreading of the broad peak, both to smaller and larger η, with decreasing atomic number. In addition, the median and mode of the distribution of η decreased slightly with decreasing Z, indicating that the spreading of the data is somewhat skewed toward larger η and ε.

For ions of the same velocity, after transforming to the random variable, η, the regions of small energy deposition of the distributions (region B in Fig. 4.6) were nearly identical. These events corresponded to incident ions that did not pass through the gas cavity of the detector but instead traveled through the wall of the detector. The regions of small energy deposition of the distributions of η were the same because, again, ions of the same velocity eject atomic electrons in a particular target with the same distribution of energy. Therefore, tracks of the delta-rays ejected from the wall had the same range and energy deposition patterns independent of the charge of the incident ion.

Cumulative Distribution Functions

Energy deposited frequency distributions may be used to determine absorbed dose distributions by multiplying the frequency in each bin by the respective ε of the bin. Cumulative distribution functions (CDF) for the dose distributions of energy deposited for each ion are shown in Fig. 4.13. Again, a random variable, η, has been defined (Equation 4.2) by dividing ε by $LET \cdot d$ for each incident ion. For $\beta = 0.70$ ions, events with ε up to 30% of $LET \cdot d$ have approximately the same impact on absorbed dose. This is true up to about 20% of $LET \cdot d$ for $\beta = 0.59$ ions. As charge increased, holding β constant, ε events corresponding to the broad peak as in Fig. 4.6 (region A) had a greater

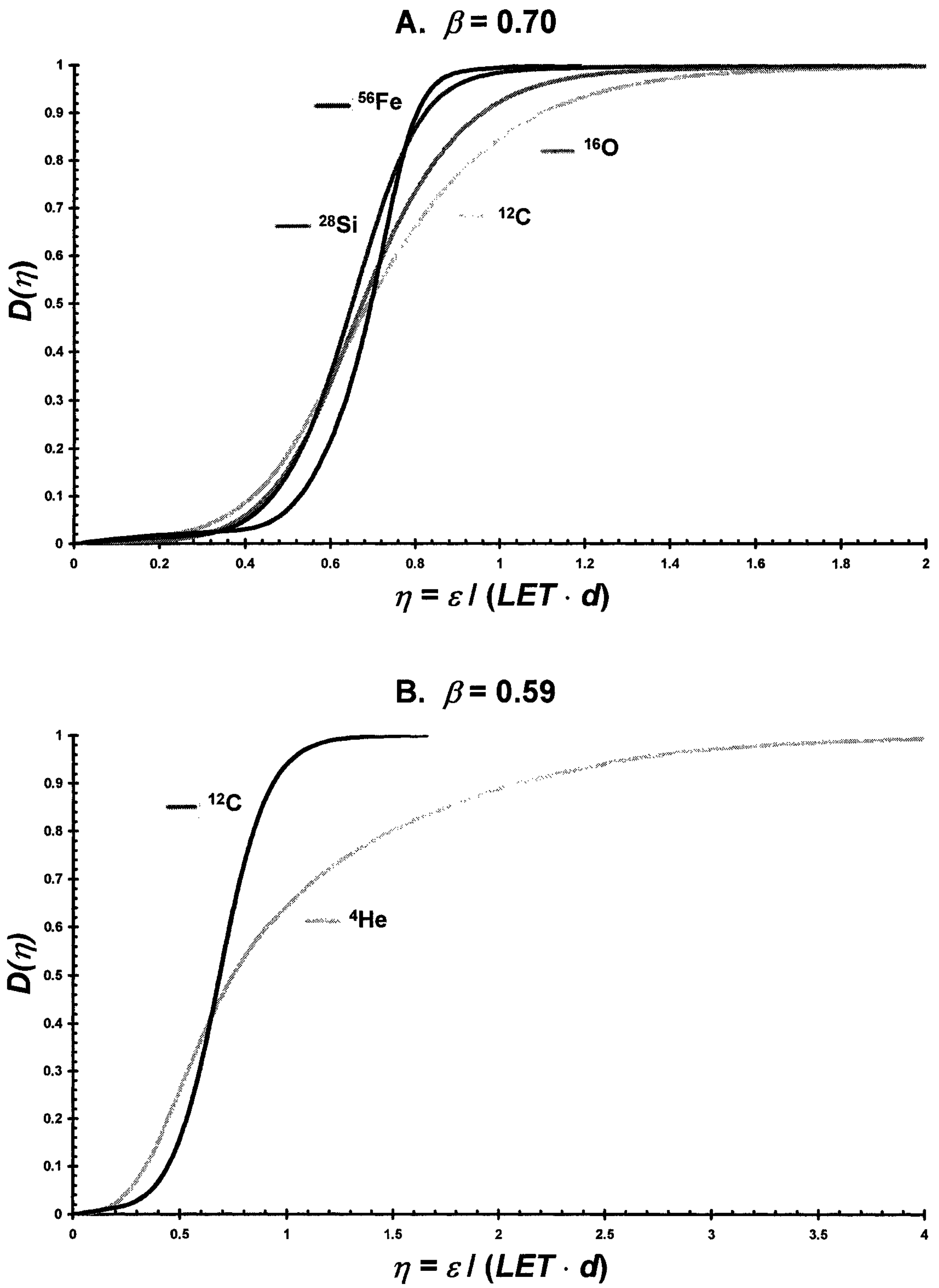

Fig. 4.13. Cumulative distribution functions of the dose distributions for $\beta = 0.70$ ions (A) and $\beta = 0.59$ ions (B). The random variable, η, has been defined (Equation 4.2) by dividing ε by $LET \cdot d$ for each incident ion.

impact on dose, and as charge decreased, large-ε events had more of an impact on dose. For lower-Z (and lower-*LET*) ions, a considerable contribution to dose was from events where ε was greater than $LET \cdot d$. For example, for ^{4}He, 35% of the dose was from events where ε was greater than $LET \cdot d$.

Complimentary Cumulative Distribution Functions

The response functions of the TEPC for ^{12}C and ^{56}Fe ions with velocity, $\beta = 0.70$, are compared in Fig. 4.14. In this plot, the random variable, η, has again been defined (Equation 4.2) by dividing ε by $LET \cdot d$ ($d = 1$ μm) for each incident ion and presented as complimentary cumulative distribution functions (CCDF). The data indicate that at high *LET* (^{56}Fe) there is a larger number of small energy deposition events that are distinguishable from noise. The energy interval between $0.1 \cdot LET \cdot d$ and $1.0 \cdot LET \cdot d$ represents the region where ions are passing through the gas cavity of the TEPC, i.e., broad peak events. Again, the spread in the data in this region are a convolution of variations in energy loss and detector resolution due to ion pair multiplication.

Spatial Resolution

The grazing ions that produce large energy depositions must have an impact parameter very close to the radius of the gas cavity. Otherwise, the soft delta-rays contributing to the large energy deposition would be stopped in the wall before reaching the gas cavity. A track model for the radial extension of an ion in water indicated that the dose from delta-rays is reduced by a factor of 10^4 at a distance of 10 nm from the trajectory of an ion at 400 MeV nucleon^{-1} and by a factor of 1.3×10^4 for ions at 240 MeV nucleon^{-1} (Cucinotta, 1995). This provides a narrow limit on the location of the

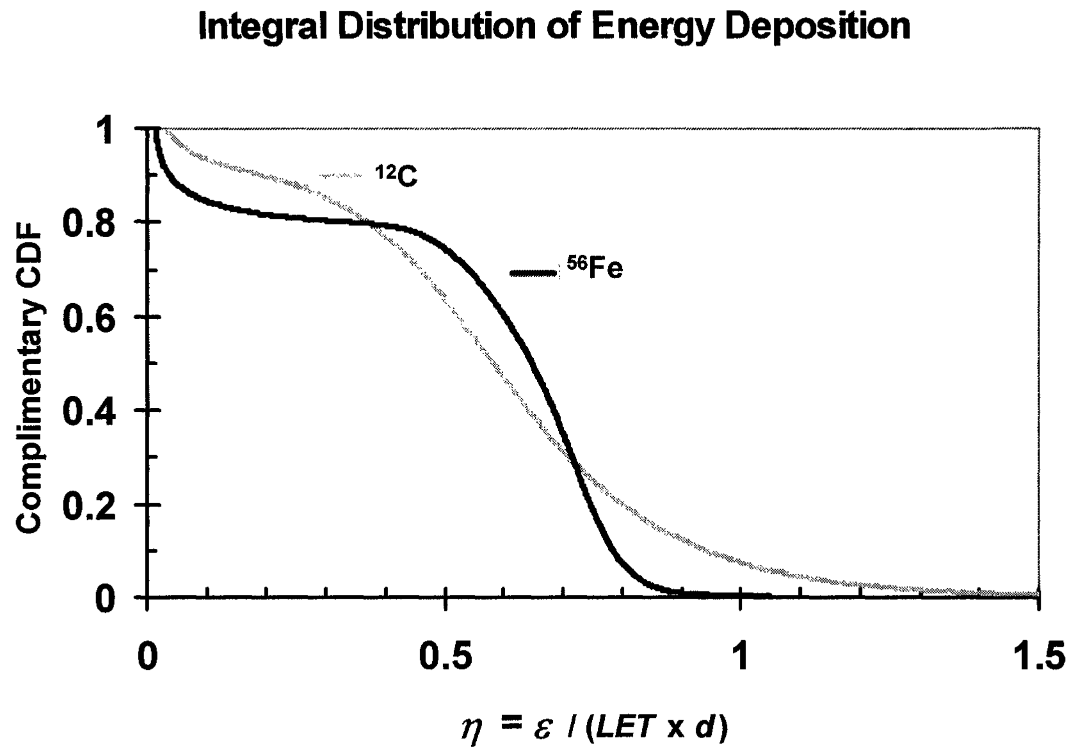

Fig. 4.14. The complimentary cumulative distribution for the probability density function, *g(η)*, measured by the TEPC for ^{12}C and ^{56}Fe at 376 MeV nucleon^{-1}. The random variable, η, has been defined (Equation 4.2) by dividing ε by $LET \cdot d$ ($d = 1$ μm) for each incident ion. The ordinate is the probability that events will have energy deposition greater the corresponding value of η on the abscissa.

track for grazing events, i.e., region C in Fig. 4.6. Fig. 4.15 shows an example of the distribution of impact parameters in region C for ^{56}Fe at 355 MeV nucleon^{-1}. The broad plateau occurring for impact parameter less than 5.5 mm is due to wire hits, and the peak centered near 6.26 mm is due to grazing events. Events in this peak can be used to determine the spatial resolution of track reconstruction assuming that these events occur exactly at the radius of the gas cavity. Fig. 4.16 shows the full width at half maximum (FWHM = 2.35σ) divided by the mean value in the peak for these events as a function of *LET* for all of the incident ions in this study. For ions with *LET* greater than 10 keV μm^{-1} (i.e., $Z \geq 6$), the resolution using this figure-of-merit is around 10%. There is a large increase in the FWHM for the ^{4}He ions due to the limitations of the charge separation technique used with the silicon PSDs. For this reason, position related analyses were not performed with the ^{4}He data.

A plot of Y_0 versus X_0 of small-ε events for ^{56}Fe at 355 MeV nucleon^{-1} (Fig. 4.17) illustrated the merit of the technique of determining the transverse position of the incident ion at $Z_0 = 0$. This plot may be compared to an x-ray radiograph of the detector (Fig. 4.18) as a qualitative demonstration of the spatial resolution of the positional spectrometer. In both figures, the gas fill hole in the upper-left corner of the wall of the TEPC can be seen, however it is difficult to see the alpha particle collimator in the lower-right corner. The events that are directly to the right of the active volume and vertically in the center represent events where the incident ion traveled near or through the extension of the anode wire of the detector. Outside of the wall, to the lower-right of Fig. 4.17 are the locations of events that interacted with the alpha source. The delta-rays of

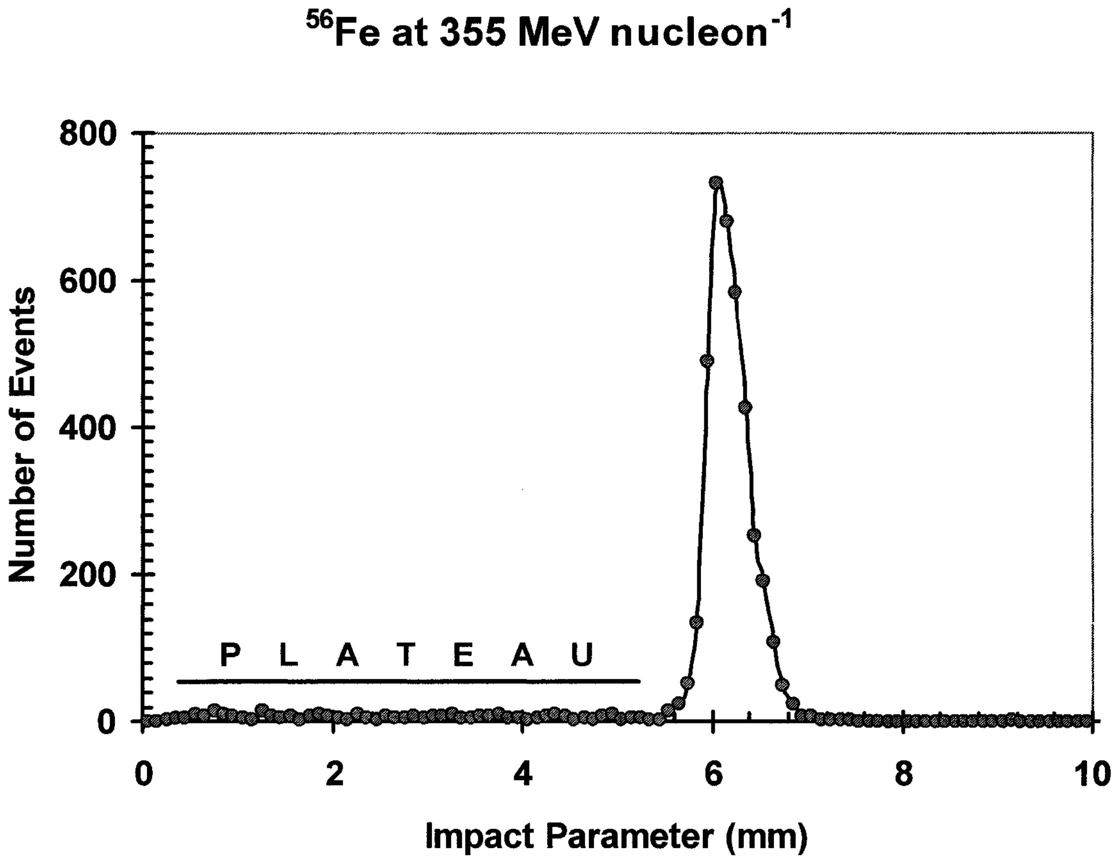

Fig. 4.15. The distribution of impact parameters for ^{56}Fe at 355 MeV nucleon^{-1} events with large energy deposition ($\varepsilon > 270$ keV) corresponding to region C (see Fig. 4.6). The broad plateau occurring for impact parameter less than 5.5 mm is due to wire hits.

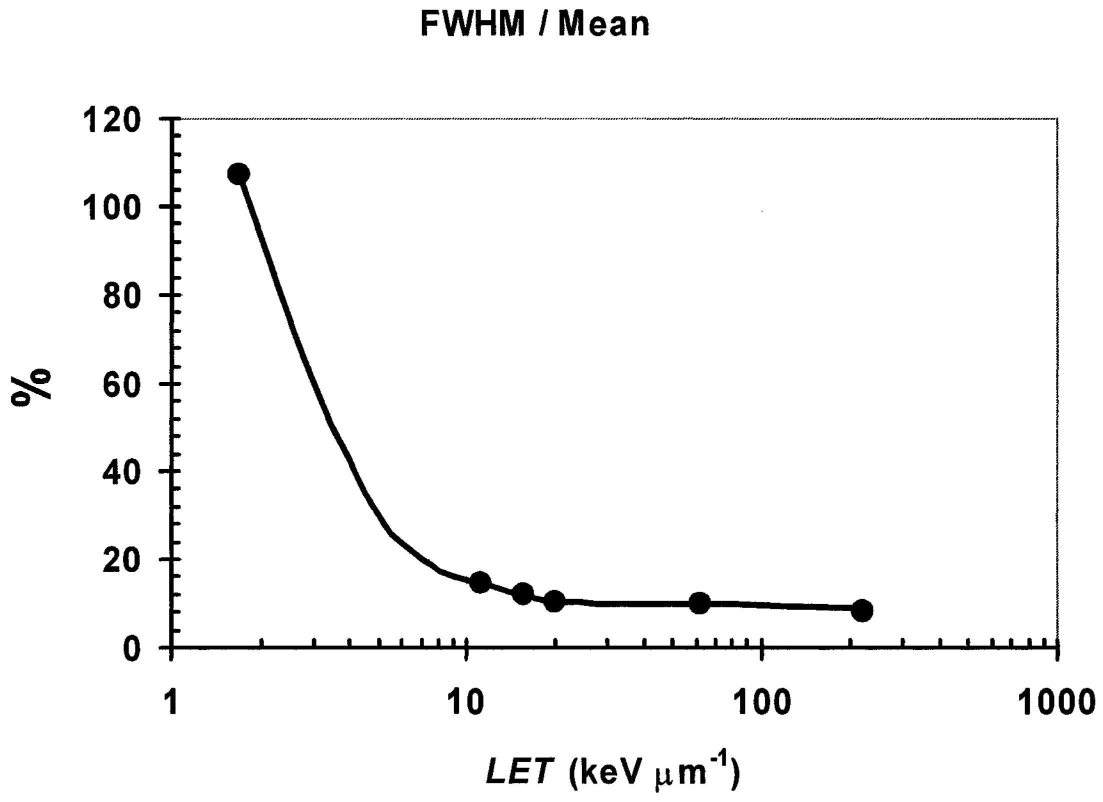

Fig. 4.16. The spatial resolution of the position-sensitive detectors for different ions as a function of *LET* using the width of the distribution of impact parameters for events with large energy deposition corresponding to region C (see Fig. 4.6). A solid line was added to guide the eye.

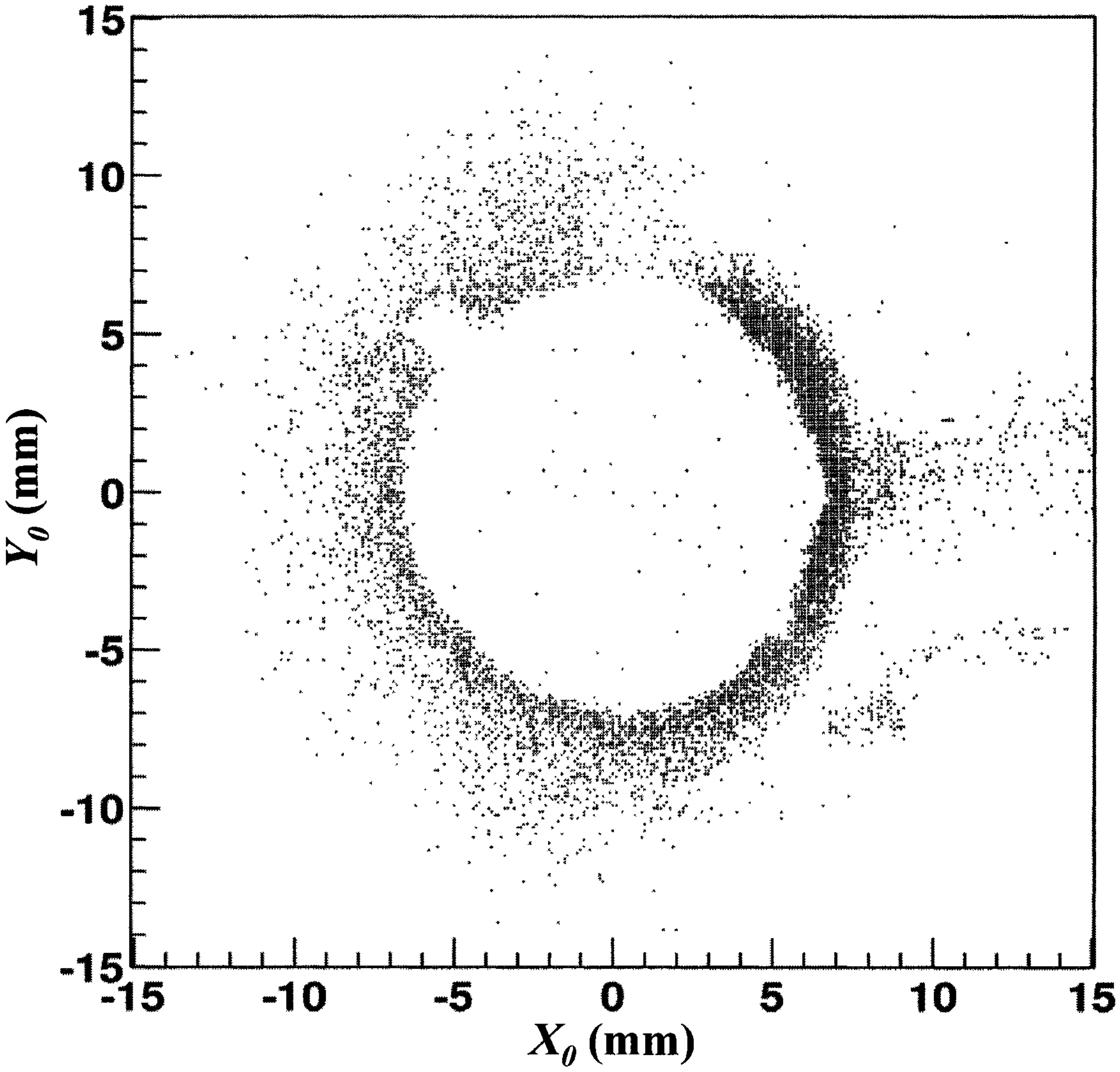

Fig. 4.17. Location, (X_0, Y_0), of incident $\beta = 0.70$ ^{56}Fe ions, where 2 keV < ε < 15 keV.

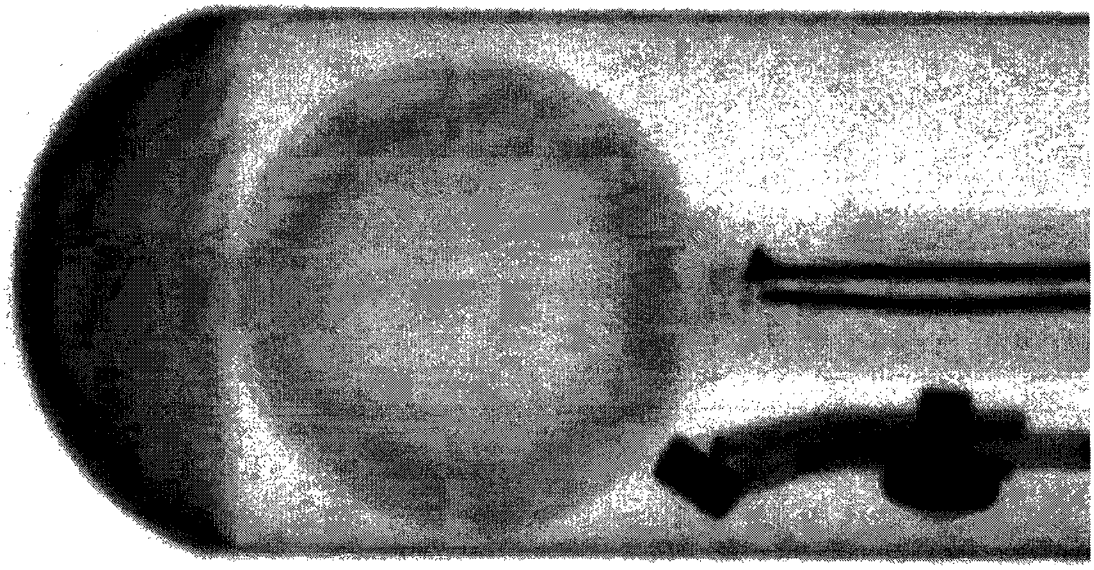

Fig. 4.18. Negative image of an x-ray radiograph of the half-inch (12.7 mm) Rossi TEPC used in this study. The gas chamber is surrounded by a 2.54-mm A-150 TE plastic wall with two holes—one is a gas-fill hole in the upper-left corner, and the other is an alpha particle collimator in the lower-right corner. Directly outside of the latter is a ^{244}Cm alpha source with a gravity-controlled shutter. Crossing the horizontal diameter are the anode and helical grid wires. To the right of the active volume extends the stem. The darkness to the left of the active volume is due to the curvature in the aluminum shell.

these events had enough energy to reach the active volume of the detector by traveling through the alpha particle collimator in the wall.

Events with b < 0.8 mm

Ions with impact parameters less than 0.8 mm passed near the center of the detector ($b \approx 0$). These ions had a minimum path length through the gas cavity at $b = 0.8$ mm,

$$x_{max} = 2\sqrt{r^2 - b^2} = 2\sqrt{(6.35\,\mathrm{mm})^2 - (0.8\,\mathrm{mm})^2} = 12.6\,\mathrm{mm}, \tag{4.4}$$

which is within 1% of the diameter of the gas cavity. Fig. 4.19 shows the mean value of energy deposition for these events with the values of the ordinate divided by $LET \cdot d$ for each incident ion. The standard error of the mean is smaller than the size of the symbols because of the large number of events used to compute the mean. The error bars represent the standard deviation of the sample of events. It can be seen that the mean energy deposited for these events was always less than 80% of the value that would be expected if $\varepsilon = LET \cdot d$. There does not appear to be any trend in these data if the results are plotted as a function of Z, β, β^2 or LET. This 20% reduction in mean energy deposited compared to the predicted maximum energy deposition is due to a combination of energy loss by delta-rays that escape the active volume of the detector and an energy gain from forward-moving electrons produced in the front wall of the detector (Rademacher, 1997; Rademacher *et al.*, 1998; Gersey *et al.*, 2002; Guetersloh, 2003; Guetersloh *et al.*, 2004).

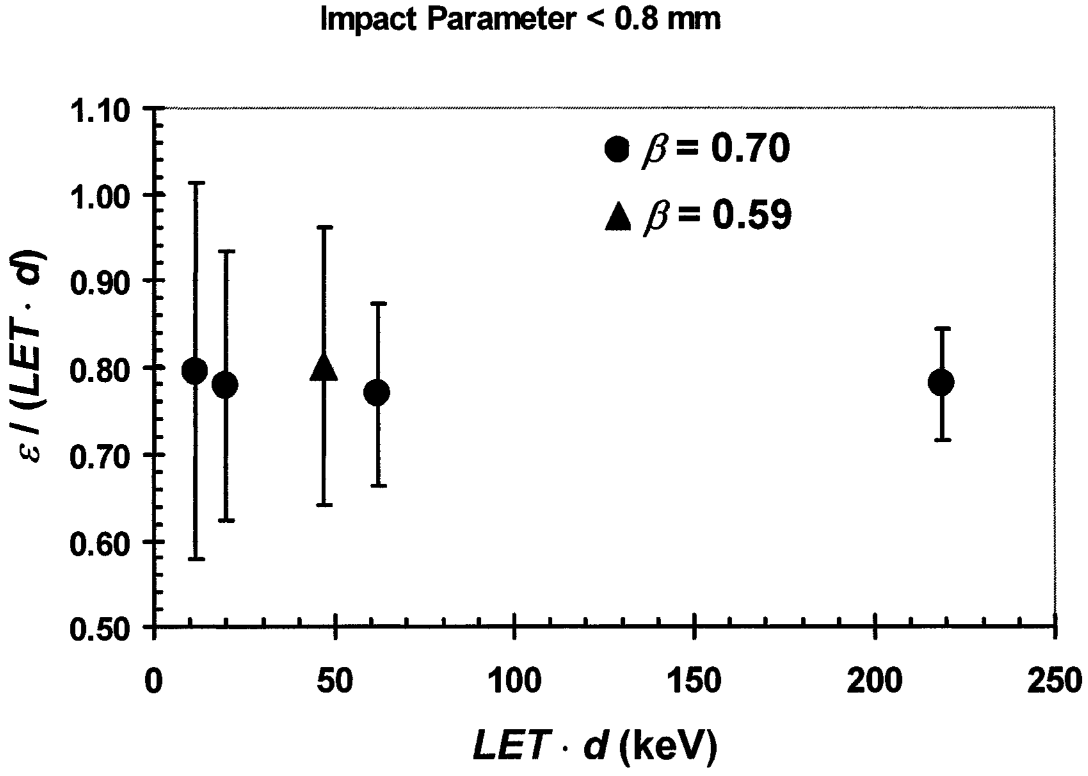

Fig. 4.19. The mean energy deposition in the TEPC for events where the incident ion passed through the center of the detector ($b < 0.8$ mm). The ordinate values of the data have been divided by the expected value of energy deposition based on the product of *LET* and the simulated diameter of each ion.

Lineal Energy

Distributions

The distributions of energy deposition for all ions were converted into distributions of lineal energy, y, and renormalized and are shown in Fig. 4.20. In order to see the full range of events recorded by the TEPC for ions of a wide range of *LET*, a logarithmic-linear plot of $y \cdot f(y)$ vs. y was created (Fig. 4.21).

Mean Values

Expected values, or means, of the y probability density functions, $f(y)$, were computed. The frequency averaged lineal energy, $\overline{y}_f$, was defined in Equation 1.6 as the first moment of y,

$$\overline{y}_f = \int yf(y)dy\,.$$

The predicted distribution for a spherical TEPC based on *LET* and the path length distribution of the ion is

$$f_{predicted}(y) = \frac{8}{9 \cdot LET^2}y\,,\ 0 < y \leq \frac{3}{2}LET\,. \tag{4.5}$$

Therefore, the predicted $\overline{y}_f$ for a spherical TEPC based on $f_{predicted}(y)$ is

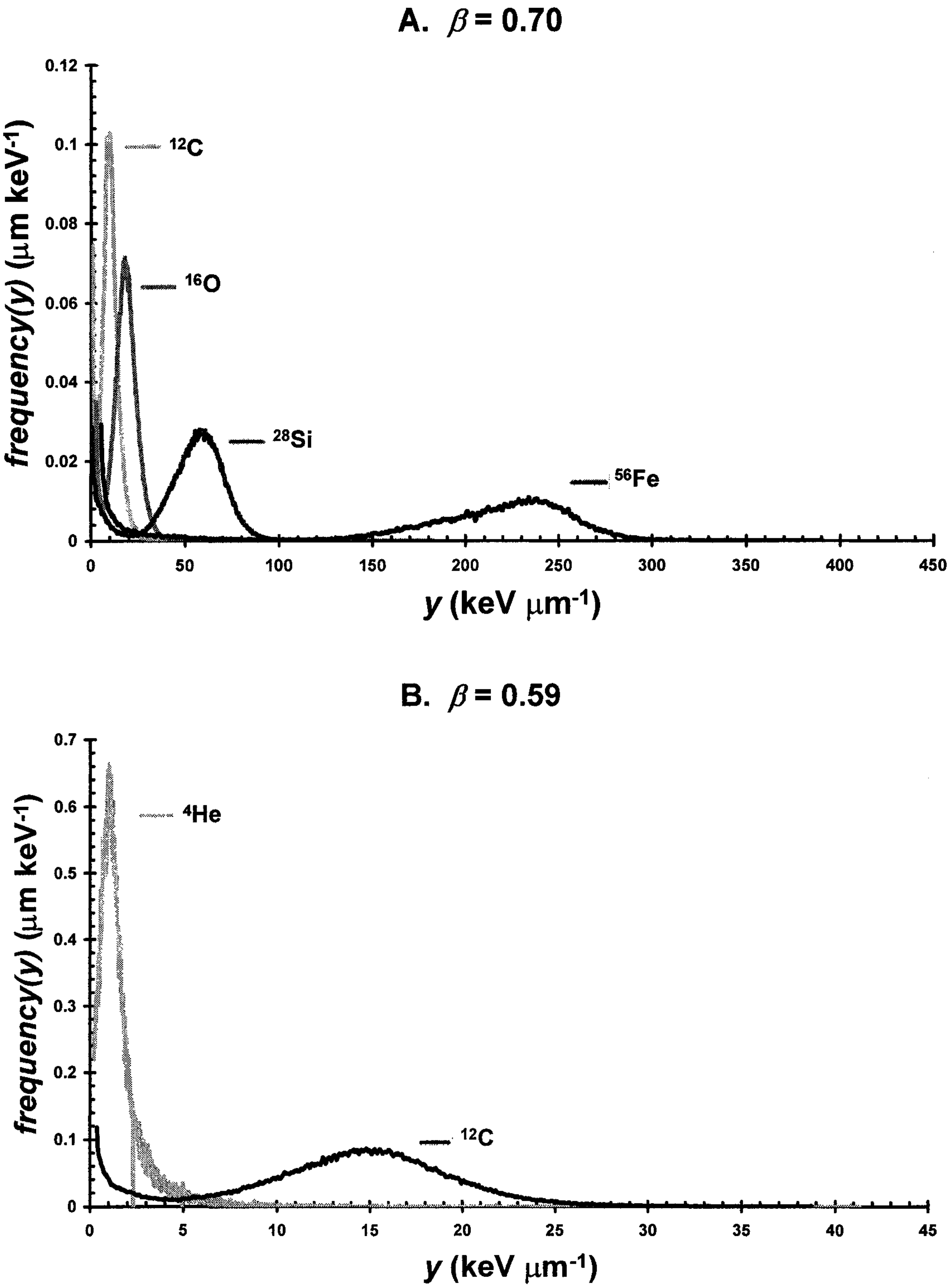

Fig. 4.20. Distributions of the lineal energy response of the TEPC, smoothed (Savitzky and Golay, 1964). Lineal energy responses of the TEPC to ions of velocity $\beta = 0.70$ (A) and ions of velocity $\beta = 0.59$ (B).

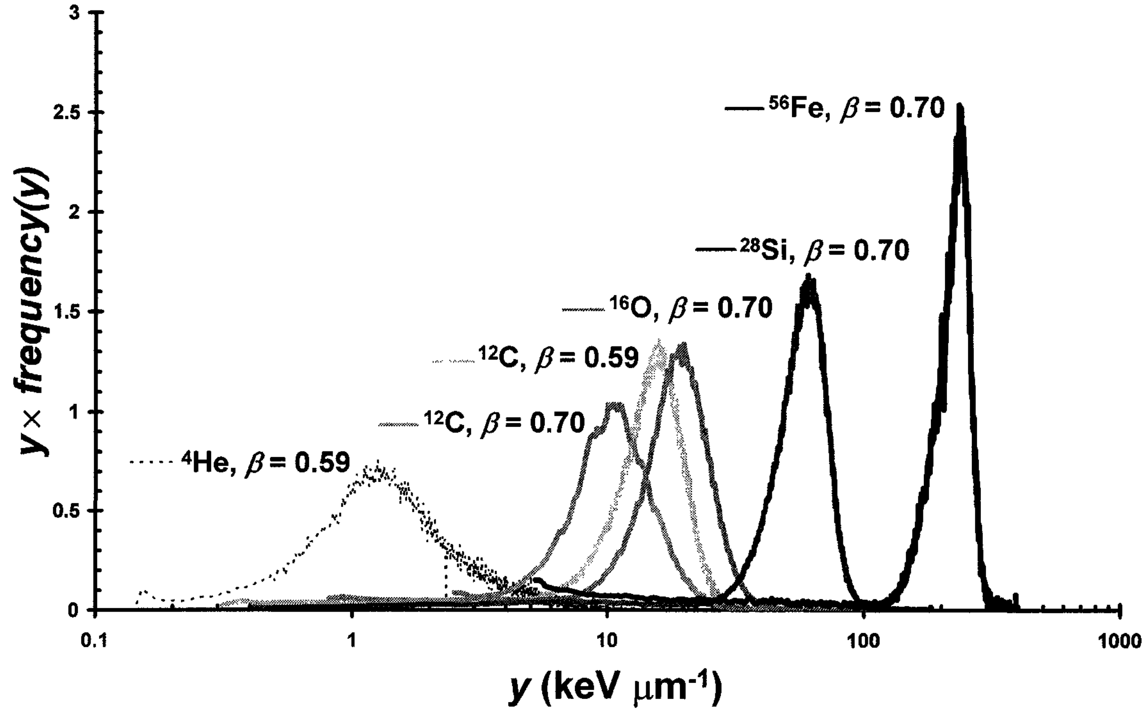

Fig. 4.21. Linear-logarithmic plot of the distributions of lineal energy. The ordinate is the product of the probability and the lineal energy. The abscissa is lineal energy.

$$\bar{y}_{f,predicted} = \int_0^{\frac{3}{2}LET} yf(y)dy = \int_0^{\frac{3}{2}LET} \frac{8}{9\cdot LET^2} y^2 dy \tag{4.6}$$

$$= \frac{8}{27\cdot LET^2} y^3 \Big|_0^{\frac{3}{2}LET} = \frac{8}{27\cdot LET^2}\left[\left(\frac{3}{2}LET\right)^3 - 0\right] = \frac{LET^3}{LET^2} = LET.$$

The dose averaged lineal energy, $\bar{y}_D$, was defined in Equation 1.7 and is the second moment of y divided by the first moment,

$$\bar{y}_D = \frac{\overline{y^2}}{\bar{y}} = \frac{\int y^2 f(y)dy}{\int yf(y)dy}.$$

The predicted $\bar{y}_D$ for a spherical TEPC based on $f_{predicted}(y)$ is

$$\bar{y}_{D,predicted} = \frac{\int_0^{\frac{3}{2}LET} y^2 f(y)dy}{\int_0^{\frac{3}{2}LET} yf(y)dy} = \frac{\int_0^{\frac{3}{2}LET} \frac{8}{9\cdot LET^2} y^3 dy}{\bar{y}_f} \tag{4.7}$$

$$= \frac{\frac{2}{9\cdot LET^2} y^4 \Big|_0^{\frac{3}{2}LET}}{LET} = \frac{\frac{2}{9\cdot LET^2}\left[\left(\frac{3}{2}LET\right)^4 - 0\right]}{LET} = \frac{\frac{9}{8}LET^2}{LET} = \frac{9}{8}LET.$$

Frequency and dose mean values for lineal energy are listed in Table 4.1.

Fig. 4.22 shows a plot of $\bar{y}_f$ and $\bar{y}_D$ as a function of charge, *Z*, for all ions. In each case, the averaged values of *y* were divided by *LET* for comparison purposes. Data for protons at $\beta = 0.53$ (172 MeV nucleon^{-1}) (Borak, 2004) were also included in the same plot. It can be seen that $\bar{y}_f$ consistently underestimated *LET* by as much as 19%. There is a slight indication that $\bar{y}_f$ approaches *LET* as *Z* decreases. For $Z = 6$ and higher, $\bar{y}_D$ was within 5% of *LET*. However, $\bar{y}_D$ was substantially greater than *LET* for ^{4}He and ^{1}H.

A plot of the measured values of frequency and dose mean lineal energy from all of the HZE studies with a TEPC are in Figs. 4.23 and 4.24. Again, $\bar{y}_f$ approaches *LET* as *Z* decreases, and the same is true as β decreases.

Noise Threshold

Although selecting a lower threshold for noise and background (see Noise and Background section above) in the *y*-distribution,

$$y_{min} = \frac{\varepsilon_{min}}{\frac{2}{3}d}, \tag{4.8}$$

has little effect on $\bar{y}_D$, where one selects a lower threshold in the *y*-distribution has a significant effect on $\bar{y}_f$. Fig. 4.25 shows the values of the ratio of $\bar{y}_f$ to *LET* for each ion for several thresholds where events with ε less than the threshold were eliminated. Values labeled "selected threshold" were the actual lower threshold values selected for

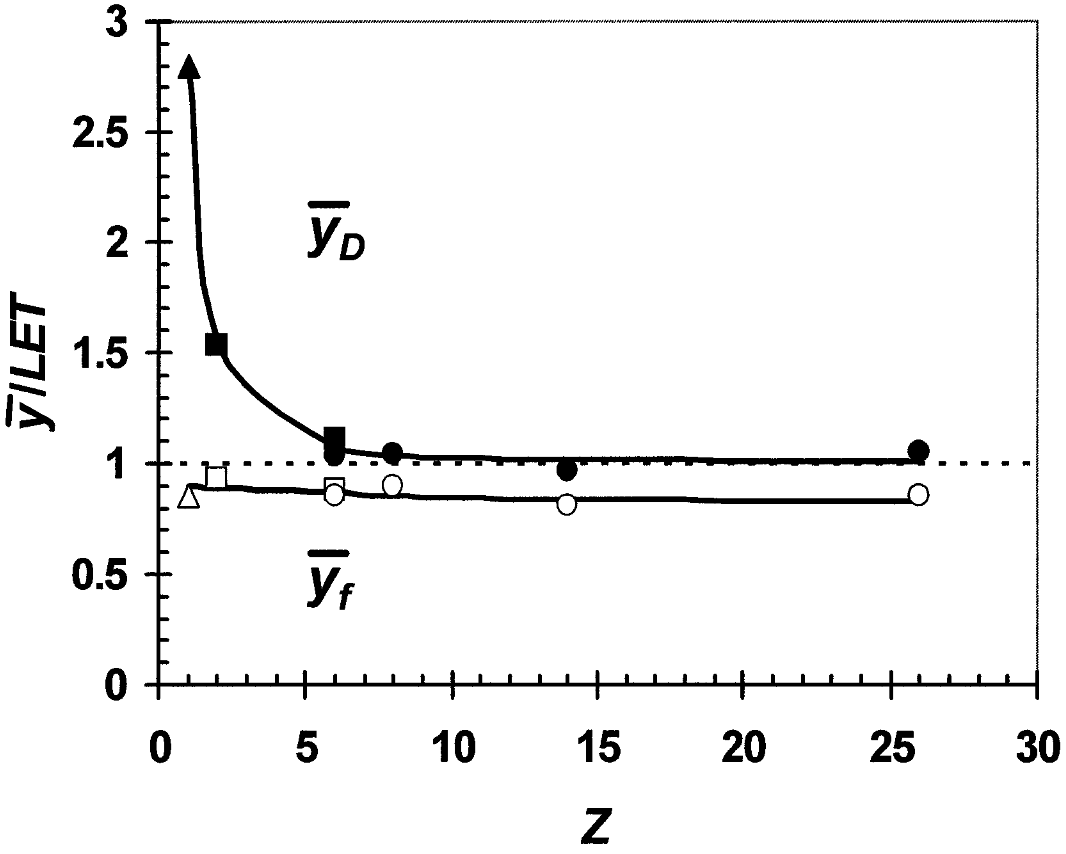

Fig. 4.22. Values of frequency averaged lineal energy (open symbols) and dose averaged lineal energy (solid symbols) as a function of charge. The circles are for ions at 376 ± 15 MeV nucleon^{-1}. The squares are for ions at 220 ± 7 MeV nucleon^{-1}. The triangles are for protons at 172 MeV (Borak, 2004).

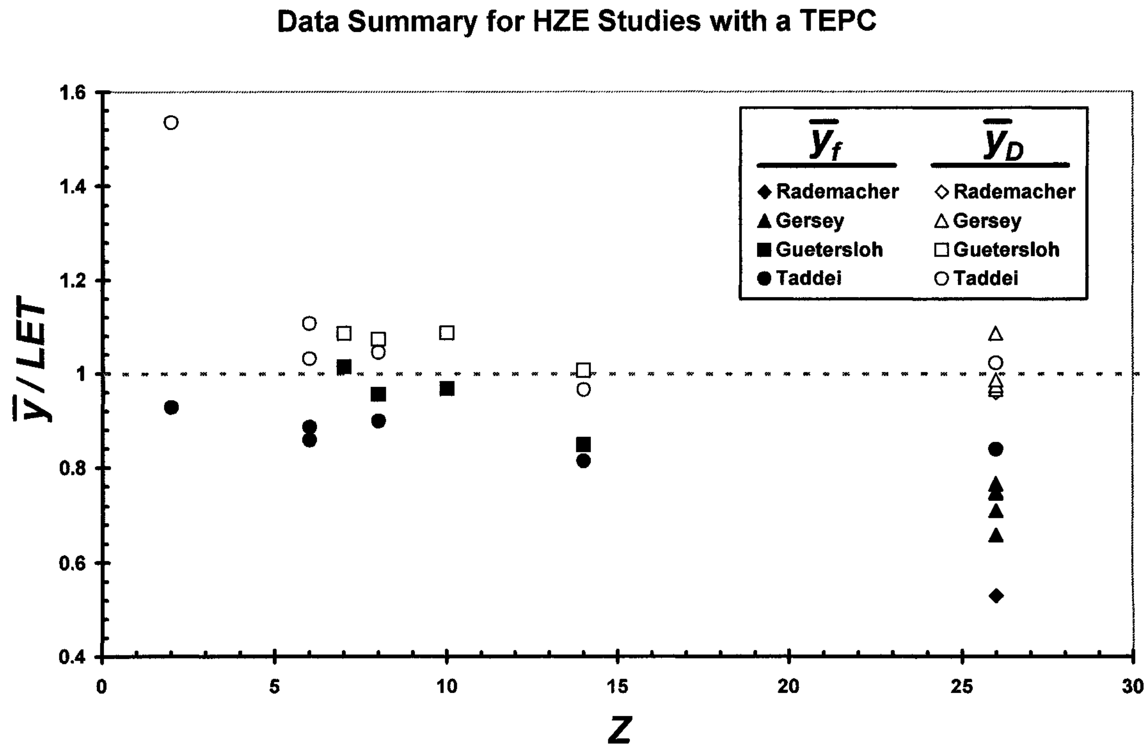

Fig. 4.23. Summary of mean lineal energies of all data for HZE studies with the same spherical TEPC (Rademacher, 1997; Rademacher *et al.*, 1998; Gersey *et al.*, 2002; Guetersloh, 2003; Guetersloh *et al.*, 2004). Frequency mean lineal energy (closed symbols) and dose mean lineal energy (open symbols) are compared to *LET* (dashed line) by dividing them by *LET* and plotting them versus atomic number.

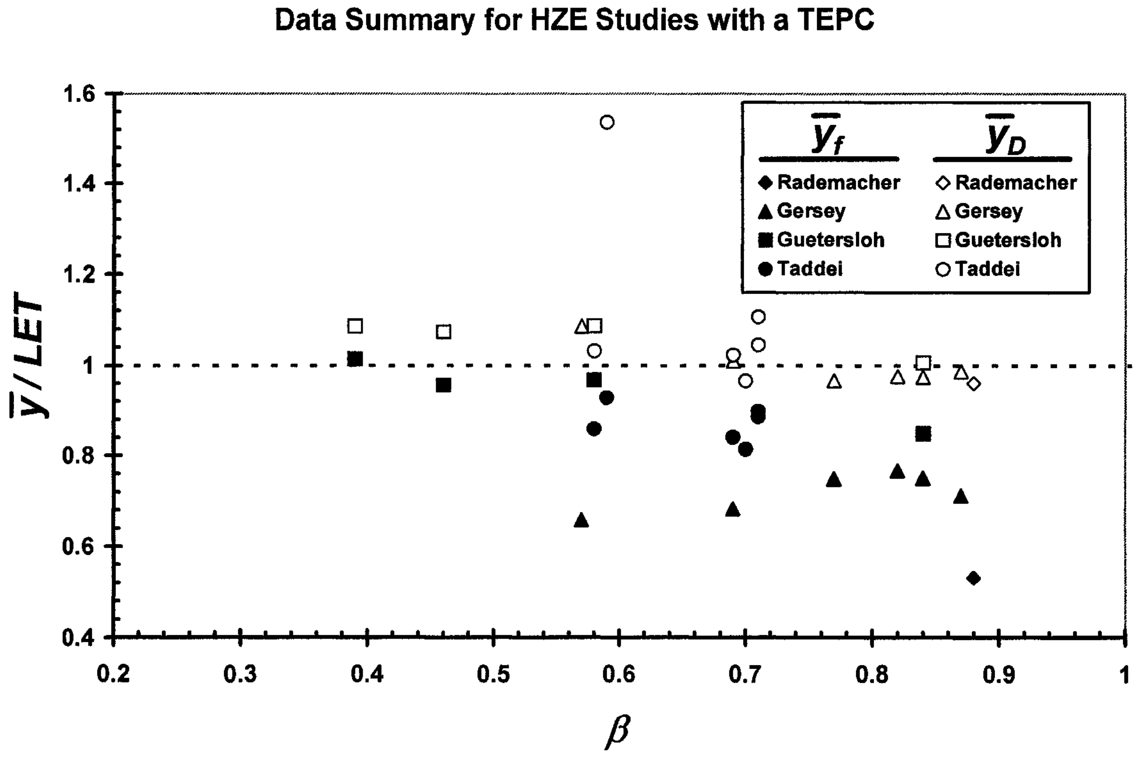

Fig. 4.24. Summary of mean lineal energies of all data for HZE studies with the same spherical TEPC (Rademacher, 1997; Rademacher *et al.*, 1998; Gersey *et al.*, 2002; Guetersloh, 2003; Guetersloh *et al.*, 2004). Frequency mean lineal energy (closed symbols) and dose mean lineal energy (open symbols) are compared to *LET* (dashed line) by dividing them by *LET* and plotting them versus velocity with respect to the speed of light.

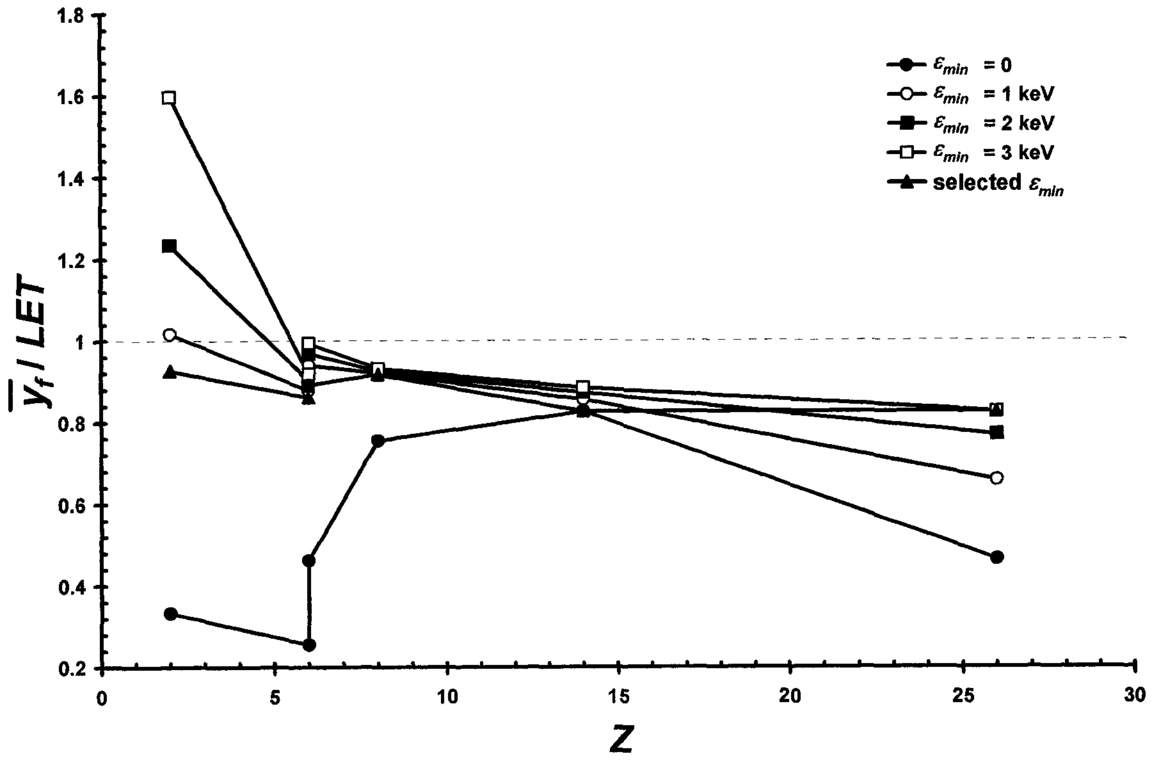

Fig. 4.25. Frequency mean lineal energy relative to *LET* of the incident ion versus atomic number for several background and noise threshold elimination levels. 'Selected ε_{min}' refers to the elimination of events less than the selected lower threshold based on the respective background and noise distribution of each ion.

the response functions of the TEPC in this study, chosen based on the values of the edge of the respective noise and background spectrum of each ion. For ions of low atomic number, $\bar{y}_f$ varied greatly depending on the selection of the lower threshold. On the other hand, only for ^{4}He was there a significant change in $\bar{y}_D$ when adjusting the noise threshold level (Fig. 4.26). In this case, the threshold levels disrupted the broad peak of the y-distribution. In other words, for higher noise threshold levels, some events where the incident ^{4}He ion traveled through the gas cavity were eliminated from the data. A protocol of assigning a universal threshold value to all TEPCs in all situations may be problematic since the noise distributions of the TEPC change in different circumstances, e.g. with various amplifier gains.

Quality Factor

The distributions of y were used to estimate mean quality factors for applications in radiation protection. The accepted value of Q was determined from *LET* of each mono-energetic ion using the relationship between quality factor and *LET*, $Q(LET)$, recommended by the ICRP (Table 1.2) (ICRP, 1991). Radiation quality based on the distributions and frequency and dose mean values of y were determined using four approaches. One approach was to assume that *LET* is equal to $\bar{y}_f$ and then determine $Q(\bar{y}_f)$. This was repeated by assuming that *LET* is equal to $\bar{y}_D$ and then determining $Q(\bar{y}_D)$. The third method was based on computing an averaged value, $\bar{Q}$, using the complete dose response function of the TEPC, $d(y)$, and the assumption that y was

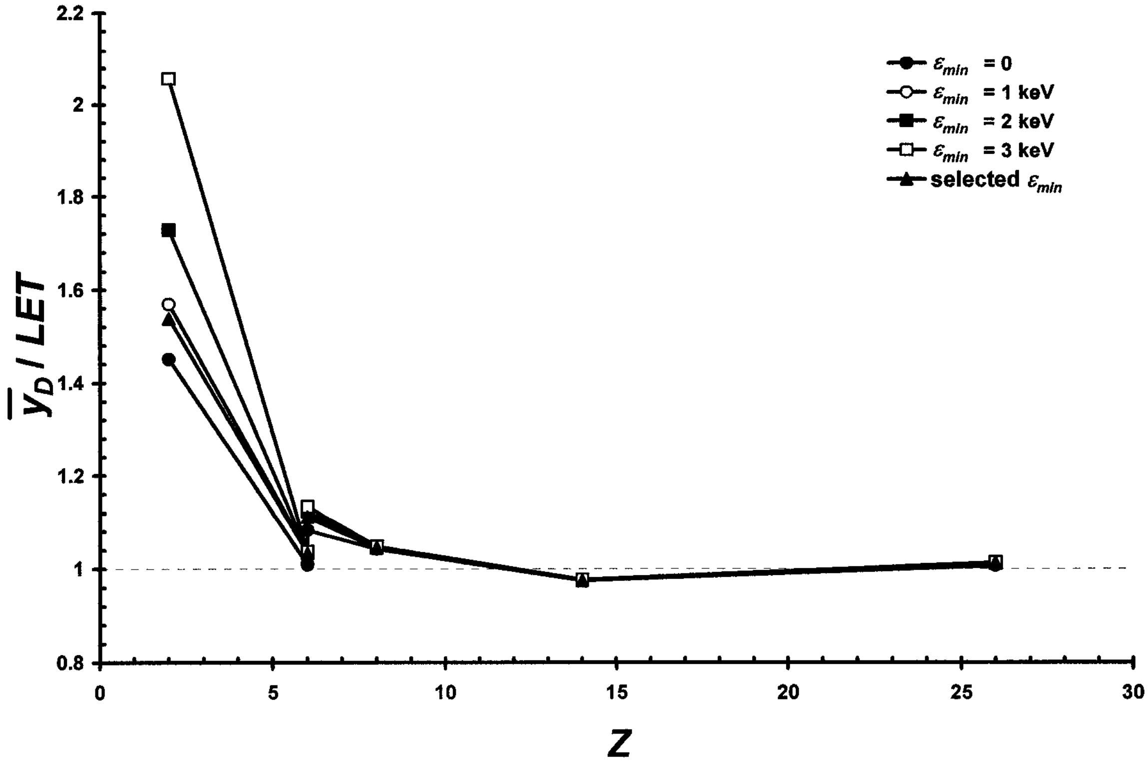

Fig. 4.26. Dose mean lineal energy relative to *LET* of the incident ion versus atomic number for several background and noise threshold elimination levels. 'Selected ε_{min}' refers to the elimination of events less than the selected lower threshold based on the respective background and noise distribution of each ion.

numerically equivalent to LET, $\overline{Q}\,[d(LET) = d(y)]$. The fourth method used a radiation quality function based on lineal energy, $q(y)$, recommended by the ICRU (ICRU, 1986) such that $Q = \overline{q}\,[d(y)]$.

The results for mean quality of all ions in this study are shown in Fig. 4.27. At 376 MeV nucleon^{-1} ($\beta = 0.70$), $Q(\overline{y}_f)$ underestimated the accepted value of Q for each ion except ^{56}Fe because $\overline{y}_f$ was always less than LET. When LET of the incident ion is less than 100 keV μm^{-1} (i.e., $Q(LET)$ with positive slope), $Q(\overline{y}_f)$ will be less than $Q(LET)$, and when LET of the ion is greater than 100 keV μm^{-1} (i.e., $Q(LET)$ with negative slope), $Q(\overline{y}_f)$ will be greater than $Q(LET)$. $Q(\overline{y}_D)$ provided the most consistently accurate estimation of Q with the exception of ^{12}C, for which Q was overestimated by 28%. Although $\overline{y}_D$ was significantly greater than LET for ^{4}He, it did not influence Q because $Q(LET)$ has constant value of 1.0 below 10 keV μm^{-1}. For the ions in this study, $\overline{Q}\,[d(LET) = d(y)]$ followed a pattern similar to $Q(\overline{y}_D)$, and $Q = \overline{q}\,[d(y)]$ made a poor estimate of the accepted quality.

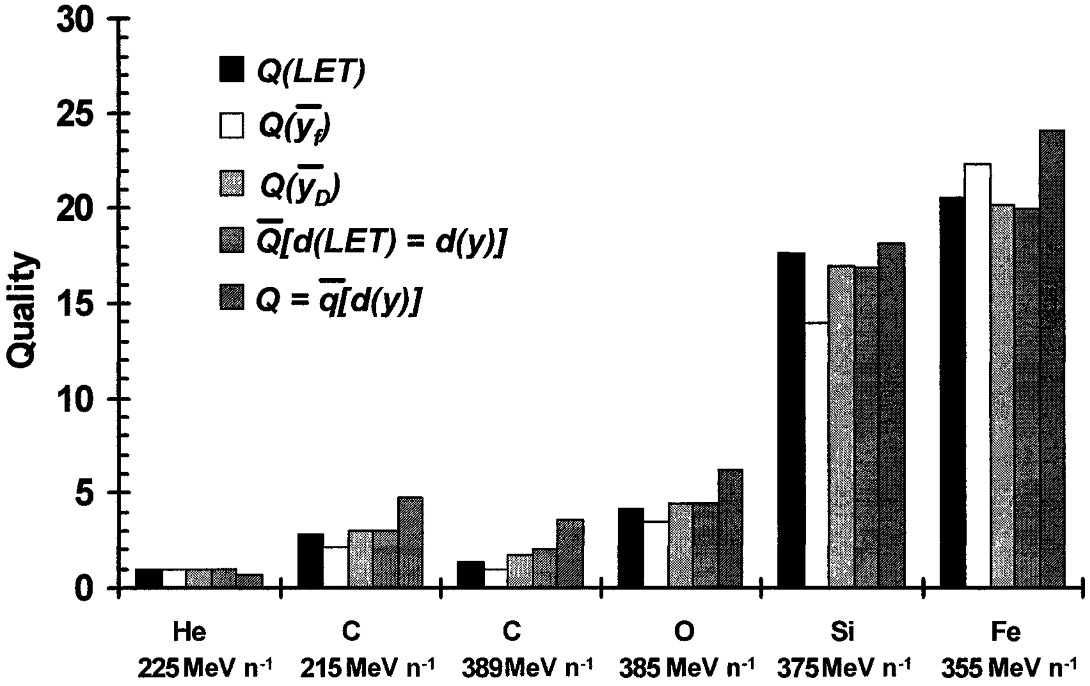

Fig. 4.27. Bar graph showing estimates of quality factor. The accepted quality factor is obtained from the exact value of *LET* for each ion and the *Q(LET)* relationship recommended by the ICRP (ICRP, 1991). $Q(\bar{y}_f)$ and $Q(\bar{y}_D)$ used the mean values of lineal energy to estimate *LET*. $\bar{Q}\,[d(LET) = d(y)]$ used the complete response function of the TEPC and the assumption that *d(LET)* = *d(y)*. $Q = \bar{q}\,[d(y)]$ is based on the ICRU method of determining quality directly from lineal energy (ICRU, 1986).

CHAPTER V: CONCLUSIONS

The response of a spherical tissue-equivalent proportional counter (TEPC) was measured for several ions that had different charge, *Z*, but with similar velocities. Specifically, data were collected for ^{12}C, ^{16}O, ^{28}Si and ^{56}Fe at 376 ± 15 MeV nucleon^{-1} ($\beta = 0.70$) and ^{4}He and ^{12}C at 220 ± 7 MeV nucleon^{-1} ($\beta = 0.59$). The gas pressure was adjusted to simulate a volume of tissue having a diameter of 1 μm for ions with velocity, $\beta = 0.70$, and 3 μm for ions with velocity, $\beta = 0.59$. Position-sensitive silicon detectors were used to determine both the trajectory and the identity of the incident ions through the detector. The spatial resolution of these detectors based on FWHM/mean was about 10% for all ions except ^{4}He.

Incident ions that passed through the center of the detector deposited only about 80% of the energy that would be expected from the product of *LET* and the simulated diameter. This was attributed to high energy delta-rays escaping from the sensitive volume and the fact that forward-moving electrons produced in the front wall of the detector did not provide complete energy compensation.

The responses of the detector in terms of energy deposition, $f(\varepsilon)$, were similar in shape for all ions. All had events with small values of energy deposition corresponding to ions that passed through the side wall of the detector but not through the gas cavity. Events with very large energy deposition were shown to be from ions that just grazed the inside wall of the detector or interacted with the anode or helical wire.

The responses of the detector, $g(\eta)$, in terms of the relative energy deposition with respect to $LET \cdot d$ ($\eta = \varepsilon / [LET \cdot d]$) were used to compare response functions of the TEPC for ions of the same velocity. As atomic number decreased, three effects were observed in the broad peaks of the distributions. First, the spread of the broad peaks of the distributions increased. This effect was due to the changing effects of energy straggling and ion-pair production with decreasing atomic number. Second, for events where $\eta > 0.2$, the means of the distributions, $\bar{\eta}_{0.2}$, remained constant. The averages of the values of $\bar{\eta}_{0.2}$ were 0.64 ± 0.02 for the $\beta = 0.70$ ions and 0.66 ± 0.03 for the $\beta = 0.59$ ions. This effect was the result of the consistency of range and energy deposition patterns for ions of the same velocity independent of their charge. Finally, a greater number of events were measured where ε was greater than the maximum based on $LET \cdot d$ (i.e., $\eta > 1$). This effect is also because of the spreading of the broad peak, both to smaller and larger η, with decreasing atomic number. In addition, the broad peaks of the distributions became more right-skewed as atomic number decreased for ions of the same velocity.

For ions of the same velocity, the small energy deposition portion of the distributions of η were nearly identical. This is because tracks of the ejected delta-rays of these ions have the same range and energy deposition patterns independent of the charge of the incident ion.

The frequency mean lineal energy, $\bar{y}_f$, was lower than the corresponding value of LET for all ions. It was noted that this quantity was particularly sensitive to the low energy threshold that was used to distinguish events with small energy depositions from background and noise. For example, changes in this threshold could change the value of $\bar{y}_f$ by a factor of 1.5 for ^{56}Fe (*LET* = 219 keV μm^{-1}) and up to a factor of 5 for ^{4}He (*LET* = 1.68 keV μm^{-1}). A protocol of assigning a universal threshold value to all TEPCs in all situations may be problematic since the noise distributions of the TEPC change in different circumstances, e.g. with various amplifier gains.

It was observed that $\bar{y}_D$ was within 10% of *LET* for $Z = 6$ to $Z = 26$. However, $\bar{y}_D$ was about 50% greater than *LET* for ^{4}He. Previous results showed that $\bar{y}_D$ was more than a factor of two greater than *LET* for ^{1}H (Borak, 2004).

The possible influence of using a simulated diameter of 3 μm for the ions at 220 MeV nucleon^{-1} has been investigated as opposed to 1 μm for the ions at 376 MeV nucleon^{-1}. When the simulated diameter was increased from 1 μm to 3 μm for ^{56}Fe ions at 1050 MeV nucleon^{-1}, $\bar{y}_f$ decreased by about 4% and $\bar{y}_D$ decreased by about 2% (Rademacher, 1997). The data for ^{12}C, shown in Table 1.3, were consistent with these observations. It is thus concluded that the increase in $\bar{y}_D$ observed for ^{4}He was not due to changes in the simulated diameter.

The dose averaged lineal energy, $\bar{y}_D$, is the second moment of the frequency distribution, $\overline{y^2}$, divided by the first moment, $\bar{y}$. The second moment is very sensitive to the number of events with large energy depositions. Even though there are compensating events with reduced energy deposition, this spread in the data causes $\bar{y}_D$ to increase as *LET* becomes small. At low *LET*, real events in the detector overlap with noise. This has the effect of decreasing the denominator faster than the numerator in the definition of $\bar{y}_D$.

The data were used to estimate quality factors for applications in radiation protection. All of the methods using the data from the TEPC produced results that were within 20% of the value of the accepted quality factor based on the value of *LET* for each ion and *Q(LET)* from the ICRP. $Q(\bar{y}_D)$ seemed to be the most consistent estimator of quality factor. When *LET* was greater than 20, $\bar{y}_D$ was not strongly influenced by changes in the number of very small energy deposition events recorded by the TEPC. Although $\bar{y}_D$ was significantly larger than *LET* for ^{4}He and ^{1}H, this result fortuitously did not affect quality factor since *Q(LET)* has a constant value equal to 1.0 in that domain of *LET*. For the ions in this study, $\bar{Q}$ [*d(LET)* = *d(y)*] followed a pattern similar to $Q(\bar{y}_D)$, and $Q = \bar{q}\,[d(y)]$ made a poor estimate of the accepted quality.

Summary of HZE Studies with a Tissue-Equivalent Proportional Counter

It is helpful to summarize the conclusions made in this and in previous studies of the response of an identical spherical TEPC to HZE ions (Rademacher, 1997; Rademacher *et al.*, 1998; Gersey *et al.*, 2002; Guetersloh, 2003; Guetersloh *et al.*, 2004; Borak *et al.*, 2004). The following list of conclusions for monoenergetic HZE ion beams are compiled from these studies:

- The response functions of a TEPC have a similar shape for all ions with a small energy deposition leading edge, a broad peak, and some very large energy deposition events.

  - Small energy depositions are from events where incident ions missed the gas cavity but passed through the side wall of the detector and produced delta-rays that entered and deposited energy in the gas cavity.
  - The broad peak of medium energy depositions is populated by events in which the incident ion passed through the gas cavity of the TEPC.
  - Large energy depositions are from events where the incident ions either just grazed the inside wall of the gas cavity or happened to hit the anode or helical grid wires within the cavity.
- Energy loss from delta-rays that escape the active volume of the TEPC are compensated for by delta-rays that enter the gas from interactions with the wall. As a result, charged-particle equilibrium was satisfied when all events were included in the measurement of absorbed dose, confirming that the TEPC accurately measures absorbed dose.
- Current models overestimate radial energy loss from the TEPC.
- For ions of the same velocity, after dividing by $LET \cdot d$, the small energy deposition portion of the response functions of the TEPC are nearly identical.
- Ions of the same velocity have similar delta-ray wall effects.
- The distribution of the energy deposition response of the TEPC does not follow the expected distribution based on *LET* and the path length distribution of the detector, demonstrating that the TEPC is not an *LET* spectrometer.
- The frequency mean lineal energy underestimates *LET* by as much as 40%, and the amount that it underestimates LET decreases as atomic number decreases.
- The dose mean lineal energy approximates *LET* to within 10% for ions of higher

atomic number, but it overestimates *LET* for ions of low atomic number.

- Mean quality factor for the response of a TEPC to HZE ions is most accurately estimated using the definition from the ICRP (ICRP, 1991) with the assumption that *LET* is equal to the dose mean lineal energy.
- Careful consideration must be made when selecting a lower energy deposition threshold in the TEPC response. The threshold value must be adjusted with respect to the gain settings of the shaping amplifiers of the TEPC.

Recommendations for Future Work

Since the positional response of the PSDs depends on the characteristics of the incident ion, masking calibration runs should be performed for each ion beam of interest. Because the small energy deposition events are important, sufficient data without the TEPC included in the triggering should be recorded for each ion. To enhance the signal to noise ratio the preamplifiers of the position signals of the PSDs and of the TEPC should be mounted as near as possible to the detector outputs. Another method of increasing the signal to noise ratio for the TEPC is to use an EG&G ORTEC 142PC preamplifier, which has an internal gain, rather than an EG&G ORTEC 142AH preamplifier. The 142PC preamplifier, however, does not produce a fast-timing signal.

The significant effect that the noise and background threshold assignment has on the mean values of the response of a TEPC is important for radiation protection applications, especially for low-*LET* ions, and is worth further investigation with other types of TEPCs. A protocol of assigning a universal lower threshold value to all TEPCs in all situations is problematic since the noise distributions of the TEPC change in different circumstances, e.g. with various amplifier gains. The selection of a lower threshold value should be altered for different environments and gain settings.

REFERENCES

Anderson, M. E., and Neff, R. A., Neutron energy spectra of different size ^{239}Pu-Be(α-n) sources. *Nucl. Instrum. Meth.* **99**, 231-235 (1972).

Attix, F. H., *Introduction to Radiological Physics and Radiation Dosimetry*. Wiley, New York, 1986.

Badhwar, G. D., Shurshakov, V. A., and Tsetlin, V. V., Solar modulation of dose rate onboard the MIR station. *IEEE Trans. Nucl. Sci.* **44**, 2529-2541 (1997).

Badhwar, G. D., Radiation measurements in low Earth orbit: U.S. and Russian results. *Health Phys.* **79**, 507-514 (2000).

Badhwar, G. D., Shuttle Radiation Dose Measurements in the International Space Station Orbits. *Radiat. Res.* **157**, 69-75 (2002).

Berger, M.J., Coursey, J.S., and Zucker, M.A., ESTAR, PSTAR, and ASTAR: Computer Programs for Calculating Stopping-Power and Range Tables for Electrons, Protons, and Helium Ions (version 1.2.2), http://physics.nist.gov/Star, National Institute of Standards and Technology, Gaithersburg, MD (accessed June 2004).

Bichsel, H., "Passage of Charged Particles through Matter." In *American Institute of Physics Handbook* (Gray, D. E. *et al.*, Ed), pp. 8-20-8-47, McGraw-Hill, New York, 1963.

Borak, T. B., Doke, T., Fuse, T., Guetersloh, S., Heilbronn, L., Hera, K., Moyers, M., Suzuki, S., Taddei, P., Terasawa, K., and Zeitlin, C. J., Comparisons of LET distributions for protons with energies between 50 and 200 MeV using a spherical tissue equivalent proportional counter (TEPC) and a position sensitive Si-spectrometer (RRMD-III). *Radiat. Res.* (in press). (2004).

Bottollier-Depois, J. F., Lebaron-Jacobs, L., Siegrist, M., Duvivier, E., Almarcha, B., Dachev, T. P., Semkova, J. V., Matviichuk, Y. N., Koleva, R. T., Tomov, B. T., Baynov, P. T., Petrov, V. M., Shurshakov, V. V., Bengin, V., and Koslova, S. B., Tissue equivalent detector data obtained recently on MIR space station. Comparison with solid state detector data. *Adv. Space Res.* **18**, 171-174 (1996).

Burmeister, J., Kota, C., Maughan, R. L., Waker, A. J., Riley, K., and Wielopolski, L., Application of TEPC microdosimetry to boron neutron capture therapy. *Radiat. Prot. Dosim.* **99**, 351-352 (2002).

Chee, P. A., Braby, L. A., and Conroy, T. J., Potential doses to passengers and crew of supersonic transports, *Health Phys.* **79**, 547-552 (2000).

Clarck, R., *The Life and Times of Einstein.* The World Publishing, New York, 1971.

Cucinotta, F. A., Katz, R., Wilson, J. W., and Dubey, R. R., *Heavy Ion Track-Structure Calculations for Radial Dose in Arbitrary Materials.* NASA Technical Paper 3497, 1995.

Cucinotta, F. A., Wilson, J. W., Williams, J. R., and Dicello, J. F., Analysis of MIR-18 results for physical and biological dosimetry: radiation shielding effectiveness in LEO. *Radiat. Meas.* **32**, 181-191 (2000).

Cucinotta, F. A., Shimmerling, W., Wilson, J. W., Peterson, L. E., Badhwar, G. D., Daganti, P. B., and Dicello, J. F., *Space Radiation Cancer Risk Projections for Exploration Missions: Uncertainty Reduction and Mitigation.* NASA JSC Document, JSC-29295, NASA Center for AeroSpace Information, Hanover, MD, January 2001.

Cucinotta, F. A., Saganti, P. B., Hu, X., Kim, M. Y., Cleghorn, T. F., Wilson, J. W., Tripathi, R. K., and Zeitlin, C. J., Physics of the Isotopic Dependence of Galactic Cosmic Ray Fluence Behind Shielding. NASA Technical Paper TP-2003-210792, NASA Center for AeroSpace Information, Hanover, MD, February 2003.

Craven, P. A. and Rycroft, M. J., An assessment of galactic cosmic radiation quality considering heavy ion track structures within the cellular environment. *Adv. Space Res.* **18**, 45-49, 1996.

Doke, T., Hayashi, T., and Borak, T. B., Comparisons of LET Distributions Measured in Low-Earth Orbit Using Tissue-Equivalent Proportional Counters and the Position-Sensitive Silicon-Detector Telescope (RRMD-III). *Radiat. Res.* **156**, 310-316 (2001).

ESV, *The Holy Bible, English Standard Version.* Crossway Bibles, a division of Good News Publishers, Wheaton, Illinois, 2001.

Garty, G., Shchemelinin, S., Breskin, A., Chechik, R., Assaf, I., Orion, I., Bashkirov, V., Schulte, R., and Grosswendt, B., The performance of a novel ion-counting nanodosimeter. *Nucl. Instr. Meth.* **A492**, 212-235 (2002).

Gerdung, S., Pihet, P. , Grindborg, J. E., Roos, H., Schrewe, U. J., and Schuhmacher, H., Operation and Application of Tissue-Equivalent Proportional Counters. *Radiat. Prot. Dosim.* **61**, 381-404 (1995).

Gersey, B. B., Borak, T. B., Guetersloh, S. B., Zeitlin, C., Heilbronn, L., Murakami, T., and Iwata, Y., The response of a spherical tissue-equivalent proportional counter to ^{56}Fe particles from 200-1000 MeV/nucleon. *Radiat. Res.* **157**, 350-360 (2002).

GSI, GSI home page, http://www.gsi.de/index.html (accessed April 2004).

Guetersloh, S. B., *Response of a Tissue Equivalent Proportional Counter to Different Ions Having a Similar Linear Energy Transfer*, Ph.D. thesis, Colorado State University, Fort Collins, Colorado, 2003.

Guetersloh, S. B., Borak, T. B., Taddei, P. J., Zeitlin, C., Heilbronn, L., Miller, J., Murakami, T., and Iwata, Y., The response of a spherical tissue-equivalent proportional counter to different ions having similar linear energy transfer. *Radiat. Res.* **161**, 64-71 (2004).

ICRP, *Recommendations of the International Commission on Radiological Protection.* Publication 26, International Commission on Radiological Protection, *Annals of the ICRP.* **1**, Pergamon Press, New York, 1977.

ICRP, *Recommendations of the International Commission on Radiological Protection.* Publication 60, International Commission on Radiological Protection, *Annals of the ICRP.* **21**, Pergamon Press, New York, 1991.

ICRU, *Radiation Quantities and Units.* Report 11, International Commission on Radiation Units and Measurements, Washington, D.C., 1968.

ICRU, *Microdosimetry.* Report 36, International Commission on Radiation Units and Measurements, Bethesda, MD, 1983.

ICRU, *Stopping Powers for Electrons and Positrons.* Report 37, International Commission on Radiation Units and Measurements, Bethesda, MD, 1984.

ICRU, *The Quality Factor in Radiation Protection.* Report 40, International Commission on Radiation Units and Measurements, Bethesda, MD, 1986.

ICRU, *Stopping Powers and Ranges for Protons and Alpha Particles.* Report 49, International Commission on Radiation Units and Measurements, Bethesda, MD, 1993.

Kellerer, A. M., Considerations on the Random Traversal of Convex Bodies and Solutions for General Cylinders. *Radiat. Res.* **47**, 359-376 (1971a).

Kellerer, A. M., An assessment of wall effects in microdosimetric measurements. *Radiat. Res.* **47**, 377 (1971b).

Kellerer, A. M., Event simultaneity in cavities. Theory of the distortions of energy deposition in proportional counters. *Radiat. Res.* **48**, 216 (1971c).

Kellerer, A. M. and Hahn, K., The quality factor for neutrons in radiation protection: physical parameters. Radiat. Prot. Dosim. 23, 73-78 (1988).

Kellerer, A. M. and Rossi, H. H., "Summary of Quantities and Functions Employed in Microdosimetry." In *Second Symposium on Microdosimetry* (Ebert, H. G., Ed), pp. 843-853, Commission of the European Communities, Brussels, Belgium, 1968.

Knoll, G. F., *Radiation Detection and Measurement.* 3rd Edition. John Wiley & Sons, New York, 2000.

Kraft, G., Kramer, M., and Sholz, M., LET, track structure, and models. *Radiat. Envron. Biophys.* **31**, 161-180 (1992).

Lindborg, L., Kyllonen, J. E., Beck, P., Bottollier-Dopois, J. F., Gerdung, S., Grillmaier, R. E., and Schrewe, U., The use of a TEPC for reference dosimetry. *Radiat. Prot. Dosim.* **86**, 285-288 (1999).

LLUMC, Proton Beam Therapy at Loma Linda University Medical Center, http://www.llu.edu/proton/index.html (accessed April 2004).

Maxwell, James Clerk, *A Student's Evening Hymn.* 1853.

Mallows, C. L., Some comments on Cp. *Technometrics.* **15**, 661-675 (1973).

Miller, J., Zeitlin, C., Heilbronn, L., Borak, T., Carter, T., Frankel, K. A., Fukumura, A., Murakami, T., Rademacher, S. E., Schimmerling, W., Stronach, C., Ground-based simulations of cosmic ray heavy ion interactions in spacecraft and planetary habitat shielding materials. *Acta Astronaut.* **42**, 389-394 (1998).

Miller, J., Zeitlin, C., Cucinotta, F. A., Heilbronn, L., Stephens, D., and Wilson, J. W., Benchmark Studies of the Effectiveness of Structural and Internal Materials as Radiation Shielding for the International Space Station. *Radiat. Res.* **159**, 381-390 (2003).

Nikjoo, H., Khvostunov, I. K., and Cucinotta, F. A., The Response of Tissue-Equivalent Proportional Counters to Heavy Ions. *Radiat. Res.* **157**, 435-445 (2002).

National Research Council and Space Studies Board. *Radiation Hazards to Crews of Interplanetary Missions: Biological Issues and Research Strategies.* National Academy Press, Washington, D.C., 1996.

Newton, Sir Isaac, *Philosophiae Naturalis Principia Mathematica.* 1678. Translated into English by Andrew Motte in 1729.

NCRP, *Limitation of Exposure to Ionizing Radiation.* Report Number 116, National Council on Radiation Protection and Measurements, Bethesda, MD, 1993.

NCRP, *Radiation Protection Guidance for Activities in Low-Earth Orbit.* Report Number 132, National Council on Radiation Protection and Measurements, Bethesda, MD, 2000.

NCRP, *Fluence-Based and Microdosimetric Event-Based Methods for Radiation Protection in Space.* Report Number 137, National Council on Radiation Protection and Measurements, Bethesda, MD, 2001.

NCRP, *Operational Radiation Safety Program for Astronauts: A Basic Framework.* Report Number 142, National Council on Radiation Protection and Measurements, Bethesda, MD, 2002.

NIRS, National Institute of Radiological Sciences, http://www.nirs.go.jp (accessed April 2004).

NIV, *The Holy Bible, New International Version.* International Bible Society, Zondervan Publishing House, Grand Rapids, Michigan, 1984.

Oldenburg, U. and Booz, J., "Wall effects of the spherical counter." In *Proceedings of the Second Symposium on Microdosimetry*, Report No. EUR 4452 (Ebert, H. G., Ed), p. 269, Commission of the European Communities, Brussels, Belgium, 1970.

Ott, R. L., *An Introduction to Statistical Methods and Data Analysis.* 4th Edition. Wadsworth, Belmont, California, 1993.

Piper, John, *The Pleasures of God: Meditations on God's Delight in Being God.* Revised and Expanded Edition, Multinoma Publishers, Sisters, Oregon, 2000.

Rademacher, S. E., *Wall Effects Observed in Tissue-Equivalent Proportional Counters*, Ph.D. thesis, Colorado State University, Fort Collins, Colorado, 1997.

Rademacher, S. E., Borak, T. B., Zeitlin, C., Heilbronn, L., and Miller, J., Wall Effects Observed in Tissue-Equivalent Proportional Counters from 1.05 GeV/nucleon Iron-56 Particles. *Radiat. Res.* **149**, 387-395 (1998).

Rossi, H. H. and Rosenzweig, W., A Device for the Measurement of Dose as a Function of Specific Ionization. *Radiology.* **64**, 404-410 (1955).

Rossi, H. H., "Energy distribution in the absorption of radiation." In *Advances in Biological and Medical Physics*, **11**, p. 27. Academic Press, New York, 1967.

Savitzky, A. and Golay, M. J. E., Smoothing and Differentiation of Data by Simplified Least Squares Procedures, *Anal. Chem.* **36**, 1627-1637 (1964).

Simonsen, L. C., Wilson, J. W., Kim, M. H., Cucinotta, F. A., Radiation Exposure for Human Mars Exploration. *Health Phys.* **79**, 515-525 (2000).

Simpson, J. A., "Introduction to the galactic cosmic radiation." In *Composition and Origin of Cosmic Rays* (Shapiro, M. M., Ed), p. 1, Reidel Publishing, Dorcht, Netherlands, 1983.

Srdoc, D., Experimental Technique of Measurement of Microscopic Energy Distribution in Irradiated Matter Using Rossi Counters. *Radiat. Res.* **43**, 302-319 (1970).

Tume, P., Lewis, B. J., Bennett. G. I., Pierre, M., Cousins, T., Hoffarth, B. E., Jones, T. A., and Brisson, J. R., Assessment of the cosmic radiation exposure on Canadian-based routes. *Health Phys.* **79**, 568-575 (2000).

Turner, J. E., *Atoms, Radiation, and Radiation Protection, Second Edition.* John Wiley & Sons., New York, 1995.

Waker, A. J., Principles of experimental microdosimetry. *Radiat. Prot. Dosim.* **61**, 297-308 (1995).

Walske, M. C., The Stopping Power of *K*-Electrons. *Phys. Rev.* **88**, 1283-1289 (1952).

Walske, M. C., The Stopping Power of *L*-Electrons. *Phys. Rev.* **101**, 940-944 (1956).

Walters, M., Bloom, T. F., and Grajerski, B., The NIOSH/FAA working women's health study: Evaluation of the cosmic-radiation exposures of flight attendants, *Health Phys.* **79**, 553-559 (2000).

Wefel, J. P., "Instrumentation for radiation measurements in space." In *Proceedings of the Workshop on the Radiation Environment of the Satellite Power System* (W. Schimmerling and S. B. Curtis, Eds.), Lawrence Berkeley National Laboratory report LBL-8581, September 15, 1978.

Wilson, J. W., Miller, J., Konradi, A., and Cucinotta, F., *Shielding Strategies for Human Space Exploration.* NASA Conference Publication 3360, NASA Langley Research Center, Hampton, VA, December 1997.

Wong, M., Schimmerling, W., Phillips, W. M., Ludewigt, B. A., Landis, D. A., Walton, J. T., and Curtis, S. B., The multiple Coulomb scattering of very heavy charged particles. *Med. Phys.* **17**, 163-171 (1990).

Zeitlin, C. J., Frankel, K. A., Gong, W., Heilbronn, L., Lampo, E. J., Leries, R., Miller, J., and Schimmerling, W., A modular solid state detector for measuring high energy heavy ion fragmentation near the beam axis. *Radiat. Meas.* **23**, 65-81 (1994).

Zirkle, R. E., Marchbank, D. F., and Kuck, K. D., Exponential and Sigmoid Survival Curves Resulting from Alpha and X Irradiation of Aspergillus Spores. *J. Cell. Comp. Physiol. Suppl. 1*, **39**, 75-85 (1952).

APPENDIX A: SIMULATED DIAMETER CALCULATION

General

A range of tissue diameters may be simulated by adjusting the pressure of the gas in the active volume of a TEPC. The composition of the gas is designed so that incident charged particles that pass through the active volume deposit energy in the gas with the same patterns as through tissue. Thus, the gas is called "tissue-equivalent." In this study, two gas pressures were used in the TEPC gas cavity, 33.0 Torr and 99.0 Torr, to simulate spheres of tissue with diameters of 1 μm and 3 μm, respectively.

Calculations

In the calculation of the simulated tissue diameter, the following relationship was used:

$$\rho_G d_G = \rho_T d_T,$$

$$\text{or } d_T = \frac{\rho_G d_G}{\rho_T}, \tag{A.1}$$

where ρ_G and ρ_T are the densities of TE gas and tissue, respectively, and d_G and d_T are the diameters of TE gas and tissue, respectively (see Equations 3.5 and 3.6). In the spherical TEPC used in these experiments, d_G was 12.7 mm. For a constant volume and temperature, the density of tissue is 1.04 g cm^{-3}. The density of the gas depends on the pressure of the gas and the gas composition.

First, the density of the gas at 33.0 Torr will be determined. The density of any gas is defined as

$$\rho_G = \frac{m_G}{V_G} \tag{A.2}$$

where m_G is the mass of the gas and V_G is the volume of the gas. In these experiments, the composition of propane-based TE gas (see Table 3.1) was approximately the same as the ICRU standard composition (percent fractions by volume) (ICRU, 1984):

$\%_{C_3H_8}$:	55.0 %
$\%_{CO_2}$:	39.6 %
$\%_{N_2}$:	5.4 %

Applying Boyle's Law, assuming that this gas may be considered essentially ideal, and assuming a room temperature of 20.0 °C, the entire gas volume had the following number of moles:

$$n_G = \frac{PV_G}{RT} = \frac{(33.0\,\text{Torr})\left((\pi/6)\cdot(1.27\,\text{cm})^3\right)}{(62.37\,\text{L Torr mol}^{-1}\,\text{K})(293.2\,\text{K})}\cdot\frac{1\,\text{L}}{1000\,\text{cm}^3} = 1.94\times10^{-6}\,\text{mol}. \tag{A.3}$$

Therefore, each component of the gas was of the amount,

$$\begin{aligned}
n_{C_3H_8} &= \%_{C_3H_8} \cdot n_G &&= 55.0\,\% \cdot 1.94 \times 10^{-6}\,\mathrm{mol} &&= 1.06 \times 10^{-6}\,\mathrm{mol} \\
n_{CO_2} &= \%_{CO_2} \cdot n_G &&= 39.6\,\% \cdot 1.94 \times 10^{-6}\,\mathrm{mol} &&= 7.67 \times 10^{-7}\,\mathrm{mol} \\
n_{N_2} &= \%_{N_2} \cdot n_G &&= 5.4\,\% \cdot 1.94 \times 10^{-6}\,\mathrm{mol} &&= 1.05 \times 10^{-7}\,\mathrm{mol}\,.
\end{aligned}$$

The total mass of the gas was

$$\begin{aligned}
m_G &= m_{C_3H_8} + m_{CO_2} + m_{N_2} \qquad\qquad (A.4) \\
&= n_{C_3H_8} A_{C_3H_8} + n_{CO_2} A_{CO_2} + n_{N_2} A_{N_2} \\
&= \left(1.06 \times 10^{-6}\,\mathrm{mol}\right)\left(44.096\,\mathrm{g\,mol^{-1}}\right) + \left(7.67 \times 10^{-7}\,\mathrm{mol}\right)\left(44.010\,\mathrm{g\,mol^{-1}}\right) \\
&\quad + \left(1.05 \times 10^{-7}\,\mathrm{mol}\right)\left(28.013\,\mathrm{g\,mol^{-1}}\right) \\
&= 8.36 \times 10^{-5}\,\mathrm{g}\,.
\end{aligned}$$

Therefore, the density of the gas at 33.0 Torr was

$$\rho_G = \frac{m_G}{V_G} = \frac{8.34 \times 10^{-5}}{(\pi/6) \cdot (1.27\,\mathrm{cm})^3} = 7.78 \times 10^{-5}\,\mathrm{g\,cm^{-3}}\,,$$

and the simulated tissue diameter at 33.0 Torr was

$$d_T = \frac{\rho_G d_G}{\rho_T} = \frac{\left(7.80 \times 10^{-5}\,\mathrm{g\,cm^{-3}}\right)\left(1.27\,\mathrm{cm}\right)}{1.04\,\mathrm{g\,cm^{-3}}} \cdot \frac{10^4\,\mu\mathrm{m}}{1\,\mathrm{cm}} = 0.952\,\mu\mathrm{m}\,.$$

The same procedure was used to calculate the gas density and simulated tissue diameter for a gas pressure of 99.0 Torr. At that pressure, the density of the gas was 2.34 × 10^{-4} g cm^{-3}, and the simulated diameter was 2.86 μm.

Simplification

For a half-inch-diameter spherical TEPC filled with the propane-based TE gas used in this experiment and at a temperature of 20 °C, the calculations for ρ_G may be simplified.

$$\rho_G = \frac{m_G}{V_G} = \frac{n_{C_3H_8}A_{C_3H_8} + n_{CO_2}A_{CO_2} + n_{N_2}A_{N_2}}{V_G}$$

$$= \left(\frac{\%_{C_3H_8}A_{C_3H_8} + \%_{CO_2}A_{CO_2} + n_{N_2}A_{N_2}}{V_G}\right)\cdot n_G$$

$$= \left(\frac{\%_{C_3H_8}A_{C_3H_8} + \%_{CO_2}A_{CO_2} + n_{N_2}A_{N_2}}{V_G}\right)\cdot \frac{PV_G}{RT}$$

$$= \left(\frac{\%_{C_3H_8}A_{C_3H_8} + \%_{CO_2}A_{CO_2} + n_{N_2}A_{N_2}}{RT}\right)\cdot P.$$

Therefore,

$$\rho_G = K_1 \cdot P, \qquad \text{(A.5)}$$

where

$$K_1 = \frac{\%_{C_3H_8} A_{C_3H_8} + \%_{CO_2} A_{CO_2} + n_{N_2} A_{N_2}}{RT} = 2.36 \times 10^{-6} \text{ g cm}^{-3} \text{ Torr}. \tag{A.6}$$

Under the same conditions, the calculations for d_T may also be simplified:

$$d_T = \frac{\rho_G d_G}{\rho_T} = \frac{K_1 d_G}{\rho_T} \cdot P. \tag{A.7}$$

Therefore,

$$d_T = K_2 \cdot P, \tag{A.8}$$

where

$$K_2 = \frac{K_1 d_G}{\rho_T} = 0.0288\, \mu\text{m Torr}^{-1}.$$

Conclusion

For the $\beta = 0.70$ experiments described in this study, the TEPC gas pressure was 33.0 Torr. At that pressure, the gas density was 7.78×10^{-5} g cm^{-3}, and the simulated tissue diameter was 0.952 μm. Throughout this work this simulated tissue diameter is called “1 μm.” For the $\beta = 0.59$ experiments, the TEPC gas pressure was 99.0 Torr, producing a gas density of 2.34×10^{-4} g cm^{-3} and a simulated tissue diameter of 2.86 μm. Throughout this work this simulated tissue diameter is called “3 μm.”

APPENDIX B: CALIBRATION OF THE TEPC

To calibrate the response of the TEPC, four calibration points related known energies deposited to the amplitude of the voltage pulses of the TEPC shaping amplifiers, or pulse heights. Pulse heights were recorded into bins, or channels, using a multichannel analyzer (MCA) so that the number of events in the pulse height channels could be displayed versus the channel number values. The result was a pulse height distribution. Since the pulse height was ultimately proportional to the energy deposited in the TEPC, the pulse height distributions could be calibrated into energy deposited distributions.

Three calibration points were obtained from the response of the TEPC to the alpha particles emitted from an internal ^{244}Cm alpha source. One additional calibration point was obtained using the maximum energy deposition, or the "proton edge," of secondary protons originating from incident neutron interactions with the wall of the detector. The linearity of both the MCA and TEPC shaping amplifiers were also confirmed. A linear regression between channel numbers in the MCA and channel numbers of the analog-to-digital converters in the data acquisition system used in the experiments finally associated the data acquisition system channels to energy deposited in the TEPC.

For the following data, the TEPC energy signal was sent first to an external EG&G ORTEC 142AH charge-sensitive preamplifier and then split into two EG&G ORTEC 572 shaping amplifiers—all the same devices that were used in the experiments.

Background spectra were recorded in the same environment with identical settings and subtracted from each recorded spectrum. For simplicity and since the energies deposited that were used for calibration were from ions of low energy, the assumption was made in determining the calibration points that all energy lost by the incident ion while traveling through the gas cavity was deposited in the detector.

Alpha Spectrum

The response of the TEPC to 5.805-MeV (76.4%) and 5.763-MeV (23.6%) alpha particles emitted by an internal ^{244}Cm alpha source was recorded for gains in each shaping amplifier of ×2.5, ×5, and ×10 and for simulated diameters, *d*, of both 1 and 3 μm. For each spectrum, the alpha peak was determined to be the mean of the highest peak, the half-crossing alpha peak was the mean of the secondary peak populated by alpha particles that stopped in the anode or helical wire, and value corresponding to the maximum energy deposition of an alpha particle, or the "alpha edge," was determined to be at the very edge of the distribution. For gains of ×5 and ×10, the alpha edge was off-scale. The pulse height distribution for the TEPC at $d = 1$ μm operating with a gain of ×2.5 in the shaping amplifier that was used for low gain in the experiments is shown in Fig. B.1. For this case, the alpha edge was channel 315, the alpha peak was channel 97, and the half-crossing alpha peak was channel 51.6.

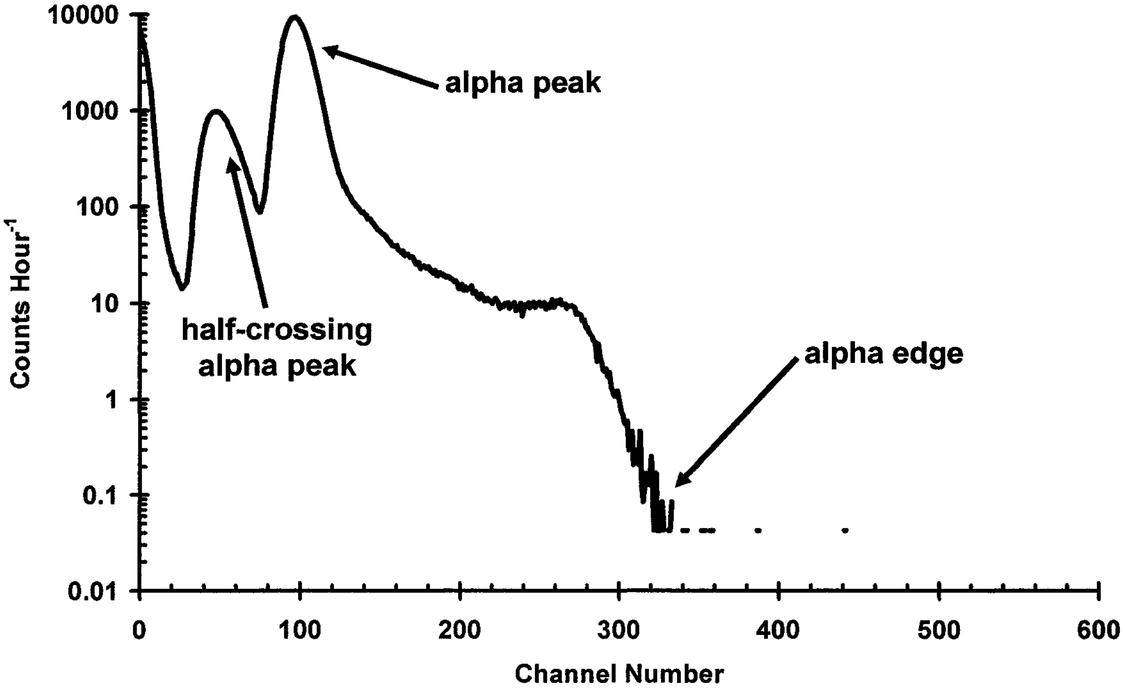

Fig. B.1. Pulse height distribution of the TEPC with a simulated diameter of 1 μm and a shaping amplifier gain of ×2.5 for the internal ^{244}Cm alpha source of the TEPC. Pulse heights were recorded into 512 channels by a multichannel analyzer, and a background distribution was subtracted. The locations of selected calibration points are shown on the plot.

Proton Spectrum

The response of the TEPC to charged particles produced by interactions in the wall of uncharged particles emitted by an external plutonium-beryllium neutron source was recorded for gains in each shaping amplifier of ×2.5, ×5, and ×10 and for simulated diameters of both 1 and 3 μm. From these plots, the proton edges were determined to be at the very edge of the distribution. For $d = 1$ μm and gain = ×2.5 in the shaping amplifier that was used for low gain in the experiments (Fig. B.2), the proton edge was channel 111.

Calculation of ε for Each Calibration Point

Calculations of energy deposition were made based on mass electronic stopping power data determined using the online version of ASTAR for alpha particles and PSTAR for protons (Berger *et al.*, 2004), which are stopping power and range calculators for ^{4}He ions (alpha particles) and protons, respectively. The equation for finding energy deposited in a target, assuming that all energy lost by the incident ion is deposited in the target, is

$$\varepsilon = \int_0^x \left(\frac{dE}{dx}\right) dx = \int_0^x LET dx \approx \rho \int_0^x \left(\frac{S}{\rho}\right) dx, \tag{B.1}$$

where x is the pathlength of the ion through the target. This was approximated by the following relationship:

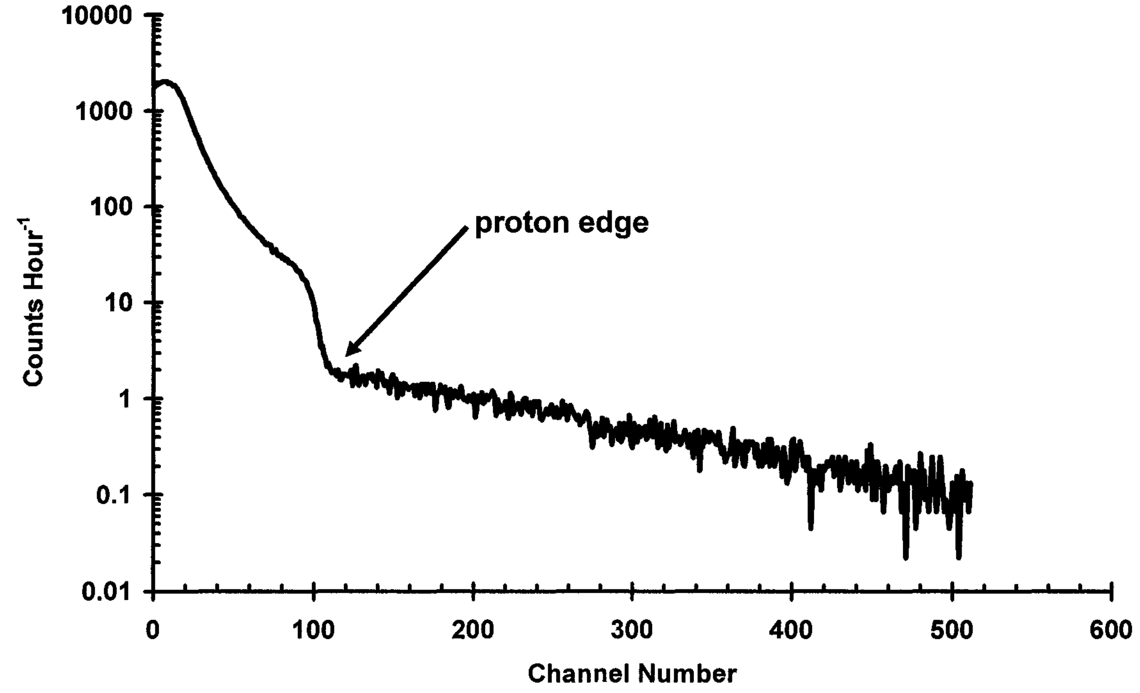

Fig. B.2. Pulse height distribution of the TEPC with a simulated diameter of 1 μm and a shaping amplifier gain of ×2.5 for a plutonium-beryllium multienergetic (see Fig. B.4) neutron source from the TEPC. Pulse heights were recorded into 512 channels by a multichannel analyzer, and a background distribution was subtracted. The location of the selected proton edge is shown on the plot.

$$\varepsilon = \rho \sum_{i=1}^{n} \left(\frac{S}{\rho} \right)_i (\Delta x)_i \qquad \text{(B.2)}$$

for a sufficient number of n iterations.

Alpha Particles

In calculating ε for calibration points from the alpha spectrum, an average original energy of 5.795 MeV was used for the alpha particles. At the gas chamber, the energy of the alpha particles are reduced to about 5.750 MeV. For alpha particles with an initial energy of 5.750 MeV, the energy deposited across 12.7 mm of propane-based TE gas at 99 Torr ($d = 3$ μm, $\rho = 2.34 \times 10^{-4}$ g cm^{-3}) is 255 keV. For the same alpha particles traveling only half-way across the same target, the energy deposited across 6.35 mm of propane-based TE gas is 126.5 keV.

By reducing the pressure in order to simulate a volume of tissue that has $d = 1$ μm the gas pressure is reduced to 33 Torr ($\rho = 7.80 \times 10^{-5}$ g cm^{-3}) for the TEPC used in this study, and the energy deposition is decreased by about a factor of 3. In this case, the energy deposited in the gas for these alphas that cross the diameter of the gas, $\varepsilon = 84.0$ keV. For alphas that cross only half of the diameter of the gas, $\varepsilon = 42.0$ keV.

The maximum ε for alpha particles in the gas was the maximum value of ε calculated using Equation B.2 for all possible initial energies. The maximum ε of alpha particles for $d = 3$ μm is from the slowing down of alpha particles with an initial energy of 1060 keV. The initial energy required to deposit the maximum ε of alpha particles for $d = 1$ μm is 750 keV (Fig. B.3). These energies can be achieved by alpha particles from

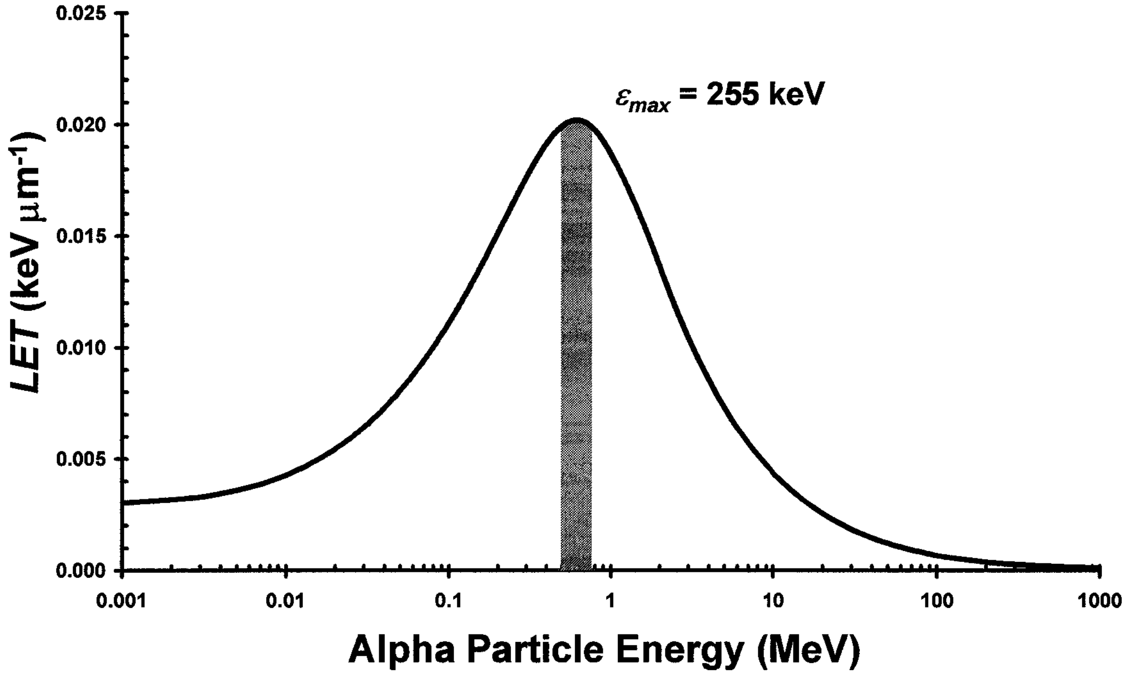

Fig. B.3. *LET*-distribution for alpha particles in 33-Torr propane-based TE gas. The shaded region represents the integral of *LET* from initial energy, $E = 750$ keV, (or initial position, $x = 0$) to final energy, $E = 496$ keV (or final position, $x = 12.7$ mm).

the internal alpha source of the TEPC that pass partially through the wall of the detector. Of course, it is extremely rare for an alpha particle to graze a portion of the wall and also have a pathlength equal to the diameter of the detector as shown in Fig. B.1. For alpha particles traveling through propane-based TE gas, the maximum ε for $d = 3$ μm is 741 keV, and the maximum ε for $d = 1$ μm is 255 keV.

Protons

Protons are produced by elastic collisions (n,p) between incident neutrons and primarily hydrogen and nitrogen nuclei of the A-150 TE plastic wall of the TEPC. A plutonium-beryllium source produced neutrons of a range of energies from 0.025 eV to 11 MeV (Anderson and Neff, 1972), which had a mean energy of 4.5 MeV. The energy distribution of these neutrons was similar to Fig. B.4. The secondary protons had energy distributions that ranged with uniform probability from zero to the incident neutron energies.

The maximum ε for protons crossing the gas cavity was the maximum value of ε for protons of all possible initial energies calculated using Equation B.2. The maximum ε of protons for $d = 3$ μm was determined to be from the slowing down of protons with an initial energy of 265 keV. For $d = 1$ μm, the maximum ε was from protons with an initial energy of 137 keV. The range of possible proton energies from the neutron interactions with the wall encompasses these energies. For protons traveling through propane-based TE gas, the maximum ε for $d = 3$ μm is 251.6 keV, and the maximum ε for $d = 1$ μm is 96.8 keV.

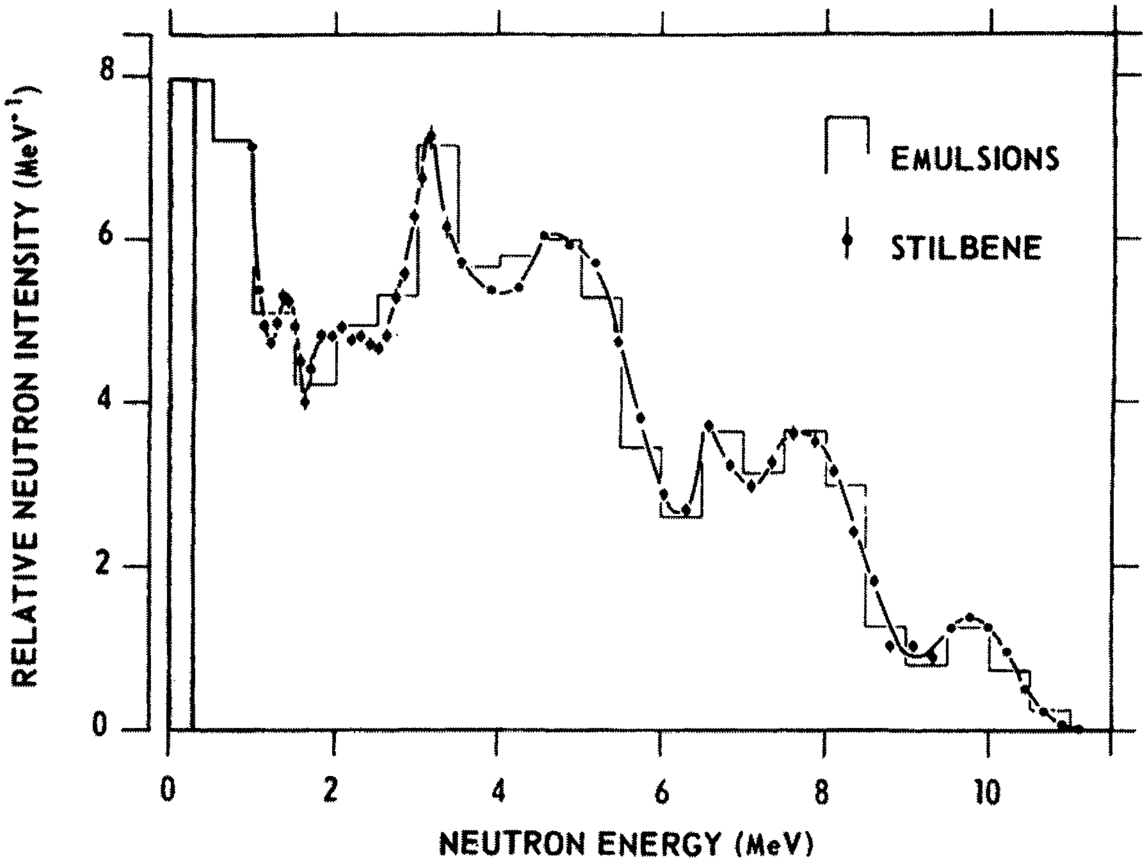

Fig. B.4. Neutron energy distribution of a plutonium-beryllium source containing 80 g of plutonium (from Anderson and Neff, 1972). The curve is a smooth curve through the data points obtained with a single crystal, fast neutron stilbene spectrometer. A nuclear emulsions spectrum is also shown.

Calibration Regression

Table B.1 summarizes the energy deposition and MCA channel numbers for all of the calibration points for $d = 1$ μm and a gain on the shaping amplifiers of ×2.5. For each

TABLE B.1

Data used for the calibration regression for a simulated diameter of 1 μm and a gain of x2.5 for the low gain and high gain shaping amplifiers.

Calibration Point	D (μm)	ε (keV)	MCA Channel	±, Weight
		low gain amplifier		
proton edge	1	95.8	111	3
half-crossing alpha peak	1	41.5	50.6	6
alpha peak	1	83	97	1
alpha edge	1	252	315	4
		high gain amplifier		
proton edge	1	95.8	107	3
half-crossing alpha peak	1	41.5	46.5	6
alpha peak	1	83	89	1
alpha edge	1	252	292	4

amplifier setting and simulated diameter, a weighted least squares estimation was determined using SAS for the coefficients, γ_0 and γ_1, of the regression,

$$\varepsilon = \gamma_0 + \gamma_1 \cdot Ch, \tag{B.3}$$

where Ch is the MCA channel number. Approximations were made for standard error in channel number, and the weights for ε shown in Table B.1 were used, with a smaller weight having more of an influence on the regression. Table B.2 lists the results. Fig.

B.5 displays the results along with the calibration points. The slopes, γ_1, of resulting regressions were tested for equivalence with an independent samples modified t-test (Satterthwaite's method). This test had an extremely small p-value, demonstrating that the slopes of the regressions for the two shaping amplifiers were not significantly different.

TABLE B.2

Coefficients of the weighted least squares regression of ε (keV) versus MCA channel number for both shaping amplifiers.

Coefficient	Value
low gain amplifier	
γ_0	7.6
γ_1	0.788
high gain amplifier	
γ_0	8.7
γ_1	0.85

This regression may be approximated for each amplifier by using one calibration point and extrapolating to the origin. The easiest calibration point to obtain for the particular TEPC used in this study is the alpha peak from alpha particles emitted by the internal alpha source.

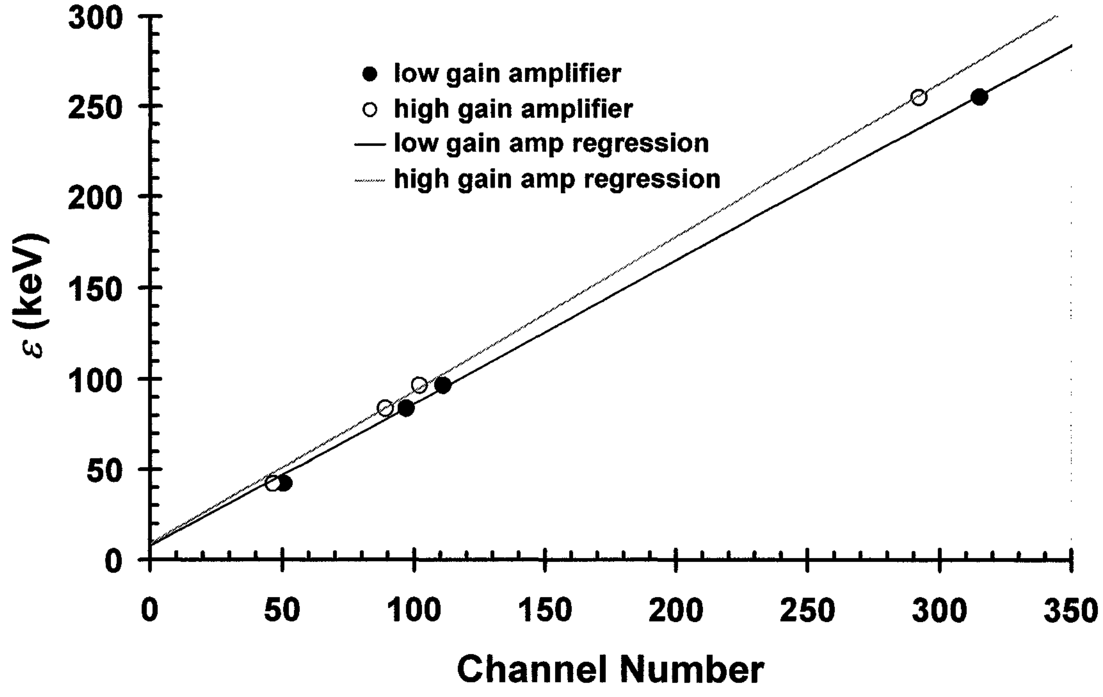

Fig. B.5. Calibration points for the low gain (solid circles) and high gain (open circles) TEPC shaping amplifiers shown with the results of a weighted least squares linear regression (black and gray lines, respectively) for energy deposited versus channel number on the multichannel analyzer.

APPENDIX C: STOPPING POWER CALCULATION

The following set of code, "bbwin," was used to calculate the mass electronic stopping power of the 1-μm and 3-μm diameter sphere of simulated tissue for HZE ions. For calculations in this paper, *LET* is assumed to be equal to the product of the mass electronic stopping power, $\frac{S}{\rho}$, and the density of the target, ρ:

$$LET(\text{keV }\mu\text{m}^{-1}) \approx \left(\frac{S}{\rho}\right)(\text{MeV cm}^2\text{ g}^{-1})\cdot \rho(\text{g cm}^{-3})\cdot 0.1\frac{\text{keV }\mu\text{m}^{-1}}{\text{MeV cm}^{-1}}, \tag{C.1}$$

neglecting the nuclear component of the mass stopping power.

This program is useful in calculating β, *LET*, and $\frac{S}{\rho}$ for ions (not electrons) incident upon a target and the energy, β, and *LET* of ions leaving a target (Fig. C.1). Also included in the result of the code is the energy transferred from the incident ion, calculated using 10,000 iterations of energy deposition through the entire path of the incident ion. Targets included as options in the program are all elements from $Z = 1$ to $Z = 98$, all compounds listed in Table 1.2 of ICRU Report 49 (Fig. C.2) (ICRU, 1984; ICRU, 1993), and custom targets.

This code is based primarily on information obtained from ICRU Report 49 (ICRU, 1993), including the target material constants. Bragg's rule from ICRU 37

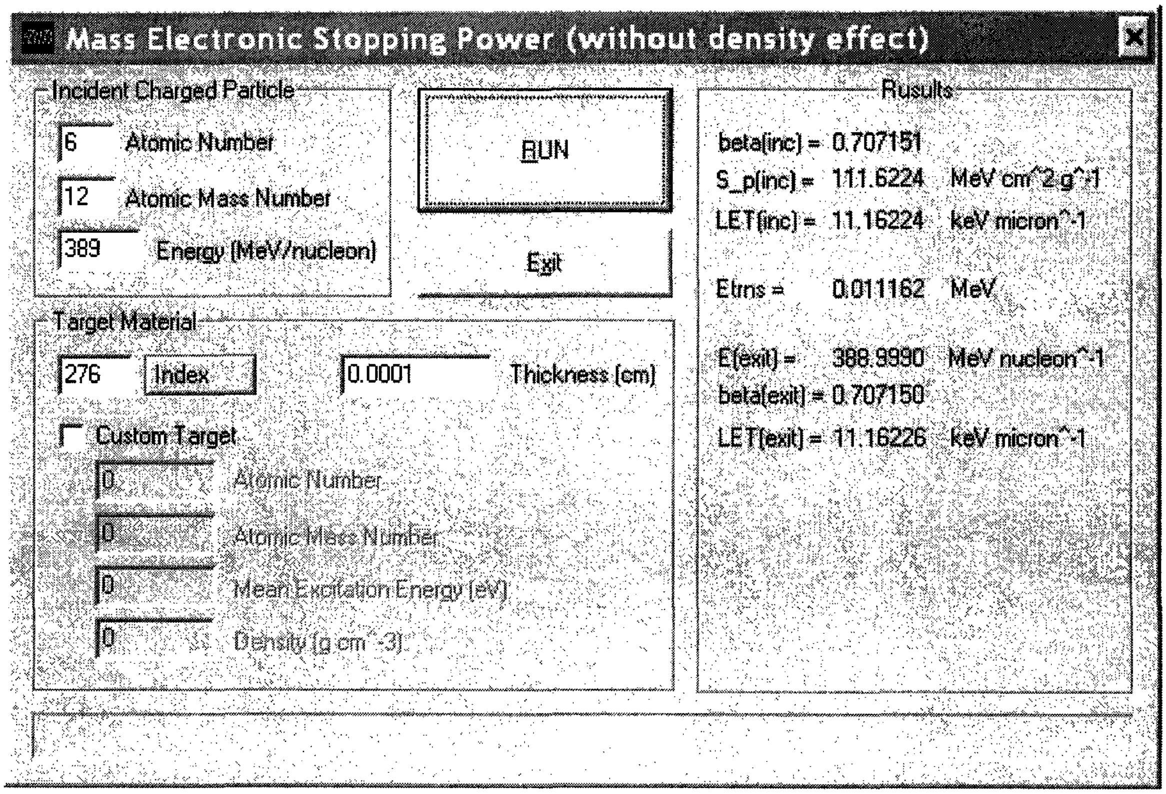

6 Atomic Number
12 Atomic Mass Number
389 Energy (MeV/nucleon)

276 Index
0.0001 Thickness (cm)

☐ Custom Target
0 Atomic Number
0 Atomic Mass Number
0 Mean Excitation Energy (eV)
0 Density (g cm^-3)

```
beta(inc) =  0.707151
S_p(inc) =   111.6224   MeV cm^2 g^-1
LET(inc) =   11.16224   keV micron^-1

Etrns =      0.011162   MeV

E(exit) =    388.9990   MeV nucleon^-1
beta(exit) = 0.707150
LET(exit) =  11.16226   keV micron^-1
```

Fig. C.1. Screen shot of bbwin graphical user interface. Results calculated in this example are for ^{12}C at 389 MeV nucleon^{-1} in 1-μm-thick liquid water.

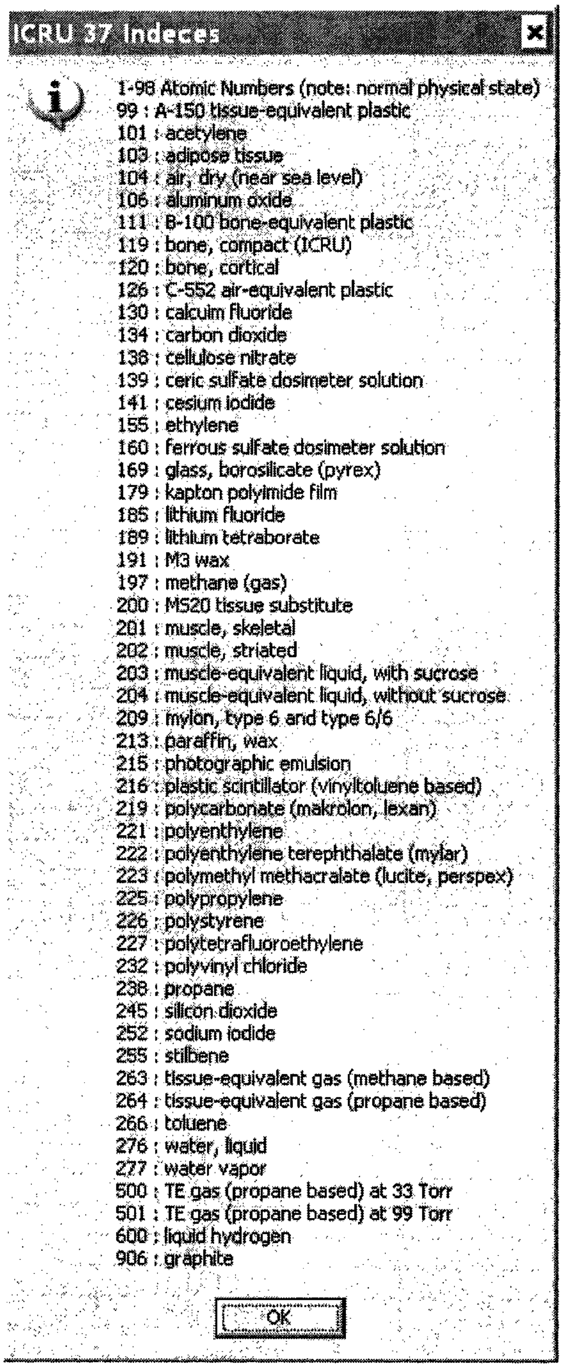

1-98 Atomic Numbers (note: normal physical state)
99 : A-150 tissue-equivalent plastic
101 : acetylene
103 : adipose tissue
104 : air, dry (near sea level)
106 : aluminum oxide
111 : B-100 bone-equivalent plastic
119 : bone, compact (ICRU)
120 : bone, cortical
126 : C-552 air-equivalent plastic
130 : calcuim fluoride
134 : carbon dioxide
138 : cellulose nitrate
139 : ceric sulfate dosimeter solution
141 : cesium iodide
155 : ethylene
160 : ferrous sulfate dosimeter solution
169 : glass, borosilicate (pyrex)
179 : kapton polyimide film
185 : lithium fluoride
189 : lithium tetraborate
191 : M3 wax
197 : methane (gas)
200 : MS20 tissue substitute
201 : muscle, skeletal
202 : muscle, striated
203 : muscle-equivalent liquid, with sucrose
204 : muscle-equivalent liquid, without sucrose
209 : mylon, type 6 and type 6/6
213 : paraffin, wax
215 : photographic emulsion
216 : plastic scintillator (vinyltoluene based)
219 : polycarbonate (makrolon, lexan)
221 : polyenthylene
222 : polyenthylene terephthalate (mylar)
223 : polymethyl methacralate (lucite, perspex)
225 : polypropylene
226 : polystyrene
227 : polytetrafluoroethylene
232 : polyvinyl chloride
238 : propane
245 : silicon dioxide
252 : sodium iodide
255 : stilbene
263 : tissue-equivalent gas (methane based)
264 : tissue-equivalent gas (propane based)
266 : toluene
276 : water, liquid
277 : water vapor
500 : TE gas (propane based) at 33 Torr
501 : TE gas (propane based) at 99 Torr
600 : liquid hydrogen
906 : graphite

Fig. C.2. Screen shot of the indices supported by the bbwin program (ICRU, 1984; ICRU, 1993).

(ICRU, 1984) was implemented in calculating the stopping powers of mixtures and compounds. The shell corrections from Walske (Walske, 1952; Walske, 1956) were applied in this program. And finally, much aid was received from Bichsel (1963).

Not included in this code are the approximations necessary to estimate mass stopping power for low energy ions. Therefore, it should not be used for calculations with respect to ions less than 10 MeV nucleon^{-1} in energy. Another limitation of the code is that there is no inclusion of a density effect correction. Therefore, it should not be used for calculations with respect to very fast ions, or at least this limitation should be considered when obtaining the final result. Also not considered in this code is the nuclear stopping power. A final limitation of this code is that the target is considered infinitely wide and tall. Thus, *LET* and energy transferred is calculated, rather than energy deposited in the target.

Superfluous lines in the code for most targets were omitted (denoted "…"). The results of this program are meant to be first approximations. The author is not responsible for their misinterpretation. The "bbwin1Dlg.cpp" code below was compiled along with its supporting files to create a graphical user interface using Microsoft® Visual C++® 6.0. The executable program is available by contacting the author.

bbwin1Dlg.cpp

```
// bbwin1Dlg.cpp : implementation file
//

/////////////////////////////////////////////////////////////////////////////

#include "stdafx.h"
#include "bbwin1.h"
#include "bbwin1Dlg.h"
#include "math.h"
#include "string.h"
```

```
#ifdef _DEBUG
#define new DEBUG_NEW
#undef THIS_FILE
static char THIS_FILE[] = __FILE__;
#endif

/////////////////////////////////////////////////////////////////////////////
// CAboutDlg dialog used for App About

class CAboutDlg : public CDialog
{
public:
	CAboutDlg();

// Dialog Data
	//{{AFX_DATA(CAboutDlg)
	enum { IDD = IDD_ABOUTBOX };
	//}}AFX_DATA

	// ClassWizard generated virtual function overrides
	//{{AFX_VIRTUAL(CAboutDlg)
	protected:
	virtual void DoDataExchange(CDataExchange* pDX);    // DDX/DDV support
	//}}AFX_VIRTUAL

// Implementation
protected:
	//{{AFX_MSG(CAboutDlg)
	//}}AFX_MSG
	DECLARE_MESSAGE_MAP()
};

CAboutDlg::CAboutDlg() : CDialog(CAboutDlg::IDD)
{
	//{{AFX_DATA_INIT(CAboutDlg)
	//}}AFX_DATA_INIT
}

void CAboutDlg::DoDataExchange(CDataExchange* pDX)
{
	CDialog::DoDataExchange(pDX);
	//{{AFX_DATA_MAP(CAboutDlg)
	//}}AFX_DATA_MAP
}

BEGIN_MESSAGE_MAP(CAboutDlg, CDialog)
	//{{AFX_MSG_MAP(CAboutDlg)
		// No message handlers
	//}}AFX_MSG_MAP
END_MESSAGE_MAP()

/////////////////////////////////////////////////////////////////////////////
// CBbwin1Dlg dialog

CBbwin1Dlg::CBbwin1Dlg(CWnd* pParent /*=NULL*/)
```

```
	: CDialog(CBbwin1Dlg::IDD, pParent)
{
	//{{AFX_DATA_INIT(CBbwin1Dlg)
	m_dA = 0.0;
	m_dAmat = 0.0;
	m_dEin = 0.0;
	m_dIpot = 0.0;
	m_drho = 0.0;
	m_dthick = 0.0;
	m_dZ = 0.0;
	m_dZmat = 0.0;
	m_bChkcustom = FALSE;
	m_smessage = _T("");
	m_dbin = 0.0;
	m_dletin = 0.0;
	m_dspin = 0.0;
	m_dbout = 0.0;
	m_dEout = 0.0;
	m_Etrns = 0.0;
	m_dletout = 0.0;
	m_imat = 0;
	//}}AFX_DATA_INIT
	// Note that LoadIcon does not require a subsequent DestroyIcon in Win32
	m_hIcon = AfxGetApp()->LoadIcon(IDR_MAINFRAME);
}

void CBbwin1Dlg::DoDataExchange(CDataExchange* pDX)
{
	CDialog::DoDataExchange(pDX);
	//{{AFX_DATA_MAP(CBbwin1Dlg)
	DDX_Text(pDX, IDC_A, m_dA);
	DDX_Text(pDX, IDC_AMAT, m_dAmat);
	DDX_Text(pDX, IDC_EIN, m_dEin);
	DDX_Text(pDX, IDC_IPOT, m_dIpot);
	DDX_Text(pDX, IDC_RHO, m_drho);
	DDX_Text(pDX, IDC_THICK, m_dthick);
	DDX_Text(pDX, IDC_Z, m_dZ);
	DDX_Text(pDX, IDC_ZMAT, m_dZmat);
	DDX_Check(pDX, IDC_CHKCUSTOM, m_bChkcustom);
	DDX_Text(pDX, IDC_MESSAGE, m_smessage);
	DDX_Text(pDX, IDC_BIN, m_dbin);
	DDX_Text(pDX, IDC_LETIN, m_dletin);
	DDX_Text(pDX, IDC_SPIN, m_dspin);
	DDX_Text(pDX, IDC_BOUT, m_dbout);
	DDX_Text(pDX, IDC_EOUT, m_dEout);
	DDX_Text(pDX, IDC_ETRNS, m_Etrns);
	DDX_Text(pDX, IDC_LETOUT, m_dletout);
	DDX_Text(pDX, IDC_MAT, m_imat);
	//}}AFX_DATA_MAP
}

BEGIN_MESSAGE_MAP(CBbwin1Dlg, CDialog)
	//{{AFX_MSG_MAP(CBbwin1Dlg)
	ON_WM_SYSCOMMAND()
	ON_WM_PAINT()
	ON_WM_QUERYDRAGICON()
```

```
        ON_BN_CLICKED(IDC_CHKCUSTOM, OnChkcustom)
        ON_BN_CLICKED(ID_RUN, OnRun)
        ON_BN_CLICKED(IDC_INDECES, OnIndeces)
        //}}AFX_MSG_MAP
END_MESSAGE_MAP()

/////////////////////////////////////////////////////////////////////////////
// CBbwin1Dlg message handlers

BOOL CBbwin1Dlg::OnInitDialog()
{
        CDialog::OnInitDialog();

        // Add "About..." menu item to system menu.

        // IDM_ABOUTBOX must be in the system command range.
        ASSERT((IDM_ABOUTBOX & 0xFFF0) == IDM_ABOUTBOX);
        ASSERT(IDM_ABOUTBOX < 0xF000);

        CMenu* pSysMenu = GetSystemMenu(FALSE);
        if (pSysMenu != NULL)
        {
                CString strAboutMenu;
                strAboutMenu.LoadString(IDS_ABOUTBOX);
                if (!strAboutMenu.IsEmpty())
                {
                        pSysMenu->AppendMenu(MF_SEPARATOR);
                        pSysMenu->AppendMenu(MF_STRING, IDM_ABOUTBOX, strAboutMenu);
                }
        }

        // Set the icon for this dialog.  The framework does this automatically
        //  when the application's main window is not a dialog
        SetIcon(m_hIcon, TRUE);                 // Set big icon
        SetIcon(m_hIcon, FALSE);                // Set small icon

        // TODO: Add extra initialization here

        m_bChkcustom = FALSE;

        UpdateData(FALSE);

        return TRUE;  // return TRUE  unless you set the focus to a control
}

void CBbwin1Dlg::OnSysCommand(UINT nID, LPARAM lParam)
{
        if ((nID & 0xFFF0) == IDM_ABOUTBOX)
        {
                CAboutDlg dlgAbout;
                dlgAbout.DoModal();
        }
        else
        {
                CDialog::OnSysCommand(nID, lParam);
        }
```

```
}

// If you add a minimize button to your dialog, you will need the code below
//  to draw the icon.  For MFC applications using the document/view model,
//  this is automatically done for you by the framework.

void CBbwin1Dlg::OnPaint()
{
	if (IsIconic())
	{
		CPaintDC dc(this); // device context for painting

		SendMessage(WM_ICONERASEBKGND, (WPARAM) dc.GetSafeHdc(), 0);

		// Center icon in client rectangle
		int cxIcon = GetSystemMetrics(SM_CXICON);
		int cyIcon = GetSystemMetrics(SM_CYICON);
		CRect rect;
		GetClientRect(&rect);
		int x = (rect.Width() - cxIcon + 1) / 2;
		int y = (rect.Height() - cyIcon + 1) / 2;

		// Draw the icon
		dc.DrawIcon(x, y, m_hIcon);
	}
	else
	{
		CDialog::OnPaint();
	}
}

// The system calls this to obtain the cursor to display while the user drags
//  the minimized window.
HCURSOR CBbwin1Dlg::OnQueryDragIcon()
{
	return (HCURSOR) m_hIcon;
}

void CBbwin1Dlg::OnChkcustom()
{
	// TODO: Add your control notification handler code here

	UpdateData(TRUE);
	if (m_bChkcustom == TRUE) {
		GetDlgItem(IDC_ZMAT) ->EnableWindow(TRUE);
		GetDlgItem(IDC_AMAT) ->EnableWindow(TRUE);
		GetDlgItem(IDC_IPOT) ->EnableWindow(TRUE);
		GetDlgItem(IDC_RHO) ->EnableWindow(TRUE);
		GetDlgItem(IDC_TARGETZ) ->EnableWindow(TRUE);
		GetDlgItem(IDC_TARGETA) ->EnableWindow(TRUE);
		GetDlgItem(IDC_TARGETI) ->EnableWindow(TRUE);
		GetDlgItem(IDC_TARGETRHO) ->EnableWindow(TRUE);
		GetDlgItem(IDC_MAT) ->EnableWindow(FALSE);
		GetDlgItem(IDC_INDECES) ->EnableWindow(FALSE);
	}
	else {
```

```
        GetDlgItem(IDC_ZMAT) ->EnableWindow(FALSE);
        GetDlgItem(IDC_AMAT) ->EnableWindow(FALSE);
        GetDlgItem(IDC_IPOT) ->EnableWindow(FALSE);
        GetDlgItem(IDC_RHO) ->EnableWindow(FALSE);
        GetDlgItem(IDC_TARGETZ) ->EnableWindow(FALSE);
        GetDlgItem(IDC_TARGETA) ->EnableWindow(FALSE);
        GetDlgItem(IDC_TARGETI) ->EnableWindow(FALSE);
        GetDlgItem(IDC_TARGETRHO) ->EnableWindow(FALSE);
        GetDlgItem(IDC_MAT) ->EnableWindow(TRUE);
        GetDlgItem(IDC_INDECES) ->EnableWindow(TRUE);
    }
}

void CBbwin1Dlg::OnRun()
{
    // TODO: Add your control notification handler code here
    const double pi=3.14159, N0=6.02205e23, r0=2.81794e-13; //1/mol, cm
    const double mn=939.574, mp=938.281, me=0.511004; //MeV
    const double k0=8.98755e9, echarge=1.60218e-19, mkg=9.10939e-31, c=2.99792e8;
    const double bins=10000.;
    const int cnsttnts=13;
    int iint,jint,num,mat;
    double f_i[cnsttnts],Zmat_i[cnsttnts],Amat_i[cnsttnts],Ipot_i[cnsttnts],mstoppow_i[cnsttnts];
    double rho,Zmat,Amat,Ipot,thick,Z,A,Ein; //input parameters
    double Etrns; //output paramater: MeV
    double dx, dE, b, Etot, E, mc2; //calculation parameters
    double i;
    double mstoppow;
    double Ry, ZKeff, ZLeff, ZMeff, etaK, etaL, etaM, x, RK, SK, BK, P, Q, RL, SL, BL, KA;
//calculation parameters
    double CK, CL, CM, delta; //output parameters

    UpdateData(TRUE);

    iint=0;mstoppow=0.;i=0.;dx=0.;dE=0.;b=0.;Etot=0.;E=0.;mc2=0.;
    rho=0.;thick=0.;Ein=0.;Z=0.;A=0.;Etrns=0.;num=0;
    jint=0;
    while (jint<cnsttnts) {
        Zmat_i[jint]=0.;
        Amat_i[jint]=0.;
        f_i[jint]=0.;
        Ipot_i[jint]=0.;
        mstoppow_i[jint];
        jint++;
    }
    Ry=0.;ZKeff=0.;ZLeff=0.;ZMeff=0.;etaK=0.;etaL=0.;etaM=0.;x=0.;
    RK=0.;SK=0.;BK=0.;P=0.;Q=0.;RL=0.;SL=0.;BL=0.;KA=0.;
    CK=0.;CL=0.;CM=0.;delta=0.;
    m_smessage = "";

    UpdateData(FALSE);

//Use input parameters
    Z = m_dZ;
    A = m_dA;
    Ein = m_dEin;
```

```
        mat = m_imat;
        thick = m_dthick;
        if (m_bChkcustom) {
                mat = 0;
                num = 1;
                Zmat_i[0] = m_dZmat;
                Amat_i[0] = m_dAmat;
                Ipot_i[0] = m_dIpot;
                f_i[0] = 1.;
                rho = m_drho;
        }

//Determining constants for the material
        if (mat == 1) {
                num = 1;
                Zmat_i[0] = 1.;
                Amat_i[0] = 1.0079;
                Ipot_i[0] = 19.2;
                f_i[0] = 1.;
                rho  = 8.3748e-5;
        }
        else if (mat == 2) {

                num = 1;
                Zmat_i[0] = 2.;
                Amat_i[0] = 4.0026;
                Ipot_i[0] = 41.8;
                f_i[0] = 1.;
                rho  = 1.6632e-4;
        }

                                                • • •
        else if (mat == 98) {

                num = 1;
                Zmat_i[0] = 98.;
                Amat_i[0] = 251.;
                Ipot_i[0] = 966.;
                f_i[0] = 1.;
                rho  = 14.; //estimate!!
        }
        if (mat <= 98) ;
        else if (mat == 99) {

                num = 6;
                Zmat_i[0] = 1.;
                Amat_i[0] = 1.0079;
                Ipot_i[0] = 19.2;
                f_i[0] = 0.101327;
                Zmat_i[1] = 6.;
                Amat_i[1] = 12.011;
                Ipot_i[1] = 78.;
                f_i[1] = 0.775501;
                Zmat_i[2] = 7.;
                Amat_i[2] = 14.0067;
```

```
                Ipot_i[2] = 82.;
                f_i[2] = 0.035057;
                Zmat_i[3] = 8.;
                Amat_i[3] = 15.9994;
                Ipot_i[3] = 95.;
                f_i[3] = 0.052316;
                Zmat_i[4] = 9.;
                Amat_i[4] = 18.998403;
                Ipot_i[4] = 115.;
                f_i[4] = 0.017422;
                Zmat_i[5] = 20.;
                Amat_i[5] = 40.08;
                Ipot_i[5] = 191.;
                f_i[5] = 0.018378;
                rho  = 1.1270; //g/cm^3
        }
```

• • •

```
        else if (mat == 906) {

                num = 1;
                Zmat_i[0] = 6.;
                Amat_i[0] = 12.011;
                Ipot_i[0] = 78.;
                f_i[0] = 1.;
                rho  = 1.7;
        }

//Calculations
        dx = thick/bins; //cm
        E = Ein;
        mc2 = (A-Z)*mn + Z*mp; //mass of incident particle in MeV
        while (i<bins) {
                jint = 0;
                if (i/100. == int(i/100.)) UpdateData(FALSE);
                while (jint < num) {
                        Zmat = Zmat_i[jint];
                        Amat = Amat_i[jint];
                        Ipot = Ipot_i[jint];
                        iint=0;
                        Etot = (A-Z)*(E+mn) + Z*(E+mp);
                        b = sqrt((Etot*Etot-mc2*mc2)/(Etot*Etot));

                //Shell Correction Calculations
                        Ry = 13.6e-6;//MeV
                        ZKeff = Zmat - 0.3;
                        ZLeff = Zmat - 4.15;
                        ZMeff = Zmat - 14.;
                        etaK = me/(2*Ry*ZKeff*ZKeff)*b*b/(1-b*b);
                        etaL = me/(2*Ry*ZLeff*ZLeff)*b*b/(1-b*b);
                        etaM = me/(2*Ry*ZMeff*ZMeff)*b*b/(1-b*b);
                //K-shell
                        x=1/etaK;
                        if (etaK >= 5.) {
                                CK = 1.22e-4*Zmat*Zmat*(1-b*b)/(b*b);
```

```
                        }
                        else if (etaK < 5. && etaK >= 0.5) {
                                if (Zmat <= 21.5)               CK = -0.1978*x*x*x*x + 1.2545*x*x*x
- 3.0704*x*x + 3.037*x - 0.0457;
                                else if (Zmat > 21.5 && Zmat <= 66.) CK = -0.2033*x*x*x*x +
1.2836*x*x*x - 3.1219*x*x + 3.1163*x - 0.0493;
                                else                    CK = -0.1994*x*x*x*x + 1.2538*x*x*x -
3.0559*x*x + 3.0809*x - 0.0368;
                        }
                        else {
                                RK = -5.8441e-7*Zmat*Zmat*Zmat + 0.0001501*Zmat*Zmat -
0.01274*Zmat + 1.9223;
                                SK = -3.5706e-7*Zmat*Zmat*Zmat + 0.00009456*Zmat*Zmat -
0.008643*Zmat + 2.5397;
                                if (Zmat <= 21.5)               BK = -3.3411*etaK*etaK*etaK +
4.4452*etaK*etaK - 0.2293*etaK - 0.001329;
                                else if (Zmat > 21.5 && Zmat <= 66.) BK = -2.3932*etaK*etaK*etaK
+ 3.6737*etaK*etaK - 0.2616*etaK + 0.001678;
                                else                    BK = -0.3730*etaK*etaK*etaK +
2.1818*etaK*etaK - 0.1207*etaK - 0.0002797;
                                if (BK < 0) BK=0;
                                CK = RK*log(etaK) + SK - BK;
                        }
                //L-shell
                        x=1/etaL;
                        if (etaL >=3) {
                                P = 2.838e-6*Zmat*Zmat*Zmat - 0.0007292*Zmat*Zmat +
0.05798*Zmat + 0.6449;
                                CL = P*x + 1.5*x*x - 4.0*x*x*x + 4.4*x*x*x*x;
                        }
                        else if (etaL < 3 && etaL >= 0.7) {
                                Q = 2.704e-6*Zmat*Zmat*Zmat - 0.0006958*Zmat*Zmat +
0.05542*Zmat + 0.8811;
                                CL = Q*x;
                        }
                        else {
                                RL = 4.7132e-7*Zmat*Zmat*Zmat*Zmat - 1.4767e-
4*Zmat*Zmat*Zmat + 0.01651*Zmat*Zmat - 0.7879*Zmat + 20.2980;
                                SL = 5.9323e-7*Zmat*Zmat*Zmat*Zmat - 1.9148e-
4*Zmat*Zmat*Zmat + 0.02252*Zmat*Zmat - 1.1704*Zmat + 43.9810;
                                if (Zmat <= 25.)                BL = -8.7076*etaL*etaL*etaL -
19.205*etaL*etaL + 49.817*etaL - 0.3814;
                                else if (Zmat > 25. && Zmat <= 37.5)  BL = -12.954*etaL*etaL*etaL -
8.1364*etaL*etaL + 39.949*etaL - 0.3758;
                                else if (Zmat > 37.5 && Zmat <= 72.5) BL = -16.681*etaL*etaL*etaL
- 1.5168*etaL*etaL + 33.112*etaL - 0.3647;
                                else                    BL = -25.443*etaL*etaL*etaL +
10.027*etaL*etaL + 27.209*etaL - 0.525;
                                if (BL < 0) BL=0;
                                CL = RL*log(etaL) + SL - BL;
                        }
                //M-shell
                        if (etaM > 0.3) {
                                KA = 1.6;
                                CM = KA*1e-4*(Zmat-14)*(Zmat-14)*(1.-b*b)/(b*b);
                        }
```

```
                        else {
                                CM = 0;
                        }

                //Calculate Mass Stopping Power in MeV*cm^2/g
                        delta = 0.;  //density effect is neglected in this version
                        mstoppow_i[jint] =
4.*pi*r0*r0*me*N0*Zmat/Amat*Z*Z/(b*b)*(log(2.*me*1000000.*b*b/(Ipot*(1.-b*b)))-b*b-
(CK+CL+CM)/Zmat-delta);
                        jint++;
                }
                jint = 0;
                mstoppow = 0.;
                while (jint < num) {
                        mstoppow = mstoppow + mstoppow_i[jint] * f_i[jint];
                        jint++;
                }
                if (i == 0) {
                        m_dbin = b;
                        m_dspin = mstoppow;
                        m_dletin = mstoppow*rho/10.;
                }
                dE = dx * mstoppow * rho;
                Etrns = dE + Etrns;
                E = (E*A - dE)/A; // assumed that energy deposited is equal to Kinetic Energy loss
                if (mstoppow <= 0.) {
                        m_smessage = "Note: At this depth into the target the energy of the charged
particle fell out of the range of this program.";
                        mstoppow = 0.;
                        Etrns = Ein*A;
                        E = 0.;
                        b = 0.;
                        break;
                }
                if (Etrns >= Ein*A) {
                        Etrns = Ein*A;
                        E=0.;
                        b=0.;
                        break;
                }
                i++;
        }

//output results
        m_Etrns = Etrns;
        if (E != 0) {
                m_dEout = E;
                m_dbout = b;
                m_dletout = mstoppow*rho/10.;
        }
        else m_smessage = "**The particle stopped in the material**";

        UpdateData(FALSE);
}

void CBbwin1Dlg::OnIndeces()
```

```
{
	// TODO: Add your control notification handler code here
	CString indeces;
	indeces = "1-98 Atomic Numbers (note: normal physical state)\n99 : A-150 tissue-equivalent
plastic\n101 : acetylene\n103 : adipose tissue\n104 : air, dry (near sea level)\n106 : aluminum oxide\n111 :
B-100 bone-equivalent plastic\n119 : bone, compact (ICRU)\n120 : bone, cortical\n126 : C-552 air-
equivalent plastic\n130 : calcuim fluoride\n134 : carbon dioxide\n138 : cellulose nitrate\n139 : ceric sulfate
dosimeter solution\n141 : cesium iodide\n155 : ethylene\n160 : ferrous sulfate dosimeter solution\n169 :
glass, borosilicate (pyrex)\n179 : kapton polyimide film\n185 : lithium fluoride\n189 : lithium
tetraborate\n191 : M3 wax\n197 : methane (gas)\n200 : MS20 tissue substitute\n201 : muscle, skeletal\n202
: muscle, striated\n203 : muscle-equivalent liquid, with sucrose\n204 : muscle-equivalent liquid, without
sucrose\n209 : mylon, type 6 and type 6/6\n213 : paraffin, wax\n215 : photographic emulsion\n216 : plastic
scintillator (vinyltoluene based)\n219 : polycarbonate (makrolon, lexan)\n221 : polyenthylene\n222 :
polyenthylene terephthalate (mylar)\n223 : polymethyl methacralate (lucite, perspex)\n225 :
polypropylene\n226 : polystyrene\n227 : polytetrafluoroethylene\n232 : polyvinyl chloride\n238 :
propane\n245 : silicon dioxide\n252 : sodium iodide\n255 : stilbene\n263 : tissue-equivalent gas (methane
based)\n264 : tissue-equivalent gas (propane based)\n266 : toluene\n276 : water, liquid\n277 : water
vapor\n500 : TE gas (propane based) at 33 Torr\n501 : TE gas (propane based) at 99 Torr\n600 : liquid
hydrogen\n906 : graphite";
	MessageBox(indeces,"ICRU 37 Indeces",MB_ICONINFORMATION);
}
```

bbwin1Dlg.h

```
// bbwin1Dlg.h : header file
//

#if !defined(AFX_BBWIN1DLG_H__20735C59_4BF3_4FAA_8077_12FA850C5A20__INCLUDED_)
#define AFX_BBWIN1DLG_H__20735C59_4BF3_4FAA_8077_12FA850C5A20__INCLUDED_

#if _MSC_VER > 1000
#pragma once
#endif // _MSC_VER > 1000

/////////////////////////////////////////////////////////////////////////////
// CBbwin1Dlg dialog

class CBbwin1Dlg : public CDialog
{
// Construction
public:
	CBbwin1Dlg(CWnd* pParent = NULL);	// standard constructor

// Dialog Data
	//{{AFX_DATA(CBbwin1Dlg)
	enum { IDD = IDD_BBWIN1_DIALOG };
	double	m_dA;
	double	m_dAmat;
	double	m_dEin;
	double	m_dIpot;
	double	m_drho;
	double	m_dthick;
	double	m_dZ;
	double	m_dZmat;
```

```
	BOOL	m_bChkcustom;
	CString	m_smessage;
	double	m_dbin;
	double	m_dletin;
	double	m_dspin;
	double	m_dbout;
	double	m_dEout;
	double	m_Etrns;
	double	m_dletout;
	int			m_imat;
	//}}AFX_DATA

	// ClassWizard generated virtual function overrides
	//{{AFX_VIRTUAL(CBbwin1Dlg)
	protected:
	virtual void DoDataExchange(CDataExchange* pDX);	// DDX/DDV support
	//}}AFX_VIRTUAL

// Implementation
protected:
	HICON m_hIcon;

	// Generated message map functions
	//{{AFX_MSG(CBbwin1Dlg)
	virtual BOOL OnInitDialog();
	afx_msg void OnSysCommand(UINT nID, LPARAM lParam);
	afx_msg void OnPaint();
	afx_msg HCURSOR OnQueryDragIcon();
	afx_msg void OnChkcustom();
	afx_msg void OnRun();
	afx_msg void OnIndeces();
	//}}AFX_MSG
	DECLARE_MESSAGE_MAP()
};

//{{AFX_INSERT_LOCATION}}
// Microsoft Visual C++ will insert additional declarations immediately before the previous line.

#endif //
!defined(AFX_BBWIN1DLG_H__20735C59_4BF3_4FAA_8077_12FA850C5A20__INCLUDED_)
```

APPENDIX D: STOPPING POWER MULTIPLE CALCULATION

The following set of code, "bb_multi," was adapted from bbwin (see Appendix C: Stopping Power Calculation) to automatically include calculations related to mass electronic stopping power of several successive targets. This code was primarily used to calculate the energy of HZE ions in this study at the upstream side of the TEPC immediately before entering the gas cavity and after traveling through all upstream detectors and the TEPC components.

The program requires an input file, "infile.txt," in the following format:

first line: Z A E
second line: index_1 thick_1
third line: index_2 thick_2
fourth line: index_3 thick_3
...
last line: index_*n* thick_*n*

where Z is the atomic number, A is the atomic mass in amu, and E is the energy in MeV nucleon^{-1} of the incident ion, index_*i* is the ICRU ID Number (Fig. C.2) (ICRU, 1984; ICRU, 1993), and thick_*i* is the thickness in cm of the i^{th} of *n* targets. This input file must placed in the same directory as the code's executable, "bb_multi.exe." An example of infile.txt is given in Fig. D.1. The resulting output file, "outfile.txt," corresponding to this input file is shown in Fig. D.2. The output file is written in the same directory as the

```
1 1 200
276 1
276 20
82 3
73 5
```

Fig. D.1. An example of an input file "infile.txt" to be used with the bb_multi program. In this example, an incident 200-MeV proton successively passes through 1 cm of liquid water, 20 cm of liquid water, and 3 cm of lead.

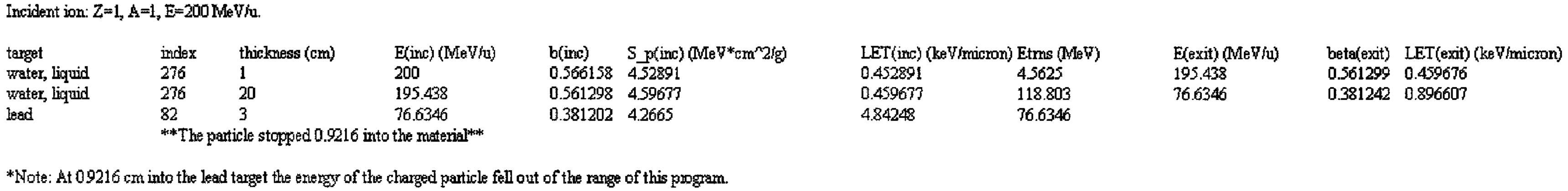

```
Incident ion: Z=1, A=1, E=200 MeV/u.

target          index   thickness (cm)   E(inc) (MeV/u)   b(inc)     S_p(inc) (MeV*cm^2/g)   LET(inc) (keV/micron) Etrns (MeV)   E(exit) (MeV/u)   beta(exit)  LET(exit) (keV/micron)
water, liquid   276     1                200              0.566158   4.52891                 0.452891              4.5625        195.438           0.561299    0.459676
water, liquid   276     20               195.438          0.561298   4.59677                 0.459677              118.803       76.6346           0.381242    0.896607
lead            82      3                76.6346          0.381202   4.2665                  4.84248               76.6346
                **The particle stopped 0.9216 into the material**

*Note: At 0.9216 cm into the lead target the energy of the charged particle fell out of the range of this program.
```

Fig. D.2. The results of the bb_multi program written in the output file “outfile.txt” using the input file in Fig. D.1. In this example, the incident proton was slowed to 195 MeV after 1 cm of liquid water, was slowed to 77 MeV after an additional 20 cm of liquid water, and stopped about 1 cm into the following lead target.

code's executable, "bb_multi.exe," and may be easily copied and pasted into a spreadsheet program.

This code is based primarily on information obtained from ICRU Report 49 (ICRU, 1993), including the target material constants. Bragg's rule from ICRU 37 (ICRU, 1984) was implemented in calculating the stopping powers of mixtures and compounds. The shell corrections from Walske (Walske, 1952; Walske, 1956) was applied in this program. And finally, much aid was received from Bichsel (1963).

Superfluous lines in the code for most targets were omitted (denoted "…"). This code has the same limitations as bbwin (see Appendix C: Stopping Power Calculation). In addition, the executable program does not support custom targets. The results of this program are meant to be first approximations. The author is not responsible for their misinterpretation. The "bb_multi.cpp" code below and its supporting files were compiled using Microsoft® Visual C++® 6.0. The executable program is available by contacting the author.

bb_multi.cpp

```
// bb_multi.cpp : Defines the entry point for the console application.
//

//MASS ELECTRONIC STOPPING POWER
//
//Note:  For density of H (not H2), rho should be cut in half

#include "stdafx.h"
#include "stdlib.h"
#include "iostream.h"
#include "stdio.h"
#include "math.h"
#include "string.h"
#include "fstream.h"

int main(int argc, char* argv[])
{
```

```
ifstream infile;
ofstream outfile;
const double pi=3.14159, N0=6.02205e23, r0=2.81794e-13; //1/mol, cm
const double mn=939.574, mp=938.281, me=0.511004; //MeV
const double k0=8.98755e9, echarge=1.60218e-19, mkg=9.10939e-31, c=2.99792e8;
const double bins=10000.;
const int cnsttnts=13;
int iint,jint,mat,num;
char matname[50];
double f_i[cnsttnts],Zmat_i[cnsttnts],Amat_i[cnsttnts],Ipot_i[cnsttnts],mstoppow_i[cnsttnts];
double rho,Zmat,Amat,Ipot,thick,Z,A,Ein; //input parameters
double Etrns; //output paramater: MeV
double dx, dE, b, Etot, E, mc2; //calculation parameters
double i;
double mstoppow;
double Ry, ZKeff, ZLeff, ZMeff, etaK, etaL, etaM, x, RK, SK, BK, P, Q, RL, SL, BL, KA; //calculation
parameters
double CK, CL, CM, delta; //output parameters
/*****************************************************************
mat      = target material index number
rho      = target density (gases for 20 C and 1 atm)
f[]      = fraction by weight of each constituent
Zmat[]   = target atomic number
Amat[]   = target atomic mass
Ipot[]   = target ionization potential, *mean excitation energy*
thick    = target thickness
Z        = CP atomic number
A        = CP atomic mass
Ein      = CP kinetic energy in MeV/nucleon
Etrns    = energy transfered to target
dx       = stepping distance traveled in target
dE       = energy transferred in dx in MeV
b        = CP speed relative to the speed of light in a vacuum
Etot     = CP total energy
E        = CP kinetic energy in MeV
mc2      = CP mass in MeV
ins      = iterations in calculating stopping
i        = step number
mstoppow = mass stopping power of target with CP of Ein
*****************************************************************/

//Initializing values
        Ein=0.;Z=0.;A=0.;

//Explain...
        cout << "MASS ELECTRONIC STOPPING POWER" << endl << endl;
        cout << "\nThe text file 'infile.txt' should have the below format and should be in the bb_multi.exe
directory.";
        cout << "\n\n\tZ A(amu) E(MeV/n)"
    << "\n\tindex thickness(cm)"
    << "\n\tindex thickness(cm)"
    << "\n\t..." << endl;

        infile.open("infile.txt");
        outfile.open("outfile.txt");
        if (infile.fail()) {
```

```
        cout << "\n****The input file does not exist.  Save it as infile.txt in the bb program
directory, and run the program again.****" << endl;
        exit(1);
    }

    infile >> Z >> A >> Ein;

    outfile << "Incident ion: Z=" << Z << ", A=" << A << ", E=" << Ein << " MeV/n." << endl;
    outfile << "\ntarget\tindex\tthickness (cm)\tE(inc) (MeV/n)\tb(inc)\tS_p(inc)
(MeV*cm^2/g)\tLET(inc) (keV/micron)\tEtrns (MeV)\tE(exit) (MeV/n)\tbeta(exit)\tLET(exit)
(keV/micron)";

while (!infile.eof()) {
//Initializing values
    iint=0;mstoppow=0.;i=0.;dx=0.;dE=0.;b=0.;Etot=0.;E=0.;mc2=0.;
    rho=0.;thick=0.;Etrns=0.;num=0;mat=0;

    infile >> mat >> thick;

//Determining constants for the material
    if (mat == 1) {
        strcpy(matname,"H2 (gas)");
        num = 1;
        Zmat_i[0] = 1.;
        Amat_i[0] = 1.0079;
        Ipot_i[0] = 19.2;
        f_i[0] = 1.;
        rho  = 8.3748e-5;
    }
    else if (mat == 2) {
        strcpy(matname,"He (gas)");
        num = 1;
        Zmat_i[0] = 2.;
        Amat_i[0] = 4.0026;
        Ipot_i[0] = 41.8;
        f_i[0] = 1.;
        rho  = 1.6632e-4;
    }

                                • • •
    else if (mat == 98) {
        strcpy(matname,"californium");
        num = 1;
        Zmat_i[0] = 98.;
        Amat_i[0] = 251.;
        Ipot_i[0] = 966.;
        f_i[0] = 1.;
        rho  = 14.; //estimate!!
    }
    if (mat <= 98) ;
    else if (mat == 99) {
        strcpy(matname,"A-150 tissue-equivalent plastic");
        num = 6;
        Zmat_i[0] = 1.;
        Amat_i[0] = 1.0079;
```

```
        Ipot_i[0] = 19.2;
        f_i[0] = 0.101327;
        Zmat_i[1] = 6.;
        Amat_i[1] = 12.011;
        Ipot_i[1] = 78.;
        f_i[1] = 0.775501;
        Zmat_i[2] = 7.;
        Amat_i[2] = 14.0067;
        Ipot_i[2] = 82.;
        f_i[2] = 0.035057;
        Zmat_i[3] = 8.;
        Amat_i[3] = 15.9994;
        Ipot_i[3] = 95.;
        f_i[3] = 0.052316;
        Zmat_i[4] = 9.;
        Amat_i[4] = 18.998403;
        Ipot_i[4] = 115.;
        f_i[4] = 0.017422;
        Zmat_i[5] = 20.;
        Amat_i[5] = 40.08;
        Ipot_i[5] = 191.;
        f_i[5] = 0.018378;
        rho  = 1.1270; //g/cm^3
    }

                        • • •
    else if (mat == 906) {
        strcpy(matname,"carbon - graphite");
        num = 1;
        Zmat_i[0] = 6.;
        Amat_i[0] = 12.011;
        Ipot_i[0] = 78.;
        f_i[0] = 1.;
        rho  = 1.7;
    }
    else {
        if (mat) {
            cout << "The targetmaterial " << mat << " that was chosen is not included in this
program." << endl;
            outfile << "\n\t\t[[The target material that was chosen next is not included in this
program.]]";
            outfile << "\n\t\t[[Please either add a target to the source file and compile or use
a similar target material substitute.]]";
        }
        outfile << endl;
        infile.close();
        outfile.close();
        exit(1);
    }

//Calculations
    dx = thick/bins; //cm
    E = Ein;
    mc2 = (A-Z)*mn + Z*mp; //mass of incident particle in MeV
    while (i<bins) {
```

```
                jint = 0;
                while (jint < num) {
                        Zmat = Zmat_i[jint];
                        Amat = Amat_i[jint];
                        Ipot = Ipot_i[jint];
                        iint=0;
                        Etot = (A-Z)*(E+mn) + Z*(E+mp);
                        b = sqrt((Etot*Etot-mc2*mc2)/(Etot*Etot));

                //Shell Correction Calculations
                        Ry = 13.6e-6;//MeV
                        ZKeff = Zmat - 0.3;
                        ZLeff = Zmat - 4.15;
                        ZMeff = Zmat - 14.;
                        etaK = me/(2*Ry*ZKeff*ZKeff)*b*b/(1-b*b);
                        etaL = me/(2*Ry*ZLeff*ZLeff)*b*b/(1-b*b);
                        etaM = me/(2*Ry*ZMeff*ZMeff)*b*b/(1-b*b);
                //K-shell
                        x=1/etaK;
                        if (etaK >= 5.) {
                                CK = 1.22e-4*Zmat*Zmat*(1-b*b)/(b*b);
                        }
                        else if (etaK < 5. && etaK >= 0.5) {
                                if (Zmat <= 21.5)               CK = -0.1978*x*x*x*x + 1.2545*x*x*x
- 3.0704*x*x + 3.037*x - 0.0457;
                                else if (Zmat > 21.5 && Zmat <= 66.) CK = -0.2033*x*x*x*x +
1.2836*x*x*x - 3.1219*x*x + 3.1163*x - 0.0493;
                                else                    CK = -0.1994*x*x*x*x + 1.2538*x*x*x -
3.0559*x*x + 3.0809*x - 0.0368;
                        }
                        else {
                                RK = -5.8441e-7*Zmat*Zmat*Zmat + 0.0001501*Zmat*Zmat -
0.01274*Zmat + 1.9223;
                                SK = -3.5706e-7*Zmat*Zmat*Zmat + 0.00009456*Zmat*Zmat -
0.008643*Zmat + 2.5397;
                                if (Zmat <= 21.5)               BK = -3.3411*etaK*etaK*etaK +
4.4452*etaK*etaK - 0.2293*etaK - 0.001329;
                                else if (Zmat > 21.5 && Zmat <= 66.) BK = -2.3932*etaK*etaK*etaK
+ 3.6737*etaK*etaK - 0.2616*etaK + 0.001678;
                                else                    BK = -0.3730*etaK*etaK*etaK +
2.1818*etaK*etaK - 0.1207*etaK - 0.0002797;
                                if (BK < 0) BK=0;
                                CK = RK*log(etaK) + SK - BK;
                        }
                //L-shell
                        x=1/etaL;
                        if (etaL >=3) {
                                P = 2.838e-6*Zmat*Zmat*Zmat - 0.0007292*Zmat*Zmat +
0.05798*Zmat + 0.6449;
                                CL = P*x + 1.5*x*x - 4.0*x*x*x + 4.4*x*x*x*x;
                        }
                        else if (etaL < 3 && etaL >= 0.7) {
                                Q = 2.704e-6*Zmat*Zmat*Zmat - 0.0006958*Zmat*Zmat +
0.05542*Zmat + 0.8811;
                                CL = Q*x;
                        }
```

```
            else {
                RL = 4.7132e-7*Zmat*Zmat*Zmat*Zmat - 1.4767e-
4*Zmat*Zmat*Zmat + 0.01651*Zmat*Zmat - 0.7879*Zmat + 20.2980;
                SL = 5.9323e-7*Zmat*Zmat*Zmat*Zmat - 1.9148e-
4*Zmat*Zmat*Zmat + 0.02252*Zmat*Zmat - 1.1704*Zmat + 43.9810;
                if (Zmat <= 25.)            BL = -8.7076*etaL*etaL*etaL -
19.205*etaL*etaL + 49.817*etaL - 0.3814;
                else if (Zmat > 25. && Zmat <= 37.5)  BL = -12.954*etaL*etaL*etaL -
8.1364*etaL*etaL + 39.949*etaL - 0.3758;
                else if (Zmat > 37.5 && Zmat <= 72.5) BL = -16.681*etaL*etaL*etaL
- 1.5168*etaL*etaL + 33.112*etaL - 0.3647;
                else                        BL = -25.443*etaL*etaL*etaL +
10.027*etaL*etaL + 27.209*etaL - 0.525;
                if (BL < 0) BL=0;
                CL = RL*log(etaL) + SL - BL;
            }
        //M-shell
            if (etaM > 0.3) {
                KA = 1.6;
                CM = KA*1e-4*(Zmat-14)*(Zmat-14)*(1.-b*b)/(b*b);
            }
            else {
                CM = 0;
            }

        //Calculate Mass Stopping Power in MeV*cm^2/g
            delta = 0.; //density effect is neglected in this version
            mstoppow_i[jint] =
4.*pi*r0*r0*me*N0*Zmat/Amat*Z*Z/(b*b)*(log(2.*me*1000000.*b*b/(Ipot*(1.-b*b)))-b*b-
(CK+CL+CM)/Zmat-delta);
            jint++;
        }
        jint = 0;
        mstoppow = 0.;
        while (jint < num) {
            mstoppow = mstoppow + mstoppow_i[jint] * f_i[jint];
            jint++;
        }
        if (i == 0) {
            outfile << "\n" << matname << "\t" << mat << "\t" << thick << "\t" << Ein <<
"\t" << b << "\t" << mstoppow << "\t" << mstoppow*rho/10.;
        }
        if (mstoppow <= 0.) {
            cout << "\nNote: At " << thick/bins*i << " cm into the target the energy of the
charged particle fell out of the range of this program." << endl;
            mstoppow = 0.;
            Etrns = Ein*A;
            E = 0.;
            b = 0.;
            break;
        }
        dE = dx * mstoppow * rho;
        Etrns = dE + Etrns;
        E = (E*A - dE)/A; // assumed that energy deposited is equal to Kinetic Energy loss
//      Ein = E; //Set beginning energy for next itteration/target to end of last itteration
        if (Etrns >= Ein*A) {
```

```
					Etrns = Ein*A;
					E=0.;
					b=0.;
					break;
				}
				i++;
			}

//output results
		outfile << "\t" << Etrns;
		Ein = E;
		if (E != 0.) outfile << "\t" << E << "\t" << b << "\t" << mstoppow*rho/10.;
		else {
				outfile << "\n\t\t**The particle stopped " << thick/bins*i << " into the material**";
				if (mstoppow == 0.) outfile << "\n\n*Note: At " << thick/bins*i << " cm into the " <<
matname << " target the energy of the charged particle fell out of the range of this program." << endl;
				break;
		}
}
		outfile << endl;
		infile.close();
		outfile.close();
		cout << "\nOutput file outfile.txt has been created in the bb_multi.exe folder.\n" << endl;
		return 0;
}
```